National Library of Canada

Acquisitions and Bibliographic Services Branch

395 Wellington Street
Ottawa, Ontario
K1A 0N4

Bibliothèque nationale du Canada

Direction des acquisitions et des services bibliographiques

395, rue Wellington
Ottawa (Ontario)
K1A 0N4

Your file Votre référence

Our file Notre référence

NOTICE

The quality of this microform is heavily dependent upon the quality of the original thesis submitted for microfilming. Every effort has been made to ensure the highest quality of reproduction possible.

If pages are missing, contact the university which granted the degree.

Some pages may have indistinct print especially if the original pages were typed with a poor typewriter ribbon or if the university sent us an inferior photocopy.

AVIS

La qualité de cette microforme dépend grandement de la qualité de la thèse soumise au microfilmage. Nous avons tout fait pour assurer une qualité supérieure de reproduction.

S'il manque des pages, veuillez communiquer avec l'université qui a conféré le grade.

La qualité d'impression de certaines pages peut laisser à désirer, surtout si les pages originales ont été dactylographiées à l'aide d'un ruban usé ou si l'université nous a fait parvenir une photocopie de qualité inférieure.

Canada

UNIVERSITY OF ALBERTA

BEHAVIOUR OF MASONRY CAVITY WALLS UNDER VERTICAL ECCENTRIC LOADS

BY

RU WANG 

A thesis submitted to the Faculty of Graduate Studies and Research in partial fulfilment of the requirements for the degree of Doctor of Philosophy

DEPARTMENT OF CIVIL ENGINEERING

EDMONTON, ALBERTA

Spring, 1996

ISBN 0-612-10651-9

University of Alberta

Library Release Form

Name of Author: Ru Wang

Title of Thesis: Behavior of Masonry Cavity Walls under Vertical Eccentric Loads

Degree: Doctor of Philosophy

Year This Degree Granted: 1996

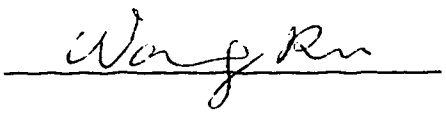

#301, 11147-82 Avenue

Edmonton, Alberta T6G 0T5

January 29, 1996

University of Alberta

Faculty of Graduate Studies and Research

The undersigned certify that they have read, and recommend to the Faculty of Graduate Studies and Research for acceptance, a thesis entitled Behavior of Masonry Cavity Walls under Vertical Eccentric Loads submitted by Ru Wang in partial fulfillment of the requirements for the degree of Doctor of Philosophy in Civil Engineering.

Dr. A.E. Elwi (Supervisor)

Dr. M. Hatzinikolas (Co-supervisor)

Dr. J. Warwaruk (Co-supervisor)

Prof. A.E. Peterson

Dr. D. Rogowsky

Dr. A.W. Lipsett

Dr. Nigel Shrive (External Examiner)

Date: Jan 29, 1996

ABSTRACT

The shear connector is a new type of masonry tie used to connect the two wythes of a masonry cavity wall. With the use of shear connectors, the stiffness and the load carrying capacities of cavity walls increase. However, there is no guidance for the design of such walls especially when the slenderness ratio of the wall is high.

As part of an ongoing investigation into the behaviour of this type of element, nine full scale shear connected masonry cavity walls have been tested under vertical eccentric loads. The tests provide a large amount of information regarding the behaviour of shear connected cavity walls. In addition, 46 shear connector units have been experimentally investigated under various loading conditions to provide information on the strength and stiffness properties of the units.

A nonlinear finite element analysis model is used to simulate the experimental investigation. A comparison of the simulation to the test results shows that the numerical simulation is quite satisfactory. The capacities and the load-deflection curves agree well with the test results.

Using the finite element model, a parametric study is carried out. Ninety-one cavity walls are analyzed. The parameters under investigation include the loading eccentricity, the slenderness ratio, the ratio of the end moments, the material properties of the block wythe, the cavity width, etc. A data base is then established including the results of the experiments and the numerical analyses.

A multi-linear regression analysis is carried out based on the data of the experiments and numerical analyses. The effective stiffness of the shear connected cavity walls is evaluated. Design equations for the ultimate strength of cavity walls are proposed

using the effective stiffness derived above in the context of the moment magnifier approach. A comparison of the proposed approach to the tests and the current masonry code shows that the proposed approach has adequate accuracy and better agreement with the test results than current code recommendations.

ACKNOWLEDGEMENTS

This investigation was made possible by financial assistance from the Canadian Masonry Research Institute, the Department of Civil Engineering, the University of Alberta Ph.D. Scholarship, IRAP (the Industry Research Assistance Program), and the Harry Edward Sim Memorial Scholarship fund.

The author is deeply grateful to her supervisors, Dr. A.E.Elwi, Dr. M. Hatzinikolas and Dr. J. Warwaruk for their help and guidance throughout the course of this study. The assistance provided by laboratory technicians R.Helfrich and L.Burden during the experimental phase of this study is also gratefully acknowledged.

TABLE OF CONTENTS

LIST OF TABLES

LIST OF FIGURES

LIST OF PLATES

LIST OF SYMBOLS

α	non-dimensional factor for stiffness of cavity walls
Δ	deflection of the wall under moment and axial load
δ	moment magnifier factor
β	ratio of the moments at the two ends of a wall
β_d	ratio of factored dead load moment to total factored moment
ϕ_e	resistance factor for masonry member
$(EI)_{block}$	stiffness of effective area section of block wythe
$(EI)_{brick}$	stiffness of effective area section of brick wythe
$(EI)_{eff}$	effective stiffness of a cavity wall for ultimate limit state
$(EI)_{spec}$	effective stiffness of a cavity wall under specified load
Δ_o	first order deflection of a wall under initial moment
a	area of cross-section of shear connector
a_r	reduced area of the cross section
b_1	thickness of brick wythe
b_2	thickness of block wythe
C	cavity width
C_e	eccentricity coefficient
C_m	moment diagram factor
C_s	slenderness coefficient
e	loading eccentricity
e_1	the smaller eccentricity occurring at the top or bottom of a wall
e_2	the larger eccentricity occurring at the top or bottom of a wall
EI	stiffness of a wall
E_i	initial tangent modulus of elasticity for masonry
e_k	kern eccentricity
E_m	modulus of elasticity of masonry, MPa
$[f]$	flexibility matrix of a shear connector

height of a member

moment of inertia of a member

cracked or uncracked moment of inertia of the section (depending on e_1) at end 1

cracked or uncracked moment of inertia of the section (depending on e_2) at end 2

cracked moment of inertia of the transformed section subjected to a pure moment, M_o

effective moment of inertia

moment of inertia of uncracked section

moment of inertia of uncracked section of the block wythe of a cavity wall

effective height factor for wall

unsupported height of wall

moment

the smaller factored end moment

the larger factored end moment

maximum moment occurring within the unsupported height of a wall

first order initial moment

ultimate moment carrying capacity

total moments including primary moment and secondary moment

Euler buckling load

factored vertical load

ultimate load carrying capacity

radius of gyration of a section

stiffness matrix of a shear connector

section modulus

thickness of a single wythe wall or thickness of the block wythe of a cavity wall

v	flexural deflection
v_{max}	maximum flexural deflection
v_o	first order deflection

CHAPTER ONE

INTRODUCTION

1.1 Introduction

As a structural element, a masonry wall should be designed to resist the lateral loads and/or the superimposed vertical loads. As an exterior element of the building, the wall serves as an aesthetic finish as well as a weather barrier to protect against moisture penetration and maintain good insulation. To accomplish these two functions, a masonry wall is designed, quite often, as a cavity wall with two wythes connected together. The exterior wythe of the cavity wall is usually constructed with burnt clay units and the interior wythe is usually constructed with concrete masonry units. Between the two wythes is the cavity which usually ranges from 25 mm to 100 mm. Modern improvements in the type of component, the design and the construction have led masonry walls to become thinner and more slender than ever before.

Traditional cavity walls are normally designed with the interior wythe as the load bearing wythe. The exterior wythe is designed with no requirement to resist the axial load other than bearing its own weight. Under lateral loads such as wind pressure or seismic loads, the exterior wythe is designed to be able to transfer the lateral loads to the structural back-up through the connectors without severe cracking or stability failure. The requirement is met by specifying a maximum spacing of the connectors which is 600 mm vertically and 800 mm horizontally.

In recent years, new types of masonry ties have been introduced. One such tie that is gaining acceptance is known as a "shear connector". The so called shear

connectors possess shear stiffness in the vertical plane and can transfer shear forces between the two wythes of a cavity wall. Research has revealed that the capacities and the stiffness of such shear connected cavity walls are increased considerably from the single wythe walls. This beneficial effect provided by the exterior wythe is important to the structural performance of slender masonry walls. In the design of such walls, consideration should be given to the contribution of the exterior wythe as a result of the composite actions between the two wythes of the wall.

Prior to the introduction of the CSA Standard CAN3-S304.1-94, masonry designers used the allowable stress design philosophy. The design of a masonry wall was dominated by the semi-empirical reduction factor method. Although a more rational moment magnifier approach was accepted by CAN3-S304-M84, the design equations were based on very simple assumptions which could not properly reflect the real behaviour of masonry walls. The current masonry structural code CAN3-S304.1-94 uses the moment magnifier method to design slender masonry walls. However, there is no direct guidance provided in the current code regarding the contribution of the exterior wythe to the capacity of shear connected cavity walls.

This investigation provides more information on the behaviour of slender masonry cavity walls and proposes a design approach to these walls under vertical eccentric compressive loads.

1.2 Literature Review

1.2.1 Shear Connector

The concept of a shear connector was introduced by Mullins and O'Connor at the University of Queensland, Australia (Mullins and O'Connor, 1987). The idea was to

transfer shear forces between the two wythes. The proposed shear connector consisted of a sheet of metal and extended tabs as shown in Figure1.1. The metal sheet is placed perpendicular to the two wythes of the wall and is continuous along the height of the cavity wall. The tabs are embedded into the head joints of each wythe at a specified spacing. Mullins and O'Connor concluded that this type of connector could improve the strength and stiffness of laterally loaded cavity wall.

One of the disadvantages of Mullins and O'Connor's connector is that both the width and the height of the units used to construct the two wythes must be identical. In other words, the connector is unable to incorporate the differences in the height of the course and the width of the units. Another problem is that the coupling effect induced by the connector may cause severe internal stresses in the wall due to the differential movement of the two wythes.

To overcome these problems, a new connector was proposed and investigated at the Canadian Masonry Research Institute and the University of Alberta. Pacholok (1988) tested the preliminary form of the shear connector which was later improved by Papanikolas et al.(1990). This type of connector is able to deal with the differences in the course height of the two wythes and is able to cope with the differential movement of the wall. Details of this shear connector will be discussed in the next chapter.

1.2.2 Shear Connected Masonry Cavity Wall

Since the introduction of the shear connector, experimental programs have been conducted by several researchers to investigate the performance of shear connected cavity walls subjected to lateral or vertical loading. Five full scale shear connected cavity walls under lateral loading were tested by Pacholok (1988). Compared to the traditional cavity wall constructed with flexible ties, it was found that the shear connected wall systems

resulted in increased lateral load carrying capacity and decreased lateral deflection. Twelve similar tests conducted by Papanikolas et al.(1990), with improved shear connectors confirmed these results.

Goyal et al. (1993) tested seven shear connected slender masonry cavity walls under vertical load. Of seven specimens, four were plain masonry walls and the other three were reinforced masonry walls. The test results showed that when a shear connected cavity wall is subjected to vertical eccentric loads, with the eccentricity towards the exterior wythe, the stiffness, and the capacity of the wall is increased and the deflection is decreased compared to those of a single wythe wall. It was also found that the contribution of the exterior wythe to the strength of the cavity wall increases as the loading eccentricity increases.

Neis and Sakr (1993) tested twenty-four cavity walls with various types of connectors. Among them, six walls were constructed with the shear connector mentioned above. The walls were subjected to vertical eccentric loads with small loading eccentricity. The increase of the capacity and stiffness of the cavity was not obvious and less than 10%.

1.2.3 Traditional Design Methods of Slender Masonry Walls

The traditional design method of slender masonry walls under vertical compressive loads is the reduction factor method. The capacity is reduced as a result of the slenderness effect and the loading eccentricity. The capacity of a slender wall is calculated as the capacity of a short axially loaded wall multiplied by the reduction factors C_s and C_e.

Yokel and Dikkers (1971) suggested that the moment magnifier method which had been successfully used for steel and concrete structures be accepted for the design of

slender masonry walls. They suggested that the magnified moment should be calculated by:

$$M = M_o \left(\frac{C_m}{1 - \frac{P}{P_{cr}}} \right) \tag{1.1}$$

In which,

M_o = Maximum moment imposed by external force

$C_m = 0.6 + 0.4\ (M_1/M_2) \geq 0.4$

M_1 = the smaller end moment,

M_2 = the larger end moment,

$$P_{cr} = \frac{\pi^2 EI}{(kh)^2}$$

where,

k = effective length factor

h = wall height,

$EI = \frac{E_i I_n}{3.5}$, for plain masonry wall

$EI = \frac{E_i I_n}{2.5}$ for reinforced masonry wall

E_i = initial tangent modulus of elasticity for masonry

I_n = moment of inertia of the uncracked section

Expressions for the effective stiffness EI were proposed by several other researchers. Hatzinikolas et al. (1978) suggested that: for plain masonry or reinforced masonry walls with loading eccentricity less than t/3, the moment of inertia is:

$$I = 8\left(0.5 - \frac{e}{t}\right)^3 I_o \qquad (1.2)$$

and for reinforced walls with loading eccentricity greater than t/3:

$$I = (0.5 - e/t) I_o > 0.1 I_o \qquad (1.3)$$

where, I_o = the moment of inertia of uncracked section.

Ojinaga and Turkstra (1980) suggested that: $P_{cr} = \dfrac{\pi^2 E_m I_{eff}}{(kh)^2}$ (1.4)

For unreinforced masonry:

$$I_{eff} = (I_1 + I_2)/4 \qquad \text{for } 0 \le e_1/e_2 \le 1 \qquad (1.5a)$$

I_{eff} = the lesser of $(I_1 + I_o)/4$ and $(I_2 + I_o)/4$ for $-1 \le e_1/e_2 \le 0$ (1.5b)

For reinforced masonry:

$$I_{eff} = (I_1 + I_{cr} + I_2)/4 \qquad \text{for } 0 \le e_1/e_2 \le 1 \qquad (1.5c)$$

I_{eff} = the lesser of $(I_1 + 2I_{cr} + I_o)/4$ and $(I_2 + 2I_{cr} + I_o)/4$ for $-1 \le e_1/e_2 \le 0$ (1.5d)

where, I_1, I_2 = the cracked or uncracked moments of inertia of the sections at ends 1 and 2.

I_o = uncracked moment of inertia of the section.

I_{cr} = the cracked moment of inertia of the transformed section subjected to a pure moment M_o

This expression for EI was adapted by the CAN3-S304-M84 Code.

Ojinaga and Turkstra (1980) also proposed the load displacement method for the design of slender masonry wall. In this method the wall is designed to carry a secondary moment in addition to the primary moment. The secondary moment was calculated as the product of the axial load P, and the displacement of the section centroid from the

centroidal plane through the wall ends. The displacement is obtained using the same EI as calculated with the moment magnifier method. The method was initially proposed as an iterative procedure but was accepted as a one step approach.

The current structural masonry design code CAN3-S304.1-94 allows both the load displacement method and the moment magnifier method to be used to consider the secondary moment effect. The effective stiffness of the wall is expressed as a function of the moment of inertia of the uncracked and the cracked sections, the loading eccentricity e and the kern eccentricity e_k. The term kern eccentricity e_k stands for the limiting eccentricity that prevents tension being developed in the section. Details of the moment magnifier method specified by the current code will be discussed in Chapter Six.

This brief literature review indicates that little research has been conducted on the behaviour of shear connected slender cavity walls. It is noticeable that the evaluation of the cross-sectional properties at different loading stages is/was based on the properties of single wythe walls. There is no direct guidance regarding the estimation of the cross-sectional properties of the composite system nor the evaluation of the effective stiffness of cavity walls.

1.3 Objectives and the Scope of the Thesis

The main purpose of this investigation is to improve understanding of the behaviour of shear connected slender masonry cavity walls subjected to vertically applied eccentric loads. Through the experimental and analytical investigation, a design guide for such walls is presented. The investigation can be subdivided into the following objectives:

(1) To experimentally investigate the behaviour of the shear connectors under various loading conditions, and to evaluate the cross sectional properties of the shear connectors based on the test results.

(2) To experimentally study the behaviour of cavity walls subjected to vertical eccentric loading, and to specifically examine the effect of loading eccentricities on the capacity and the stiffness of the cavity wall.

(3) To develop a finite element analysis model for numerical simulation of the full scale wall tests. This model would be used to compare the analytical results with the experimental results to verify the validity of the analysis model.

(4) To study experimentally, and/or analytically, the effects of parameters such as the geometric and material properties of the cavity wall as well as the loading conditions.

(5) To evaluate the effective stiffness of the cavity wall for calculating the moment magnifier factor.

(6) To estimate the stiffness of the cavity wall for the purpose of deflection calculation.

(7) To develop a rational approach for the design of slender masonry cavity walls which properly accounts for the contribution of the exterior wythe to the capacity of the cavity wall.

1.4 Organization of the Thesis

In Chapter Two of this thesis, the experimental program carried out on the shear connectors is described. Chapter Three presents the experimental program on shear connected slender masonry cavity walls. The effect of the loading eccentricities on the capacity of the cavity walls is studied. A finite element model is developed in Chapter Four for numerical simulation of the experimental program. The tests validate the analytical results. In Chapter Five, the numerical model is used to analyze more walls with varying

parameters to study the effects of these variables on the capacity and the stiffness of the cavity walls. Chapter Six presents the derivation of the design equations for cavity walls. Finally, a brief summary of the conclusions and recommendations are addressed in Chapter Seven.

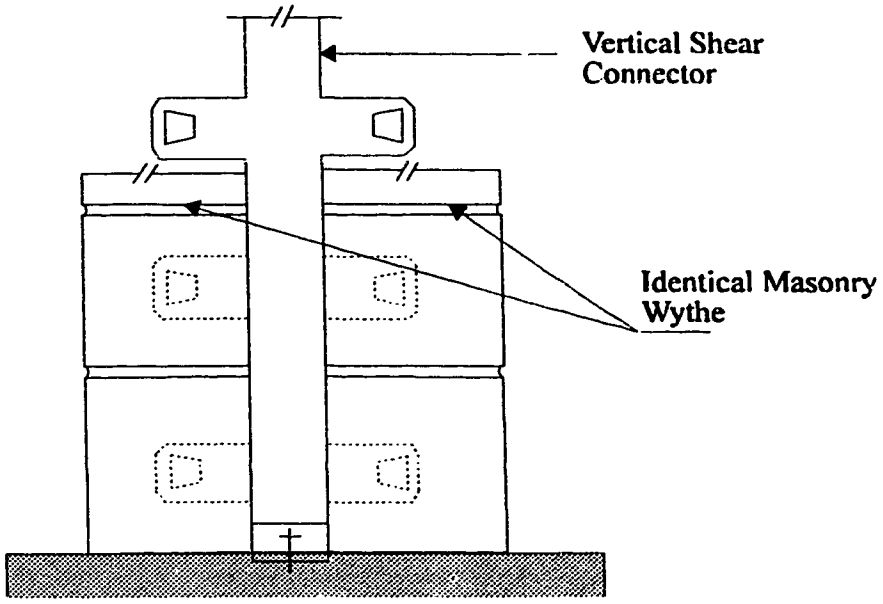

Figure 1.1 Mullins and O'Connor's Connector

CHAPTER TWO

SHEAR CONNECTORS

2.1 Introduction

The composite action between the two wythes of a cavity wall relies on the efficiency of the shear connector as a moment transfer mechanism. An experimental program on the behaviour of the shear connectors was carried out as part of this investigation. This program investigated the strength and the stiffness of the shear connectors under various loading conditions. The test program and the results are described and discussed in this chapter.

2.2 The Shear Connector

The connector mentioned in this thesis is a device which connects the two wythes of the masonry cavity walls. In recent years, many new types of connectors have been invented. At present, a variety of connectors are commercially available for masonry cavity walls. The shape and placement of the connectors depend on the specific functions that must be fulfilled. Nevertheless, there exist differences in the quality of the performance that the connectors should accomplish.

2.2.1 Development of the Shear Connectors

The connector should function as a wall tie to transfer the forces between the two wythes. The brick wythe of the cavity wall is usually subjected to horizontal wind load.

The connectors should be able to tie the exterior wythe to the back-up wythe so that under lateral pressure or suction, the exterior wythe does not develop large cracking failure. Although it is not required that the exterior wythe resist the vertical load which is normally imposed on the back-up wythe, a proper connection between the two wythes could enhance the capacity of the cavity wall under vertical loading. In the direction perpendicular to the wall panel, the connector should be able to restrain any extensive relative movement which causes the two wythes to move closer or apart. This is because large movements or rotation could result in significant cracking within the brick joints, weakening the ability of the exterior wythe to act as a barrier to the outside climates. To accomplish this function, the connectors should be firmly embedded within the joints without pull-out or punch through failure. It also has to have adequate strength and stiffness to provide restraint to the exterior wythe.

Traditional connectors provided for transferring the loads from the exterior wythe to the inner wythe. The shear connectors initially tested by Pacholok (1988) and improved by Papanikolas and the Canadian Masonry Research Institute (1990) caused the two wythes to act together in resisting loads applied perpendicular to the outer wythe. Unlike traditional connectors, this type of shear connector provides partial restraint to the movements of the two wythes of the wall. The connector consists of a steel plate, a V-tie, and a device which holds the insulation material in place as shown in Figure 2.1. The steel plate and the V-tie form the force transfer mechanism. To transfer the force, the thin and short plate of the connector has a relatively large shear stiffness. To ensure proper restraint to the wythes, the V-tie made of steel rod is embedded, at one end into the brick mortar joints. The plate is firmly embedded in the block mortar joints. To provide flexibility in the direction parallel to the wall panel, the V-tie and the thin plate are connected through one of eight small holes at the tip of the thin plate to allow relative rotation between them therefore, the two wythes connected by such mechanism can have relative vertical movement without inducing large stresses. Figure 2.2 shows a shear connector embedded in a cavity wall.

2.2.2 The Profile of Shear Connectors

Figures 2.3(a) and 2.3 (b) show the dimensions of the connector plates for a 75 mm and a 100 mm cavities. The nominal thickness of the connector plate is 1.5 to 1.6 mm. Eight holes with a diameter of 6 mm are located at the front edge of the plate. The V-tie is installed in one of the eight holes. This mechanism allows the connection between the plate and the V-tie to be adjustable along the height to incorporate the difference in courses between the block and the brick wythes. In the middle part of the plate, there are five holes in the 75 mm connector and eight holes in the 100 mm connector. These holes are made to reduce the thermal conductivity of the connector. The rear part of the connector plate which is embedded into the mortar layer of the block wythe contains a cantilever lip embedded horizontally to enhance the embedment of the connector as shown in Figure 2.1.

2.2.3 Physical Properties of the Shear Connectors

As shown in Figure 2.2, one end of the connector plate is embedded into the mortar-block joint. With adequate embedment, this part of connector plate will work together with the block wythe. Therefore, the strength and the stiffness of this part are not important. The middle part of the connector plate is left in the cavity. Under different loading conditions, this part of the connector plate can be subject to tension, compression, and shear forces.

To investigate the behaviour of the shear connector in the cavity wall, the cross-sectional properties of the part of connector plate which is exposed in the cavity need to be evaluated. As can be seen in Figure 2.3, the evaluation of the cross-sectional properties is not easy to accomplish due to the irregular shape of the plate. Even though the

theoretical cross-sectional properties may be derived from the dimensions of the connector, using these properties to predict the behaviour of the connector may not reflect stress concentrations, inelastic effects and residual stresses from fabrication. The variations in the loading conditions include the location of the V-tie along the height of the connector, the initial out-of-plane eccentricities due to the imperfections in the alignment between the connector plate and the V-tie as well as the different load types imposed on the block or brick wythes, etc. Therefore, an experimental investigation was carried out to evaluate the cross-sectional properties of the connector. The investigation was focused on establishing a nominal connector plate which has a rectangular shape and solid cross section. The cross-sectional properties of this shear connector are equivalent to the properties of the real connector.

2.3 Tests on Shear Connectors

To investigate the behaviour of the shear connector and to find out the equivalent cross-sectional properties as a nominal plate, a total of 46 shear connectors has been tested under tension, compression, shear and bending.

2.3.1 Tension Test

2.3.1.1 Test Set-up and Measurement

The tests were carried out on the testing frame shown in Figure 2.5. The specimens were fixed at one end to the testing frame as shown in Plate 2.1. The tensile force was applied at the free end through a steel rod which connected the specimens with a manually controlled hydraulic jack.

A linear variable differential transformer (LVDT) was placed at the loading point and was used to measure the elongation of the specimens. Because the LVDT was

mounted at the point between the base of the frame and the load cell, the elongation of the rod could affect the accuracy of the test results. To take this into account, a special test was conducted on the elongation of the rod to exclude the rod deformation from the recorded shear connector elongation. Three dial gauges were also mounted on the frame to monitor the in-plane and out-of-plane displacement as shown in Plate 2.1.

2.3.1.2 Test Results and Discussion

The yield strengths, the ultimate strengths and the flexibility parameters of the connectors under tensile loading are summarized in Table 2.1(a), in which the flexibility parameter is the reciprocal of the slope of the load-deflection curves at the elastic stage. A typical load-deflection curve of the tensile specimen is shown in Figure 2.7(a). It was found that all the tensile failures were caused by local yielding at the loading hole. At the final stage of loading, the loading hole was simply pulled apart. Comparing the results between the specimens with different loading locations, it was found that the loading at the third hole resulted in the highest load capacity and the maximum initial stiffness. However, the difference in capacity due to the loading locations is not significant. It can be seen from the table that for each loading point, the variations of the results of the ultimate load capacity and the stiffness obtained from three duplicated tests are small. These results indicate that the tensile capacity and the initial stiffness of the shear connector are affected by the cross-sectional properties around the loading holes.

2.3.2 Compression Test

A total of fourteen specimens was tested under compressive load. Among them, three were 75 mm connectors and all the others were 100 mm connectors. For the 100 mm specimens, the load was applied at the first, the third and the fourth holes respectively. For the 75 mm specimens, the load was applied at the third hole.

2.3.2.1 Test Set-up and Measurement

The compression test set-up is shown in Figure 2.6(a) and Plate 2.2. A pin which is essentially a straightened V-tie was used to connect the specimen with the loading plate which was connected to the hydraulic jack. The stiffness of the loading plate was much higher than that of the specimen, therefore the deformation of the loading plate should not affect the test results. This loading system was trying to simulate the real situation where a V-tie embedded in the mortar layer in the brick wythe and attached to the connector plate through the holes.

A LVDT was placed at the loading point to record the in-plane deformation of the specimen. Three dial gauges were placed to record the out-of-plane deformations.

2.3.2.2 Test Results and Discussion

Compression test results are summarized in Table 2.1(b). It was found that the failure mode of all the compression tests was out-of-plane buckling. Plate 2.3 shows a specimen that buckled under ultimate compressive load. A typical load-deflection curve of the compression test is shown in Figure 2.7(b). Test results revealed that the load vs. deformation response is approximately linear before reaching the ultimate load followed by a sudden drop after reaching the ultimate load. This shape of the load-deflection curve reflects the buckling failure mode of the specimens. It was also found from the test that loading at the third hole gave the highest load capacity with a mean value of 3.92 kN for 75 mm cavity connector and 3.45 kN for 100 mm cavity connector. This fact seems to imply that the centroid of the connector plate may pass through the third hole or close to it. It was also found that the slope of the load-deflection curve was influenced by the loading locations. Loading at the first hole resulted in a larger deformation of the specimens. During the whole loading process, dial gauges were used to record out-of-

plane displacements. The dial gauges indicated that at the initial loading stage of the compression tests, the loading device was kept in a good alignment with the specimens. The out-of-plane deformations were small for most specimens. It was not until the loads almost reached the ultimate load capacities, that the out-of-plane displacements developed rapidly.

2.3.3 Shear Test

A total of thirteen specimens was tested under shear loading. Three were 75 mm shear connectors, while the others were 100 mm connectors. For the 100 mm specimens, the loads were applied at the third, the fourth, and the eighth holes respectively. For the 75 mm specimens, the load was applied at the third hole.

2.3.3.1 Test Set-up and Measurement

The shear test set-up is shown in Figure 2.6 (b) and Plate 2.4. The shear force was applied in the plane parallel to the connector plate through a loading rod. A LVDT was placed at the loading point to measure the shear deformation of the specimens. The elongation of the rod was tested, recorded and eliminated from the records of the elongation of the specimens.

2.3.3.2 Test Results and Discussion

The shear test results are summarized in Table 2.1 (c). Loading at the third hole resulted in the largest load carrying capacities. However, the difference was not significant when loading at the different locations. The stiffness is almost the same when loading at

the third and the fourth holes. Figure 2.7 (c) shows the load-deflection curve of one of the specimens under shear load.

2.3.4 Bending Test

A total of six specimens was tested under bending. Three of them were 75 mm connectors and the other three were 100 mm connectors.

2.3.4.1 Test Set-up and Measurement

The bending device is shown in Figure 2.6(c) and Plate 2.5. A loading device made of two steel plates was connected to the specimen as shown in the figure. The connection between the loading plate and the specimen was through two steel pins one at the first hole and the other at the eighth hole of the specimen. At the other end of the loading plate, a steel rod was used to connect the loading plate to the hydraulic jack. When a tension force generated from the hydraulic jack is applied to the steel rod, the loading plate will impose a tensile force at the first hole and an equal compressive force at the eighth hole. The tensile and the compressive forces will form a bending couple. This bending device induced a moment and a shearing force on the specimen. LVDT's were placed at the tip of the shear connectors to measure the deformation of the specimens under the bending moment and the shear force.

The test results are summarized in Table 2.1(d). Failure of the specimens was due to large deformation in the tension zone accompanied with local buckling in the compression zone.

2.4 Capacities of the Shear Connectors

Table 2.2 summarizes the ultimate capacities of the connectors under each loading case. It should be mentioned that the test results should be interpreted rationally by considering the following aspects:

In the case of the connector subjected to tension and shear loads, as discussed earlier, the strength of the connector depends much on the properties of the plate that surrounds the loading hole. Since this area is relatively weak, the deformation of the connector is significant before reaching the ultimate load. For this reason, the yield strength was used in defining the properties of the connector.

In a cavity wall, where the block wythe is subjected to an eccentric vertical load, the connector may be loaded with a combination of shear, bending and/or axial forces. In such situations, the strength of the connector is weaker than that when subjected to a single load.

When more than one connector is placed in a course, the total strength is smaller than the sum of each individual connector. This is because the pattern of the placement of the connector and the inevitable imperfection in the construction of the wall could cause stress concentration in one or a few connectors.

2.5 Beam Model

To investigate the behaviour of the connector and to evaluate its cross-sectional properties, a short beam analysis model was established. The shear connector plate exposed in the cavity is treated as a beam. At the end where the connector plate is embedded into the block wythe, the end restraint is simplified as fixed. At the other end, the connector plate is subjected to the load transferred through the V-tie. This end was treated as free end. Thus, the connector plate is a cantilever beam subjected to the loads

applied at the free end. This beam is very short. The span-height ratio usually ranges from 1.0 to 1.6. In such short beam, the shear deformation is of great importance. Figure 2.4(a) shows a short beam and the coordinate of deformations. The flexibility matrix for such a beam is (Ghali and Neville, 1989):

$$[f] = \begin{bmatrix} \frac{h^3}{3EI} + \frac{h}{Ga_r} & \frac{h^2}{2EI} \\ \frac{h^2}{2EI} & \frac{h}{EI} \end{bmatrix} \qquad (2.1)$$

Where, $\frac{h}{Ga_r}$ is the shear deformation at the free end due to a unit transverse load applied at that end. G is the shear modulus of elasticity, a_r is the reduced area of the cross section. a_r depends on the shear stress distribution, which in turn depends on the shape of the cross section (Timoshenko and Gere, 1972).

Therefore, the stiffness matrix of this beam is:

$$[S] = \begin{bmatrix} \frac{12EI}{(1+\alpha)h^3} & -\frac{6EI}{(1+\alpha)h^2} \\ -\frac{6EI}{(1+\alpha)h^2} & \frac{(4+\alpha)EI}{(1+\alpha)h} \end{bmatrix} \qquad (2.2)$$

In which, $\alpha = \frac{12EI}{h^2 Ga_r}$

If the axial deformation is included, the flexibility matrix is:

$$[f]=\begin{bmatrix} f_{11} & f_{12} & f_{13} \\ f_{21} & f_{22} & f_{23} \\ f_{31} & f_{32} & f_{33} \end{bmatrix}=\begin{bmatrix} \frac{h}{Ea} & 0 & 0 \\ 0 & \frac{h^3}{3EI}+\frac{h}{Ga_r} & \frac{h^2}{2EI} \\ 0 & \frac{h^2}{2EI} & \frac{h}{EI} \end{bmatrix} \qquad (2.3)$$

In which, f_{ij} is the deformation at point i caused by the force applied at point j. Figure 2.4 (b) shows the coordinates which correspond to the flexibility matrix of equation (2.3) Therefore, the corresponding stiffness matrix is:

$$[S]=\begin{bmatrix} K_{11} & K_{12} & K_{13} \\ K_{21} & K_{22} & K_{23} \\ K_{31} & K_{32} & K_{33} \end{bmatrix}=\begin{bmatrix} \frac{Ea}{h} & 0 & 0 \\ 0 & \frac{12EI}{(1+\alpha)h^3} & -\frac{6EI}{(1+\alpha)h^2} \\ 0 & -\frac{6EI}{(1+\alpha)h^2} & \frac{(4+\alpha)EI}{(1+\alpha)h} \end{bmatrix} \qquad (2.4)$$

Where, K_{ij} is the force induced at point i due to the deformation at point j.

2.6 Cross-Sectional Properties of the Connectors

2.6.1 Stiffness of the Shear Connectors

The test results of various loading conditions were used to evaluate the terms in the flexibility matrix and stiffness matrix. For 100 mm cavity connectors, it was found from the combined shear and bending tests that:

$$f_{23} = f_{32} = 2.466 \times 10^{-3} \qquad rad/kN$$

where notations follow the coordinates shown in Figure 2.4(b). Because $f_{23} = f_{32} = \frac{h^2}{2EI}$, for h = 97 mm, which is the actual length of the specimen measured from the loading point to the end restraint, the EI value is found to be:

$$EI = \frac{97^2 (mm^2)}{2 \times 2.466 \times 10^{-3} (rad / kN)} = 1.91 \times 10^9 \qquad N \cdot mm^2$$

And if E is taken as 200 GPa, then $I = 9550\ mm^4$.

Also the shear and bending tests indicated that:

$$f_{22} = \frac{h^3}{3EI} + \frac{h}{Ga_r} = 0.3073 \qquad mm/kN$$

Rearranging the above expression, one obtains:

$$Ga_r = \frac{h}{-\frac{h^3}{3EI} + 0.3073} = 655 \qquad kN$$

The term was found to have a value of $\alpha = \frac{12EI}{h^2 Ga_r} = 3.72$

Lastly the term $f_{11} = \frac{h}{Ea} = 0.1876$ mm/kN corresponds to the loading case where the axial force is in tension. For axial force in compression, $f_{11} = \frac{h}{Ea} = 0.3127$ mm/kN.

The corresponding flexibility matrix and stiffness matrix are written as:

$$[f] = \begin{bmatrix} \frac{h}{Ea} & 0 & 0 \\ 0 & \frac{h^3}{3EI} + \frac{h}{Ga_r} & \frac{h^2}{2EI} \\ 0 & \frac{h^2}{2EI} & \frac{h}{EI} \end{bmatrix} = \begin{bmatrix} 0.1876 & 0 & 0 \\ 0 & 0.3073 & 2.466 \times 10^{-3} \\ 0 & 2.466 \times 10^{-3} & 50.79 \times 10^{-6} \end{bmatrix}$$

From which the stiffness matrix is obtained as:

$$[S] = \begin{bmatrix} \frac{Ea}{h} & 0 & 0 \\ 0 & \frac{12EI}{(1+\alpha)h^3} & -\frac{6EI}{(1+\alpha)h^2} \\ 0 & -\frac{6EI}{(1+\alpha)h^2} & \frac{(4+\alpha)EI}{(1+\alpha)h} \end{bmatrix} = \begin{bmatrix} 5.33 & 0 & 0 \\ 0 & 5.32 & -258.0 \\ 0 & -258.0 & 32.2 \times 10^3 \end{bmatrix}$$

Where, $K_{11} = 5.33$ kN/mm corresponds to the loading case in which the axial force is in tension. For compressive axial load, $K_{11} = 3.18$ kN/mm.

The flexibility matrix and stiffness matrix obtained above are for 100 mm connectors. For 75 mm connectors, a similar derivation is followed:

From the tests it was found that:

$$f_{23} = f_{32} = \frac{h^2}{2EI} = 1.06 \times 10^{-3} \qquad rad/kN$$

for $h = 77$ mm,

$$EI = \frac{h^2(mm^2)}{2 \times 1.06 \times 10^{-3}(rad/kN)} = 2.806 \times 10^9 \qquad N \cdot mm^2$$

And if E = 200 GPa, then I = 14030 mm^4.

Similarly,

$$f_{22} = \frac{h^3}{3EI} + \frac{h}{Ga_r} = 0.2668 \qquad mm/kN$$

where 0.2668 *mm/kN* was obtained from the test. Rearrange the above expression, to obtain Ga_r as:

$$Ga = \frac{h}{-\frac{h^3}{3EI} + 0.2668} = 362 \quad kN$$

Hence, $\alpha = \frac{12EI}{h^2 Ga_r} = 15.69$

Lastly, f_{11} = 0.1876 mm/kN and K_{11} = 5.33 kN/mm correspond to the loading case where the axial force is in tension. For the axial force in compression and for 75 mm cavity connectors, f_{11}= 0.3675 mm/kN, and K_{11} = 2.72 kN/mm.

Therefore, the flexibility matrix is:

$$[f]=\begin{bmatrix} f_{11} & f_{12} & f_{13} \\ f_{21} & f_{22} & f_{23} \\ f_{31} & f_{32} & f_{33} \end{bmatrix}=\begin{bmatrix} 0.1876 & 0 & 0 \\ 0 & 0.2668 & 1.06\times10^{-3} \\ 0 & 1.06\times10^{-3} & 27.44\times10^{-6} \end{bmatrix}$$

The corresponding stiffness matrix is:

$$[S]=\begin{bmatrix} K_{11} & K_{12} & K_{13} \\ K_{21} & K_{22} & K_{23} \\ K_{31} & K_{32} & K_{33} \end{bmatrix}=\begin{bmatrix} 5.33 & 0 & 0 \\ 0 & 4.419 & -170.1 \\ 0 & -170.1 & 43.0\times10^{3} \end{bmatrix}$$

The EI values obtained from the above derivation were used in the numerical analyses of the cavity walls which will be described in Chapter Four and Chapter Five. For the 75 mm connector, E = 200 GPa and, I = 14030 mm^4. For the 100 mm connector, E = 200 GPa and, I = 9550 mm^4.

2.6.2 Effective Cross-Sectional Area

The axial load capacities obtained in the test were thought to be higher than expected in actual practice. This is because the end restraints are stiffer than the actual embedment of the connector in the brick wythe. Therefore only 1/3 of the average capacity was considered effective. For the 75 mm connector, the axial load capacity was taken as 0.9 kN. Assuming a yield strength of 300 MPa, the corresponding cross-sectional area is 2.95 mm^2. For 100 mm cavity connector, the area is 1.82 mm^2. This corresponds to the axial load capacity of 0.6 kN.

2.7 Summary

In this chapter, the shear connector used in this investigation is discussed. The test results on such connectors are presented. Based on the test results, the cross-sectional

properties of the connectors are evaluated. Those values were used in the numerical analyses of the cavity walls. Based on the test results, the stiffness matrices of the short beam model of the connectors were evaluated.

Table 2.1 (a) Shear Connector Tension Test

Specimen	Load Type	Loading hole	Cavity mm	Ultimate Load kN	Yield Load kN	Flexibility Parameter mm/kN
S1	T	4	100	3.51	2.81	0.1946
S2	T	4	100	3.72	2.98	0.2398
S3	T	4	100	3.75	2.85	0.1812
S5	T	1	100	3.66	2.72	0.2278
S6	T	1	100	3.69	2.66	0.1736
S7	T	1	100	3.72	2.68	0.1812
S8	T	3	100	3.81	2.68	0.2066
S9	T	3	100	3.78	2.83	0.1706
S10	T	3	100	3.81	3.02	0.1721
S22	T	3	100	3.66	2.71	0.1695
S24	T	3	100	3.51	2.85	0.1869
S25	T	3	100	3.60	3.00	0.1688
S26	T	3	100	3.72	2.98	0.1264

Note:

T = tension force

Loading hole = number of the loading holes labeled from the top to the bottom of the connector plate

Flexibility Parameter = inverse of initial slope of the load-deformation curve of the specimen

Table 2.1 (b) Shear Connector Compression Test

Specimen	Load Type	Loading Location	Cavity mm	Ultimate Load kN	Flexibility Parameter mm/kN
S11	C	3	100	3.63	0.2924
S12	C	3	100	4.20	0.3413
S13	C	3	100	3.72	0.2985
S23	C	3	100	3.66	0.2924
S14	C	4	100	3.78	0.3021
S15	C	4	100	3.39	0.2936
S17	C	4	100	3.57	0.2755
S18	C	1	100	2.91	0.2725
S19	C	1	100	3.12	0.3891
S20	C	1	100	3.18	0.3559
S21	C	1	100	2.85	0.3268
S49	C	3	75	3.66	0.3333
S50	C	3	75	3.36	0.3891
S52	C	3	75	4.74	0.3802

Table 2.1 (c) Shear Connector Shear Test

Specimen	Load Type	Loading hole	Cavity mm	Ultimate Load kN	Flexibility Parameter mm/kN
S27	S	8	100	2.64	Rejected
S28	S	8	100	2.70	Rejected
S29	S	8	100	2.61	0.2899
S30	S	8	100	2.73	0.3559
S31	S	3	100	2.76	0.2899
S32	S	3	100	2.91	0.3344
S33	S	3	100	2.73	0.2985
S34	S	4	100	2.76	0.3268
S35	S	4	100	2.85	0.3236
S36	S	4	100	2.73	0.2625
S37	S	3	75	3.21	0.2786
S38	S	3	75	3.21	0.2688
S39	S	3	75	3.27	0.2532

Table 2.1 (d) Shear Connector Bending Test

Specimen	Load Type	Loading hole	Cavity mm	Ultimate Load kN	Maximum Moment kN·m	Flexibility Parameter mm/kN
S41	B	N/A	100	1.47	0.140	0.5650
S42	B	N/A	100	1.47	0.140	0.5618
S43	B	N/A	100	1.44	0.137	0.5025
S44	B	N/A	75	1.83	0.174	0.3106
S46	B	N/A	75	1.53	0.145	0.2558
S47	B	N/A	75	1.53	0.145	0.2941

Table 2.2

Type of Loading	Number of Specimens	Cavity (mm)	Ultimate Load (kN)		
			Mean	Standard Error	Standard Diviation
T	13	100	3.72	0.0275	0.099
C	11	100	3.45	0.1233	0.409
S	10	100	2.74	0.0280	0.089
B	3	100	1.46	0.0100	0.017
S	3	75	3.23	0.0200	0.035
C	3	75	3.92	0.4190	0.725
B	3	75	1.63	0.1000	0.173

Note:

T = Tensile Load
C = Compressive Load
S = Shear Load
B = Bending

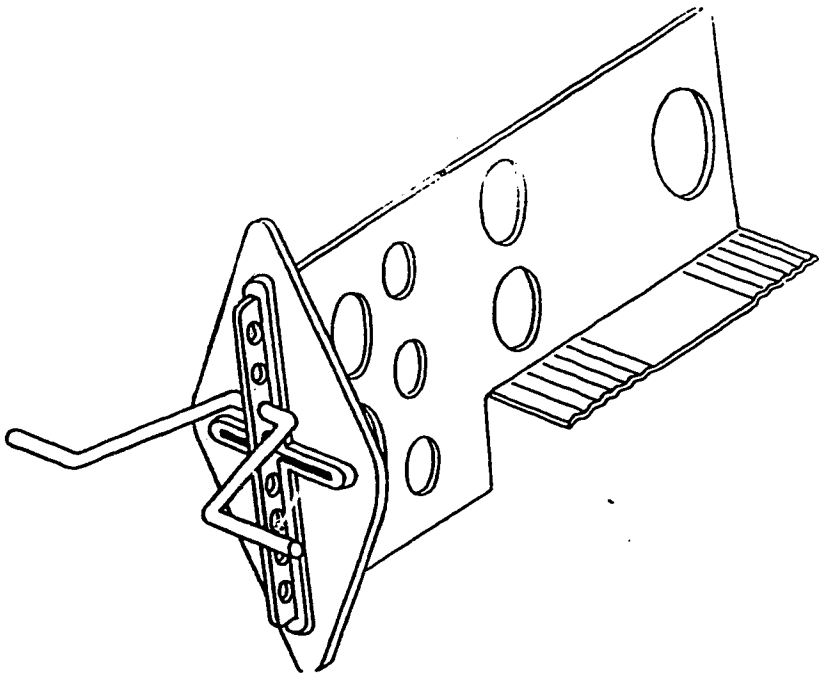

Figure 2.1 Shear connector (Courtesy K.Papanikolas)

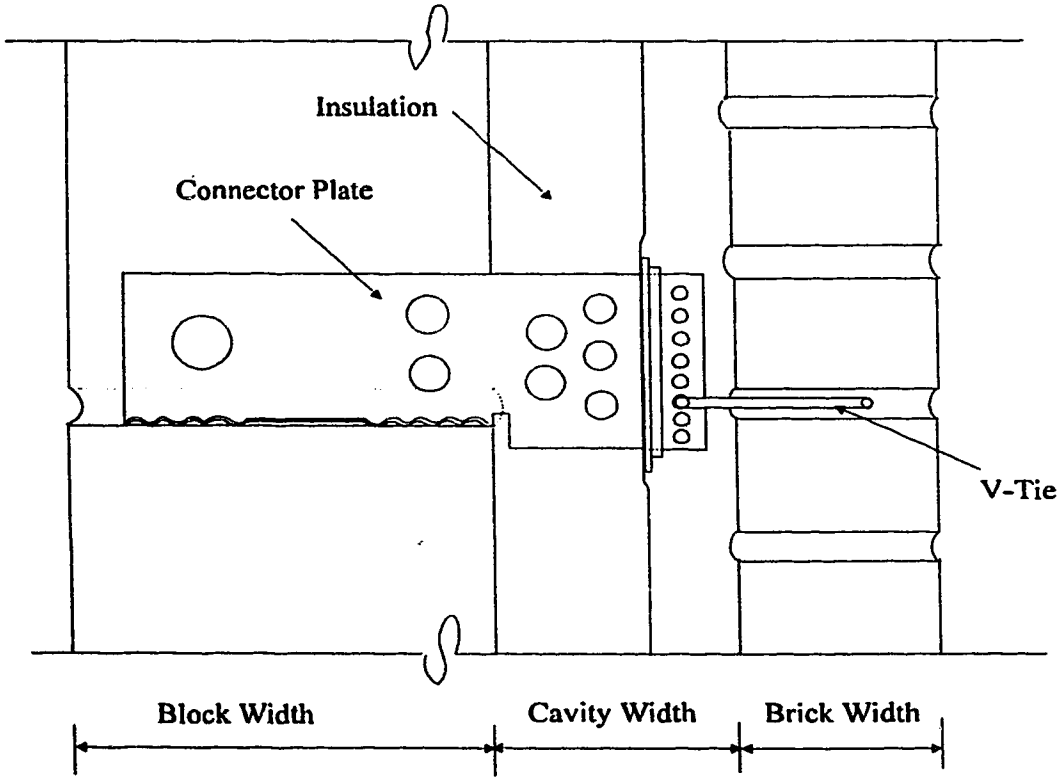

Figure 2.2 Shear connector in the cavity wall

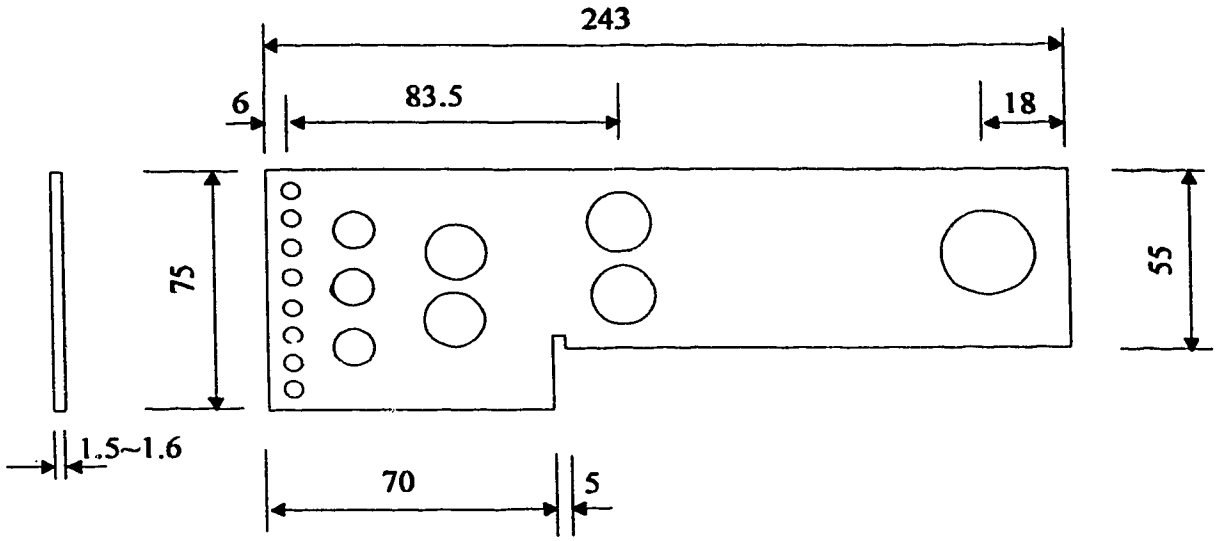

Figure 2.3 (a) Shear connector for 75 mm cavity

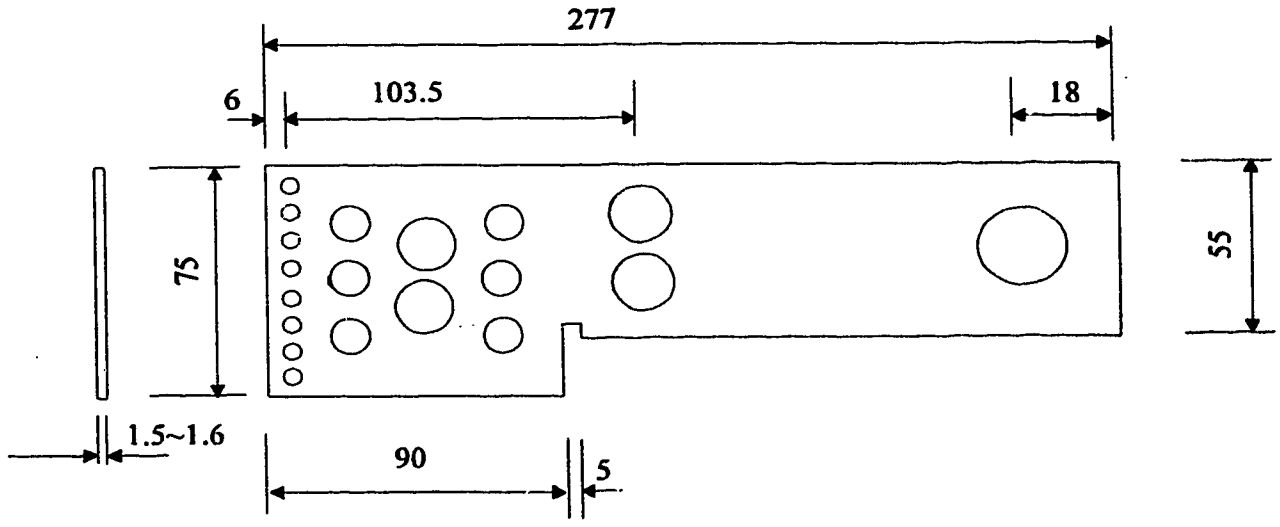

Figure 2.3 (b) Shear connector for 100 mm cavity

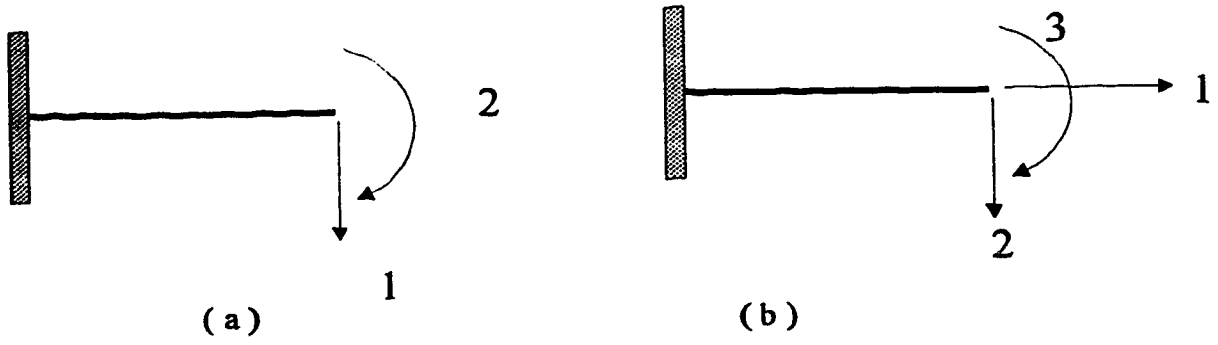

Figure 2.4 Coordinate of beam model

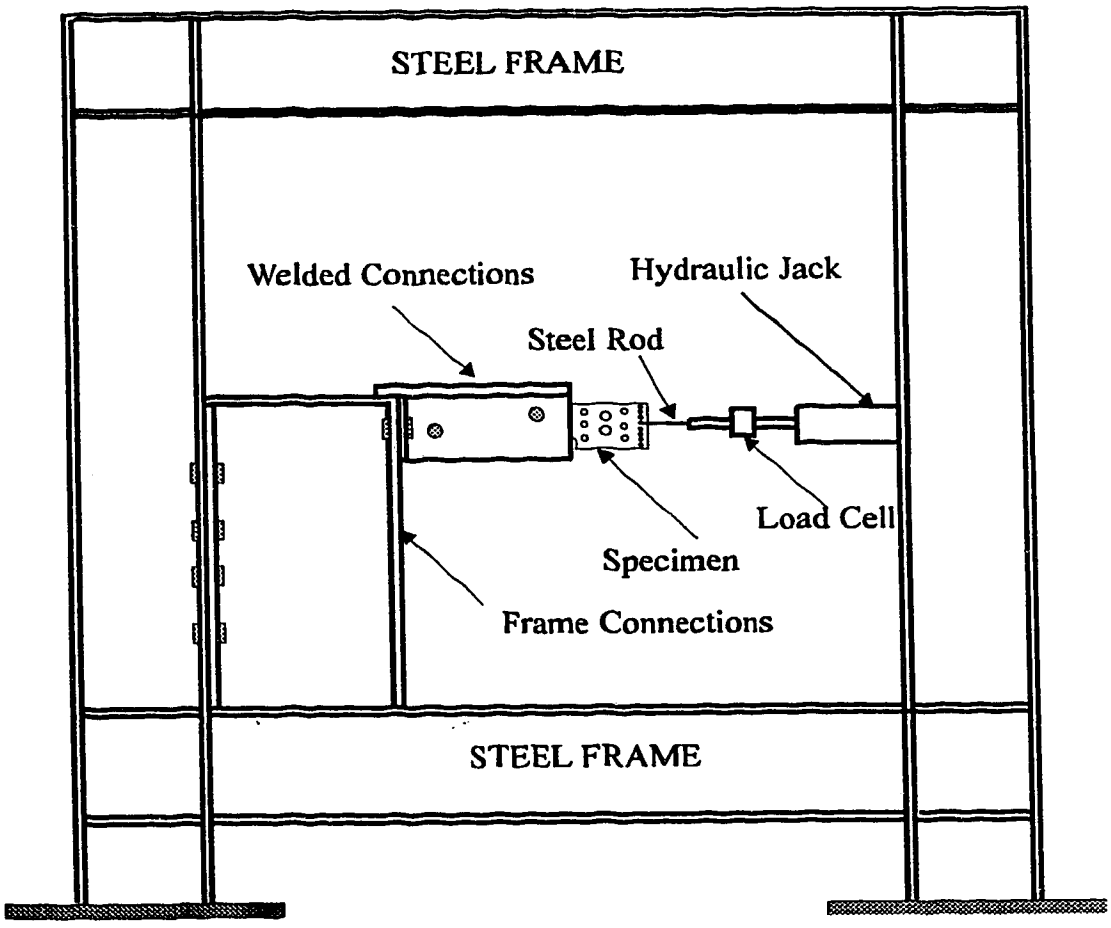

Figure 2.5 Shear connector test loading frame and set-up

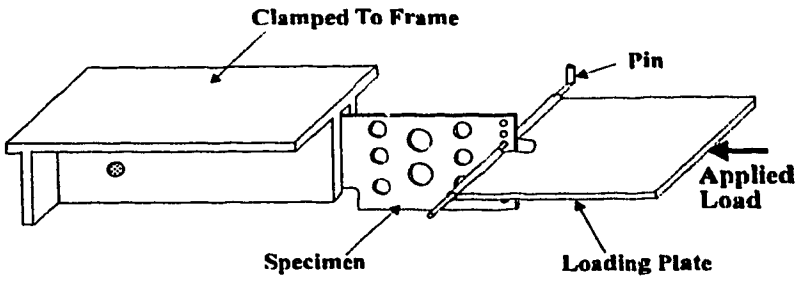

Figure 2.6(a) Compression test set-up

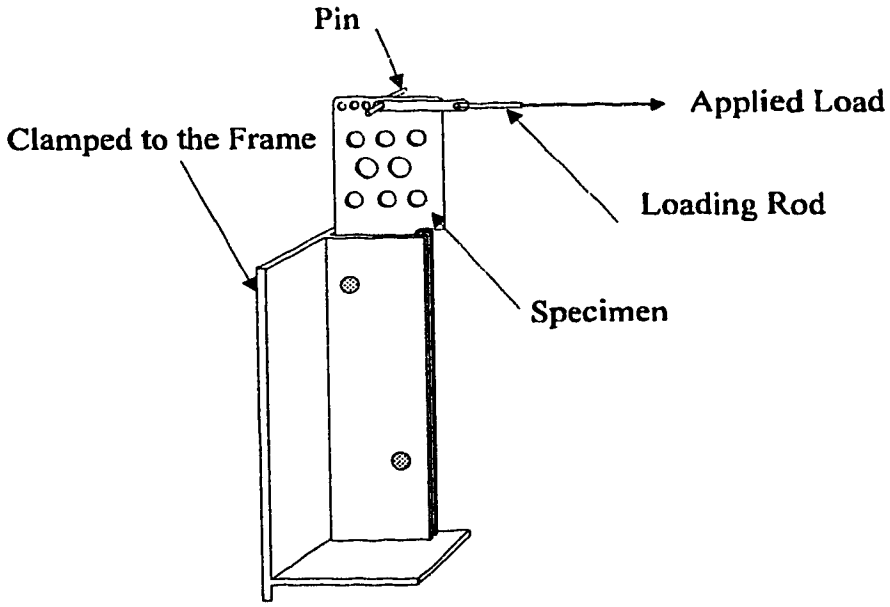

Figure 2.6 (b) Shear test set-up

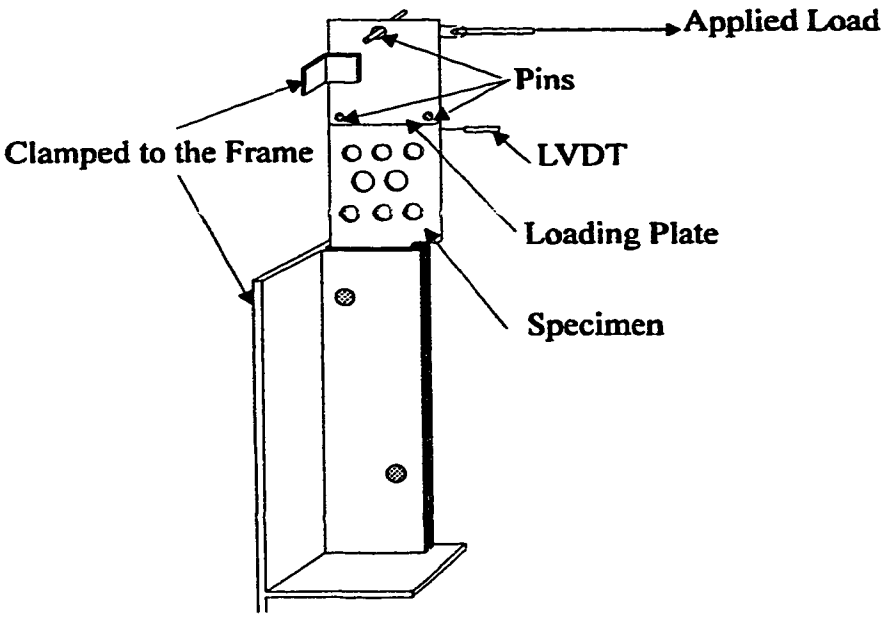

Figure 2.6 (c) Bending test set-up

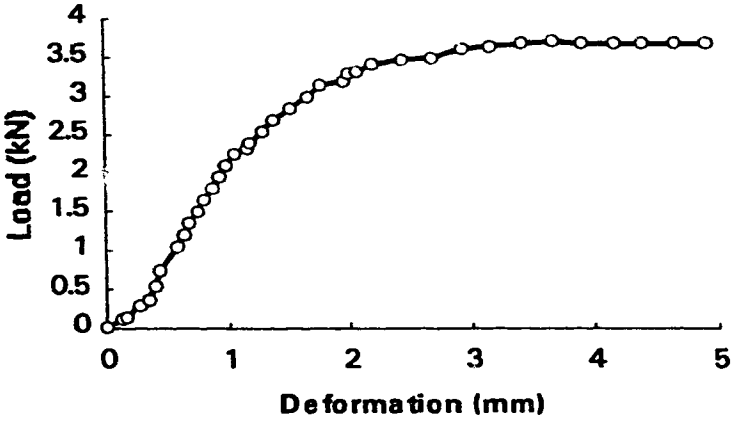

Figure 2.7(a) Tension test load-deflection curve, specimen S3

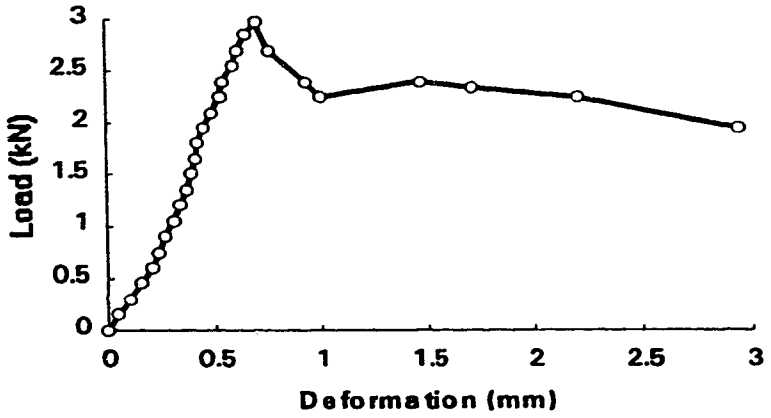

Figure 2.7(b) Compression test load-deflection curve, specimen S16

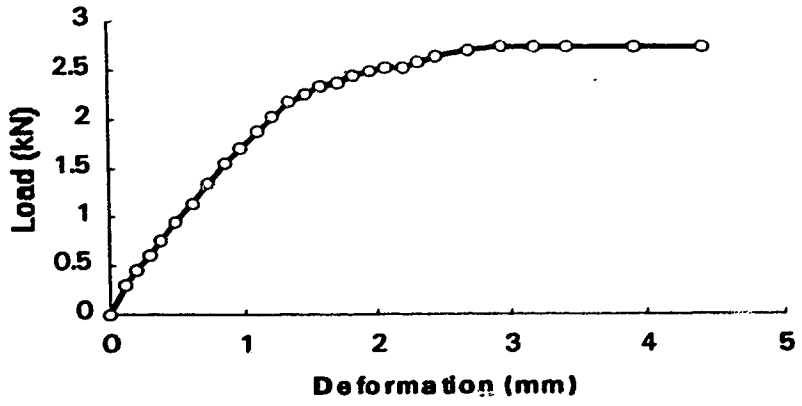

Figure 2.7(c) Shear test load-deflection curve, specimen S35

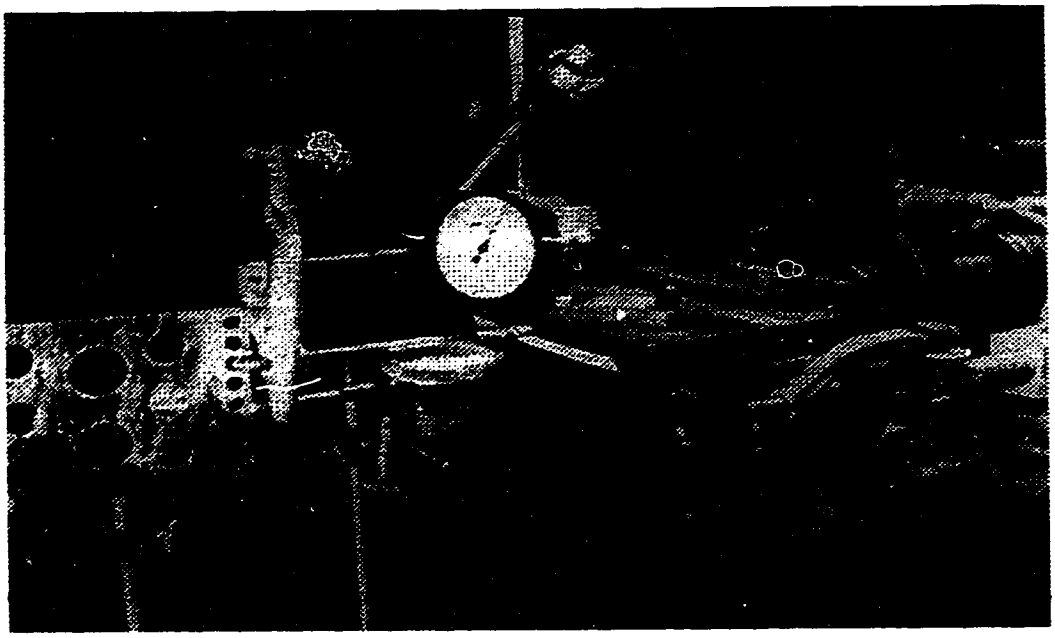

Plate 2.1 Tension test set-up

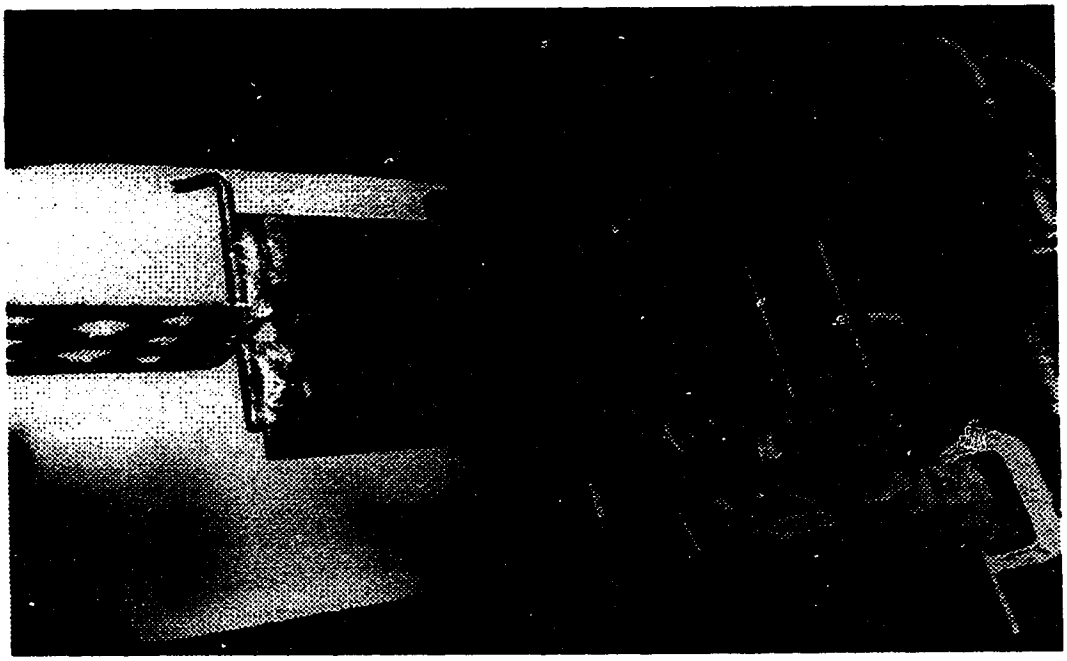

Plate 2.2 Compression test set-up

Plate 2.3 Specimen failed in compression

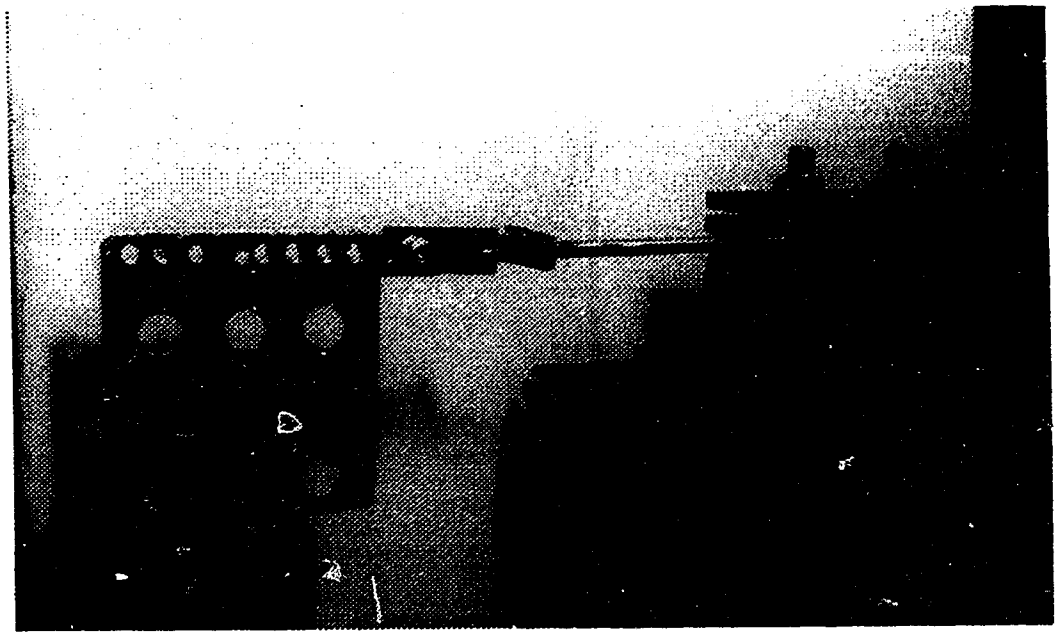

Plate 2.4 Shear test set-up

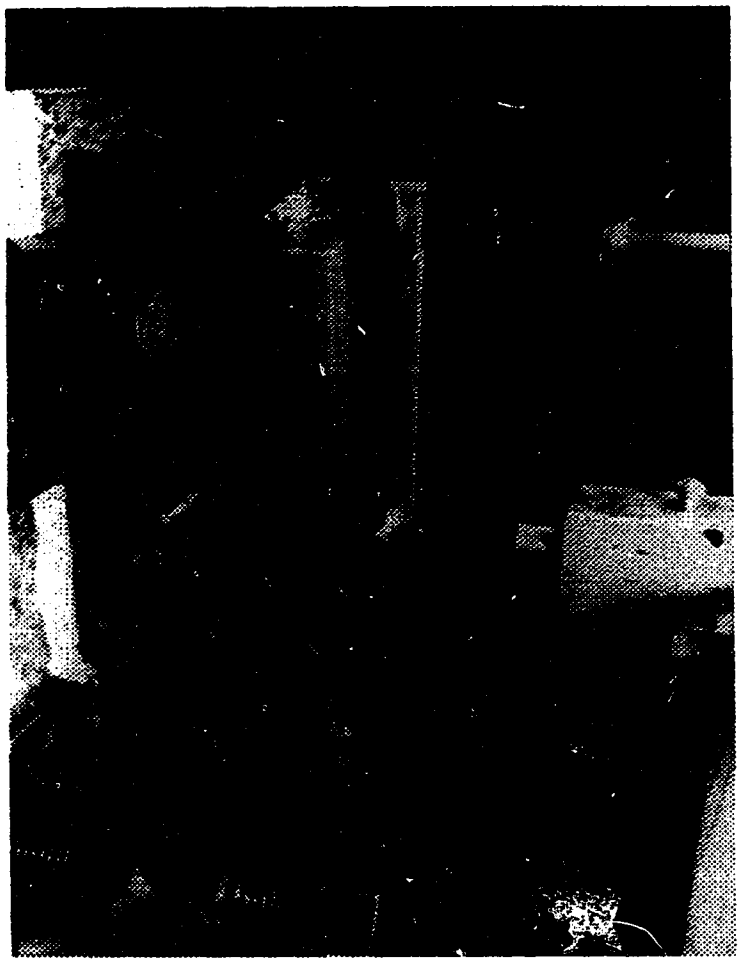

Plate 2.5 Bending test set-up

CHAPTER THREE
EXPERIMENTAL PROGRAM

3.1 Introduction

The literature review indicated that few tests had been conducted on shear connected cavity walls and little information was available on the evaluation of the stiffness and the ultimate load capacity for cavity walls subjected to eccentric vertical loading. The existing information related only to the performance of the connector. In order to evaluate the performance of the assembly, a test program was undertaken.

The experimental program included two phases - the full scale wall tests and the corresponding material tests. In the material tests, both the strengths and the deformation properties of the masonry assemblages were examined. In the full scale wall tests, a total of nine cavity wall tests was conducted. The experimental investigation was designed to observe the effects of the loading eccentricities by changing the magnitude and direction. Other parameters affecting the behaviour of the cavity walls were studied numerically and will be discussed in Chapter Five. The details of the test program are described in this chapter along with the test results and discussion.

3.2 Materials and Material Tests

A full suite of ancillary tests were conducted on units and prisms from both the blocks and bricks used in the experimental program. The materials used in material tests and full scale wall tests were locally supplied in the Edmonton, Alberta area.

3.2.1 Concrete Masonry Units

Standard 200 mm hollow concrete block units were used throughout the tests. Figure 3.1(a) to 3.1(c) show the dimensions and the configuration of the regular stretcher, the half and single corner of such units. Table 3.1 lists the physical properties of such units supplied by the manufacturer where the nominal compressive strength is 15 MPa (H/15/C/O).

Five regular units with a nominal dimension of 200 × 200 × 400 mm were tested for uniaxial compressive strength. A typical failure pattern is shown in Plate 3.1. Test results are summarized in Table 3.2 . The mean of the strength is 17.35 MPa and the standard deviation is 2.49 MPa.

Three regular units were tested to examine their deformation properties. The deformation was measured using a Twc-inch Demec Gauge. During the test, one specimen experienced early cracking at a load of 25 kN. The measuring point spalled off. No measurement was recorded for this specimen. The modulus of elasticity of the units was derived from the test results and is listed in Table3.3 where the mean value is 16088 MPa.

3.2.2 Concrete Masonry Prisms

Since the concrete block wythes of the cavity walls were constructed with two cores grouted vertically from the top to bottom, two types of specimens were tested for the properties of concrete masonry prisms - grouted prisms and ungrouted prisms.

- Hollow Block Prisms

Five ungrouted concrete block prisms (hollow block prisms) were tested for the uniaxial compressive strength, f'_m. The specimens were five courses in height and one unit

in length and were fabricated with mortar laid along the two face shells as well as two side-end webs. This mortar bedded area was taken into account when deriving the compressive strength from the ultimate loads. At the ultimate loads, the prisms were vertically separated into pieces - a typical splitting failure pattern as shown in Plate 3.2. The test results of compressive strengths for hollow block prisms f'_m are listed in Table 3.4 where the mean of f'_m is 19.30 MPa and the standard deviation is 2.62 MPa.

Three hollow concrete block prisms with the same dimensions were tested to determine the modulus of elasticity of the masonry assemblage. The specimens were five courses in height and one unit in length. The uniaxial deformation of the prisms was measured with a 200 mm Demec Gauge. The measuring length on the prisms incorporated both the units and the mortar layer. The test results are listed in Table 3.5. The mean of the values of the modulus of elasticity of hollow block prism is 15606 MPa.

- Grouted Prisms

Five grouted concrete block prisms were tested for uniaxial compressive strength. The specimens were five courses in height and one unit in length. The typical failure pattern was a split off face shell as shown in Plate 3.3. The test results are listed in Table 3.6 where the mean strength is 10.55 MPa and the standard deviation is 1.01 MPa. As can be seen from Tables 3.3 and 3.6, grouting increased the ultimate load capacities while the strength obtained from the grouted prism test is lower than that obtained from the hollow prism test since they were based on a different cross-sectional area. The lower strength of the grouted prisms may be attributed to the voids in grouted masonry, differential shrinkage and creep between units and grout material as well as differences in stress-strain behaviour between units and the grout material (Glanville and Hatzinikolas 1989).

Three grouted concrete block prisms with the same dimensions were tested to determine the modulus of elasticity of grouted masonry assemblages. The Demec Gauge

with 200 mm gauge length was used to measure the uniaxial deformation. The modulus of elasticity obtained from the tests are listed in Table 3.5. The mean is 8551 MPa.

3.2.3 Burnt Clay Units

Locally supplied burnt clay brick units were used to construct the brick wythes of the cavity walls and were used for the brick material tests. Figure 3.1(d) shows the dimensions and the configuration of the brick unit. The physical properties of the brick units provided by the manufacturer are summarized in Table 3.7.

Five brick units were tested for uniaxial compressive strength. Table 3.8 shows the test results. The mean strength was 29.36 MPa and the standard deviation was 3.30 MPa.

3.2.4 Burnt Clay Prisms

Five specimens were tested for uniaxial compressive strength of burnt clay brick prisms. The specimens were five courses in height and one unit in length. The typical failure pattern was vertical splitting of the prism. Table 3.9 lists the test results. The mean value of the compressive strength is 18.13 MPa. The standard deviation is 4.2 MPa.

Three brick prisms with the same dimensions were tested to determine the modulus of elasticity of the brick assemblage. The uniaxial deformation was measured with a Two-inch Demec Gauge. The test results are summarized in Table 3.10 where the mean value is 6536 MPa.

3.2.5. Mortar, Grout and Reinforcement

Premixed type S mortar was used to construct the prisms and the walls. Six 50 × 50 × 50 mm cubes were cast to test the strength. The results are summarized in Table 3.11 where the mean of the values is 10.9 MPa and the standard deviation is 1.24 MPa.

The grout was mixed on site. The weight ratio between cement, sand and pea gravel is 1 : 3.92 : 2.78. The water cement ratio is 1 : 1. Five 75 × 75 × 150 mm grout prisms were cast and tested to determine the compressive strength of the grout. The results are shown in Table 3.12. The mean grout strength is 29.4 MPa and the standard deviation is 5.6 MPa.

Each cavity wall was reinforced vertically with two 15M rebars. The specified strength of the rebar was 300 MPa. The locations of the rebars will be described later. All the cavity walls were reinforced horizontally with # 9 wire joint reinforcement, placed every third course. The configuration of the joint reinforcement is shown in Fig. 3.2.

3.3 Full Scale Cavity Wall Tests

3.3.1 Specimens

Nine reinforced masonry cavity wall specimens were constructed and tested. All the specimens were constructed with the same materials and of the same dimensions except the cavity width. Each cavity wall consisted of two wythes connected with shear connectors. The back-up wythe was built with concrete blocks and the brick wythe was built with burnt clay bricks. The specimens were 24 courses high and 1.2 m wide. The total height between the top and the bottom hinges of the loading apparatus was around 5.28 m. The concrete block wythes were 190 mm thick and the brick wythes were 90 mm thick. The cavity widths were either 75 mm or 100 mm as labelled in Table 3.13.

The specimens were constructed with type S mortar. The thickness of the mortar joints was 10 mm. The concrete block wythes were mortared only at the face shells while the brick brick wythes were laid in a full mortar bed. Horizontal reinforcement was placed in the mortar joints of the block wythes at every third course. The second core from the each side of the block wythe was grouted and each grouted core was reinforced with one

15M longitudinal reinforcement. The grouting for each core was completed in two stages with 12 courses grouted at each stage.

The shear connectors discussed in Chapter Two were used for all the specimens. The connectors were placed with the same pattern and it is as shown in Figure 3.3. The vertical and horizontal maximum spacing was 600 mm and 800 mm respectively. More connectors were placed at the top and the bottom ends of the specimens in order to account for the anticipated higher loads in these locations.

In order to move the specimens into the test machine, the block wythes of the walls were built on top of 1300 × 240 × 310 mm concrete pedestals while the brick wythes were built on 1300 ×150 × 150 × 20 steel angles overhanging on the concrete pedestals. The pedestals were designed with embedded bolts to allow the specimens to be moved as well as to be loaded at the bottoms.

For specimens W6, W8, and W9, a loading eccentricity of 90 mm was added at the top of each specimen. This meant that the loading point was at the edge of the block wythe. To distribute the load along the cross-section and to ensure local bearing resistance, 13 mm thick steel plates were placed at the top of these three specimens. The steel plates were welded to the longitudinal reinforcement which was placed at the grouted cores.

3.3.2 Test Set-Up

Figure 3.4 shows the set-up for the full scale wall tests. At the bottom end, a hinge was placed along the bottom line of the specimen. Its centre line was carefully aligned with the centre line of the block wythe. The hinge was 103 mm in width, 105 mm in height, and 1265 mm in length. A thin layer of plaster was laid at the top of the hinge and the concrete pedestal sat on the plaster. The plaster layer was used to keep an uniform contact between the concrete pedestal and the bottom hinge. After the specimen was

positioned, several bolts were placed underneath the steel angle to support the brick wythe. They were removed once the loading started.

A steel channel was placed on the top of the specimen. Again, a plaster layer was placed between the top of the specimen and the channel to allow uniform contact between them. On the top of the channel was a hinge assembly which was bolted at the two side-ends to the channel. To prevent lateral movement at the top of the specimen, two parallel braces were used built from steel angles. Each brace was connected to the centre of the hinge at one end and to an independent column at the other end. The column base was fixed to the load floor.

The vertical load was applied by a 6600 kN MTS machine. The moment was applied at the top end of the specimen by shifting the position of the hinge on the channel. The moment at the bottom end of the specimen was applied through a built-up loading arm which was bolted to the concrete pedestal at one end as shown in Plate 3.4. At the other end of the loading arm, a manually controlled hydraulic ram was used to apply upwards or downwards loading in accordance with the desired direction of the moment. Plate 3.5 shows the loading frame for the hydraulic ram.

3.3.3 Instrumentation

The vertical load was measured directly by the MTS machine. The load on the loading arm was measured by a load cell. The horizontal displacement of the specimen was recorded by eleven LVDT's with five on the block wythe side and six on the brick wythe side. On the top of each wythe of the specimen, one LVDT was attached to measure the vertical movement of the specimen. Three rotation meters were mounted on the specimen with one at the top and one at the bottom of the block wythe and one at the bottom of the brick wythe.

3.3.4 Test Procedure

After 28 days of curing, the specimens were moved into the loading frame by a 10 tonne crane, one specimen at a time.

In order to control the magnitude and ratio of the moments at the bottom and the top of the specimen, the load applied at the loading arm was controlled by a pre-calculated load ratio for each load increment throughout the test. The vertical loading from the MTS machine was carried out by stroke control. For the specimens loaded in double curvature, the initial loading condition was carefully controlled to create the double curvature situation.

Throughout each test, loads, displacements and rotations were monitored and recorded automatically by a computer. This was done through a Fluke data acquisition system which was connected with the measuring devices.

3.3.5 Test Results and Discussion

3.3.5.1 Specimen W1

This specimen had a 75 mm cavity and was loaded at both ends of the wall with an eccentricity of t/3 (63.3 mm) measured from the centre of the cross-section of the block wythe to the direction of away from the brick wythe. That is $e_1/e_2 = 1$. The specimen deflected towards the brick wythe in single curvature.

Figure 3.5 shows the load versus mid-height deflection curve of the block wythe. As can be seen, the deflection response of the specimen was fairly linear up to a load level of 320 kN, i.e., the change of the slope of the response curve was small. At a load about 300 kN, the first crack in the brick wythe was observed at the number 34 mortar joint (mid-height) where a V-Tie was embedded. As the load increased, more cracks occurred

at the mortar joints of the brick wythe at, or close to, the positions of the shear connectors. The brick wythe was finally separated into several rigid brick assemblages by large horizontal cracks at the mortar layers. In the block wythe of the specimen, cracking started at the mid-height mortar joint. More cracks at the mortar joints occurred as the load increased. Horizontal cracks also formed on the tension side of the concrete block wythe. These cracks formed when the bond between the mortar and units failed. The ultimate load was 451 kN. After reaching the ultimate load, the specimen could still sustain the load at a high level even though large deformations had developed. The final failure was due to the large deflection which was about 40 mm at mid-height. The failure was ductile.

Figure 3.6 shows a comparison of the response curve between specimen W1 and a single masonry wall with the same materials and the same dimensions conducted by Goyal, et al. (1993). It can be observed that the effect of the interaction between the block wythe and the shear connected brick wythe is significant since both the strength and the initial stiffness of the wall were improved.

3.3.5.2 Specimens W2 and W5

Specimen W2 had 75 mm cavity and was loaded with an eccentricity of t/3 (63.3 mm) from the centre of the cross-section of the block wythe to the direction of away from the brick wythe only at the top of the specimen. That is $e_1/e_2 = 0$. The specimen deflected in single curvature towards the brick wythe.

Figure 3.7 shows the load versus mid-height deflection curve of specimen W2. As shown in the Figure, the change of the slope of the deflection curve was small before the load reached 500 kN. After this load level, the deflection developed at a more rapid rate. The cracking in the brick wythe started at the number 50 mortar layer (Height = 3.9 m) which was one brick layer away from a shear connector position. The subsequent cracking in the brick wythe occurred at the mortar joints at, or close to, the shear connector

positions. The cracks in the block wythe of the specimen were also at the mortar joints and were distributed in the upper part of the block wythe. Cracking in both wythes was due to debonding as shown in Plate 3.6 where debonding between the mortar joints and the brick units can be observed. The ultimate load of the specimen was 818.0 kN.

Specimen W5 was designed with the same dimensions and the same loading conditions of specimen W2. The test results were similar to those of the specimen W2. The ultimate load was 815.5 kN.

3.3.5.3 Specimen W3

This specimen had 75 mm cavity and was loaded with an eccentricity of t/3 (63.3 mm) measured from the centre of the cross-section of the block wythe to the direction of towards the brick wythe only at the top end of the specimen. That is $e_1/e_2 = 0$. The specimen deflected in single curvature towards the block wythe.

The load versus mid-height deflection curve for specimen W3 is shown in Figure 3.8. As shown in the Figure, the deflection response was almost linear up to a load of 350 kN. The deflection increased more rapidly after this load level. At this load level a crack occurred in the brick at a height of 3.8 m from the bottom of the specimen. The crack went through the brick wythe and no other cracks formed in the brick wythe until complete failure of the specimen occurred. The cracking in the block wythe started at the number 17 mortar joint (height = 3.7 m). When approaching failure, cracks were observed at all the mortar joints of the upper part of the block wythe. The ultimate load was 651.9 kN. After reaching the ultimate load, the specimen sustained the load at a high level.

Comparing specimen W3 with specimen W2, the only significant difference lay in the direction of the loading eccentricity. The specimen W2 was loaded with the

eccentricity away from the brick wythe while the specimen W3 was loaded towards the brick wythe. The ultimate load of specimen W3 was, however, twenty percent less than that of specimen W2. Since we have two specimens (specimens W2 and W5) with similar test results for the latter case, and since the loading eccentricity of specimen W3 was towards the brick wythe which was closer to the centroid of the cross-section of the cavity wall, we may conclude that the ultimate load capacity of specimen W3 was lower than expected. This may be due to material property variation and the variation in the efficiency of the shear connector working under various loading conditions.

3.3.5.4 Specimen W4

This specimen was constructed with a 75 mm cavity and was loaded with an eccentricity of t/3 (63.3 mm) from the centre of the cross-section of the block wythe at the both ends of the wall with opposite directions. That is $e_1/e_2 = -1$. The loading at the lower end of the specimen was maintained constant after the primary load reached 800 kN.

Figure 3.9 shows the deflection shapes along the height of the block wythe at several load levels. As shown in the figure the specimen deflected initially in double curvature. As the load increased, unwinding of the specimen to the direction of the upper end could be observed but was not significant. After the load reached 800 kN, the upper curve developed more quickly since the upper end had larger moment. During the test, a crack was observed at the number 57(height = 4.4 m) mortar joint of the brick wythe. For safety reasons, the lower part of the brick wythe and the block wythe were not closely observed. At the ultimate load of 1200 kN, the face shells of the blocks at the top end of the specimen were spalled off as shown in plate 3.7. Crushing of the block was sudden and without warning. The loading dropped off quickly from the ultimate point and the specimen reached failure. No descending part of the response curve was captured.

Comparing specimens W1, W2 and W4, the properties of the specimens and the magnitudes of the loading eccentricities were the same, but the ratios of e_1/e_2 were different, +1, 0, and -1. The corresponding values of the ultimate load capacities were 451 kN, 818 kN, and 1200 kN respectively. As can be seen, the capacities of the specimens were strongly influenced by the end eccentricity ratios. On the other hand, the ductility decreased as the end eccentricity ratio changed from the positive to the negative values.

3.3.5.5. Specimen W6

Specimen W6 had a 75 mm cavity and was loaded at both ends of the specimen with an eccentricity of t/2 (90 mm) measured from the centre of the cross-section of the block wythe towards the brick wythe. That is $e_1/e_2 = 1$. The specimen deflected in single curvature towards the block wythe.

The load verses mid-height deflection curve is shown in Figure 3.10. It can be observed that the deflection increased at a faster rate at load levels higher than 150 kN. Two cracks in the brick wythe were observed at the mortar layers at mid-height and at a height of 4.5 m (number 59 mortar layer counted from the bottom). When approaching failure, these two mortar joints were completely debonded. In the block wythe, cracks appeared at several mortar joints of the middle part of the specimen. The two cracks at the mid-height, however, were the most developed. One of the cracks spread into the block unit as shown in Plate 3.8. The ultimate load was 251.4 kN.

3.3.5.6 Specimen W8

This specimen had a 75 mm cavity and was loaded at both ends of the specimen with an eccentricity of t/2 (90 mm) measured from the centre of the cross-section of the block wythe in the direction of away from the brick wythe. That is $e_1/e_2 = 1$. The specimen deflected in single curvature towards the brick wythe.

Figure 3.11 shows the load-displacement response of the specimen. As can be observed from the figure the response curve was approximately linear at the initial loading stage. When the load reached about 160 kN, a big crack appeared at the number 58 mortar joint at mid-height of the brick wythe. The whole mortar joint cracked through immediately after. The deflection corresponding to this cracking was about 9 mm. Cracks in the block wythe also occurred at mid-height. After this, the deflection increased rapidly while the load remained constant but sustained for quite a long time. The ultimate deflection was about 90 mm, ten times the deflection at the ultimate load. The ultimate load capacity was 166 kN.

Unlike other specimens, the curvature of the response of specimen W8 shows a sudden change at the ultimate load as can be seen in Figure 3.11. This sudden change may have been caused by local buckling of the shear connectors. This will be discussed further in Chapter Four.

Comparing specimen W6 with W8, The physical properties of the specimens and the loading conditions were the same except the direction of the eccentricities. Specimen W6 was loaded with an eccentricity towards the brick wythe while specimen W8 was loaded away from the brick wythe. The ultimate load capacity of specimen W6 was higher than that of specimen W8 indicating the direction of the loading eccentricity may affect the behaviour of cavity walls.

3.3.5.7 Specimen W7

Specimen W7 had a 100 mm cavity and was loaded at both ends of the wall with an eccentricity of t/3 (63.3 mm) measured from the centre of the cross-section of the block wythe towards the brick wythe. That is $e_1/e_2 = 1$. The specimen deflected in single curvature towards the block wythe.

The load versus mid-height deflection curve of the block wythe is shown in Figure 3.12. The curve was approximately linear up to a load of 320 kN. The curve then gradually showed increasing nonlinearity and reached the ultimate load at 424.0 kN.

3.3.5.8. Specimen W9

The specimen W9 had a 75 mm cavity and was loaded with an eccentricity of t/2 (90 mm) measured from the centre of the cross-section of the block wythe at the both ends of the specimen in opposite directions. That is $e_1/e_2 = -1$. The moment ratio between the top end and the bottom end was kept unchanged throughout the test.

The deflection shapes along the height of the specimen are plotted at different load levels and shown in Figure 3.13. As can be seen, the specimen initially deflected in double curvature. As the load increased, unwinding of the specimen occurred towards the lower end of the specimen. This unwinding phenomenon was not significant and the specimen remained in double curvature until the failure. At a load level of 822 kN, compression failure started at the face shells of the block units at the top end of the block wythe. The face shell spalled off as shown in Plate 3.9. The failure was brittle. No descending part of the curve was obtained in the test. The ultimate load capacity was 822.9 kN

3.3.6 Summary of the Test Results

A total of nine full scale cavity masonry walls was tested. The physical properties, the loading conditions and the ultimate load capacities are summarized in Table 3.14. The test results and the observations led to the following conclusions:

(1). The behaviour of the cavity walls was affected by the magnitude of the loading eccentricities as well as the end eccentricity ratios. The ultimate load decreased while the ductility increased as the magnitude of the eccentricities increased and as the value of the end eccentricity ratios changed from -1 to +1.

(2). The ultimate load capacity was also affected by the directions of the loading eccentricities, either towards or away from the brick wythes. The effects of this influence will be discussed in Chapter Five.

(3). At least two failure patterns were captured by the tests. Specimens W4 and W9, which were loaded with $e_1/e_2 = -1$, failed in a brittle manner in a material compression failure pattern. The other specimens, which were loaded with either $e_1/e_2 = 0$ or $e_1/e_2 = 1$, failed by inelastic instability due to large deformations caused by the initial moments, the vertical loads and the second order effects. Specimen W8, however, may be an exception since its response changed direction suddenly at about the ultimate load level. This failure pattern will be discussed further in Chapter Four.

(4). Cracking of the specimens in both the brick wythe and the block wythes occurred at the mortar layers. The nature of the cracking was identified as debonding between the units and the mortar joints. Most cracks developed within the mortar layers but a few of the cracks in the block wythes extended into the units. Cracking in the brick wythes was concentrated at a few mortar layers near the locations of the shear connectors. While, cracking in the block wythe was more uniformly distributed in several mortar layers since the block wythes were reinforced and partially grouted.

(5). The load-deflection responses were approximately linear up to a load level of at least $0.53\ P_u$.

(6). The reinforced cavity walls being tested exhibited good ductility except when loaded in double curvature.

(7). Compared with single masonry walls, the ultimate load capacity and the initial stiffness of the shear connected cavity wall increased significantly.

Table 3.1 Physical Properties of Concrete Block Units

Properties	200 mm Standard Block H/15/C/O
Width	190 mm
Length	390 mm
Height	190 mm
Minimum Face Shell Thickness	32 mm
Gross Area	74100 mm^2
Net Area	41500 mm^2
Unit Mass(kg)	13.4
Moisture Content	10.2
Absorption(%)	14.3

Table 3.2 Compressive Strength of Concrete Block Units

Specimens	Ultimate Load kN	Ultimate Strength * MPa
1	591.0	14.24
2	756.0	18.21
3	638.0	15.37
4	776.0	18.70
5	842.0	20.29
AVERAGE	720.6	17.35

* Based on net area of 41500 mm^2.

Table 3.3 Modulus of Elasticity of Concrete Block Units

Specimen	Modulus of Elasticity MPa
1	14105
2	18072
3	N/A*
AVERAGE	16088

* Specimen cracked at P=25 kN.

Table 3.4 Compressive Strength of Hollow Concrete Block Prisms

Specimens	Ultimate Load kN	Ultimate Strength * MPa
1	504.0	15.59
2	725.0	22.42
3	575.0	17.79
4	660.0	20.42
5	644.0	19.92
AVERAGE	621.6	19.30

* Based on bedded area of 32328 mm^2.

Table 3.5 Modulus of Elasticity of Concrete Block Prisms

Specimens	Modulus of Elasticity of Grouted Prism* MPa	Modulus of Elasticity of Hollow Prism** MPa
1	8465	14040
2	8724	16320
3	8465	16460
AVERAGE	8551	15606

* Based on gross cross-sectional area of 72200 mm^2.

** Based on bedded area of 32328 mm^2.

Table 3.6 Compressive Strength of Grouted Concrete Block Prisms

Specimens	Ultimate Load kN	Ultimate Strength * MPa
1	782.0	10.55
2	749.0	10.11
3	788.0	10.63
4	693.0	9.35
5	898.0	12.12
AVERAGE	782.0	10.55

* Based on gross cross-sectional area of 74100 mm^2.

Table 3.7 Physical Properties of Burnt Clay Brick Units

Property	Burnt Clay Brick Units
Width	90 mm
Length	190 mm
Height	63 mm
Volume of Voids	25 %
Thermal Expansion Coefficient	3.6×10^{-6}
Weight per Unit	1.6kg
Weight of wall / Sq.m	140 kg

Table 3.8 Compressive Strength of Burnt Clay Brick Units

Specimens	Ultimate Load kN	Ultimate Strength * MPa
1	427.0	27.74
2	452.0	29.37
3	381.0	24.76
4	492.0	31.97
5	507.0	32.94
AVERAGE	451.8	29.36

* Based on net area of 15390 mm^2.

Table 3.9 Compressive Strength Of Burnt Clay Brick Prisms

Specimens	Ultimate Load kN	Ultimate Strength * MPa
1	298.0	19.36
2	226.0	14.68
3	230.0	14.94
4	258.0	16.76
5	383.0	24.89
AVERAGE	279.0	18.13

* Based on cross-sectional area of 15390 mm^2.

Table 3.10 Modulus of Elasticity of Burnt Clay Brick Prisms

Specimens	Burnt Clay Brick Prisms* MPa
1	6821
2	6529
3	6259
AVERAGE	6536

*Based on cross-sectional area of 15390 mm^2.

Table 3.11 Compressive Strength of Mortar

Specimens	Ultimate Load kN	Ultimate Strength * MPa
1	28.5	11.4
2	26.5	10.6
3	28.0	11.2
4	31.5	12.6
5	22.0	8.8
6	27.0	10.8
AVERAGE	27.3	10.9

Table 3.12 Compressive Strength Of Grout Material

Specimens	Ultimate Load(prism) kN	Strength (prism) MPa
1	152.5	27.11
2	120.5	21.42
3	193.5	34.40
4	197.0	35.02
5	163.5	29.07
AVERAGE	165.4	29.40

Table 3.13 Summary of Full Scale Wall Tests

Specimens	Slenderness	Cavity mm	Eccentricity	e_1 / e_2	Ultimate Load kN
W1	27.81	75	t / 3* (a)**	1	451.0
W2	27.82	75	t / 3 (a)	0	818.0
W3	27.81	75	t / 3 (t)**	0	651.9
W4	27.84	75	t / 3	-1	1200.1
W5	27.81	75	t / 3 (a)	0	815.5
W6	27.84	75	t / 2* (t)	1	251.4
W7	27.82	100	t / 3 (t)	1	424.0
W8	27.89	75	t / 2 (a)	1	166.0
W9	27.83	75	t / 2	-1	822.9

* t = Thickness of the wall. Here, t / 3 = 63.3 mm; t / 2 = 90 mm.
**(a) = away from brick wythe; (t) = towards brick wythe.

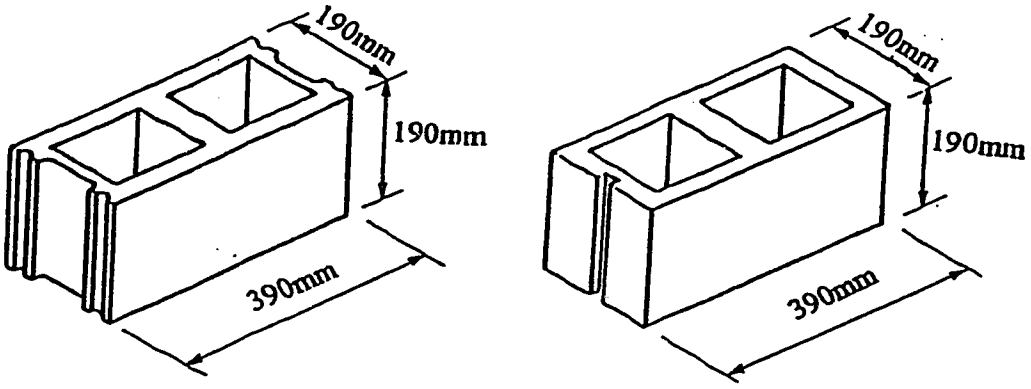

(a) 200 mm Standard Concrete Unit (b) 200 mm Concrete Corner Sash

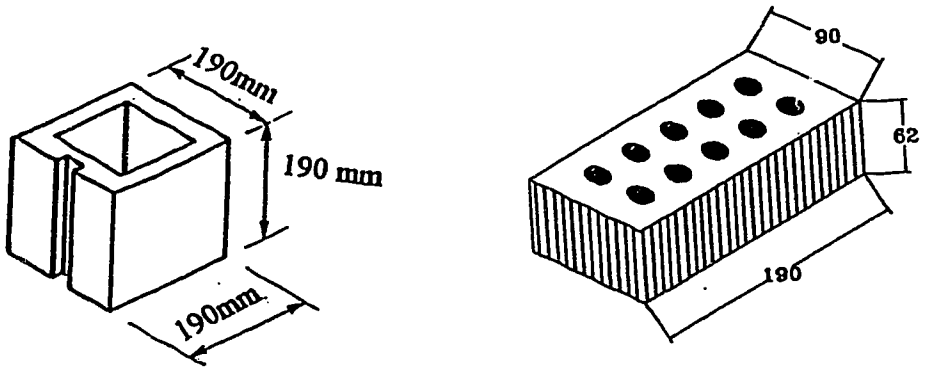

(c) 200 mm concrete half unit (d) Clay Burnt Unit (mm)

Figure 3.1 Dimensions of concrete block units and burnt clay unit

Figure 3.2 Ladder type horizontal reinforcement

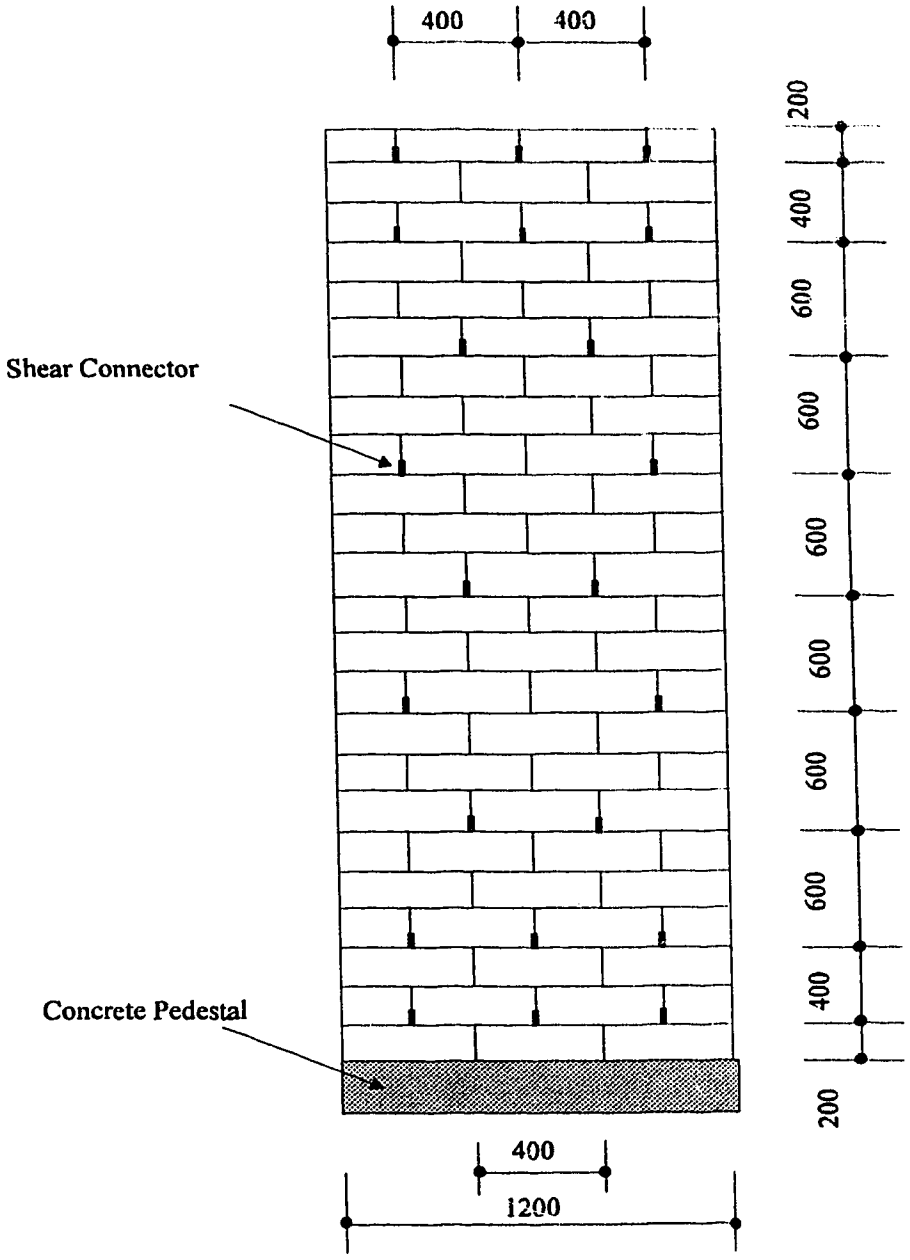

Figure 3.3 The pattern of placement of the shear connectors

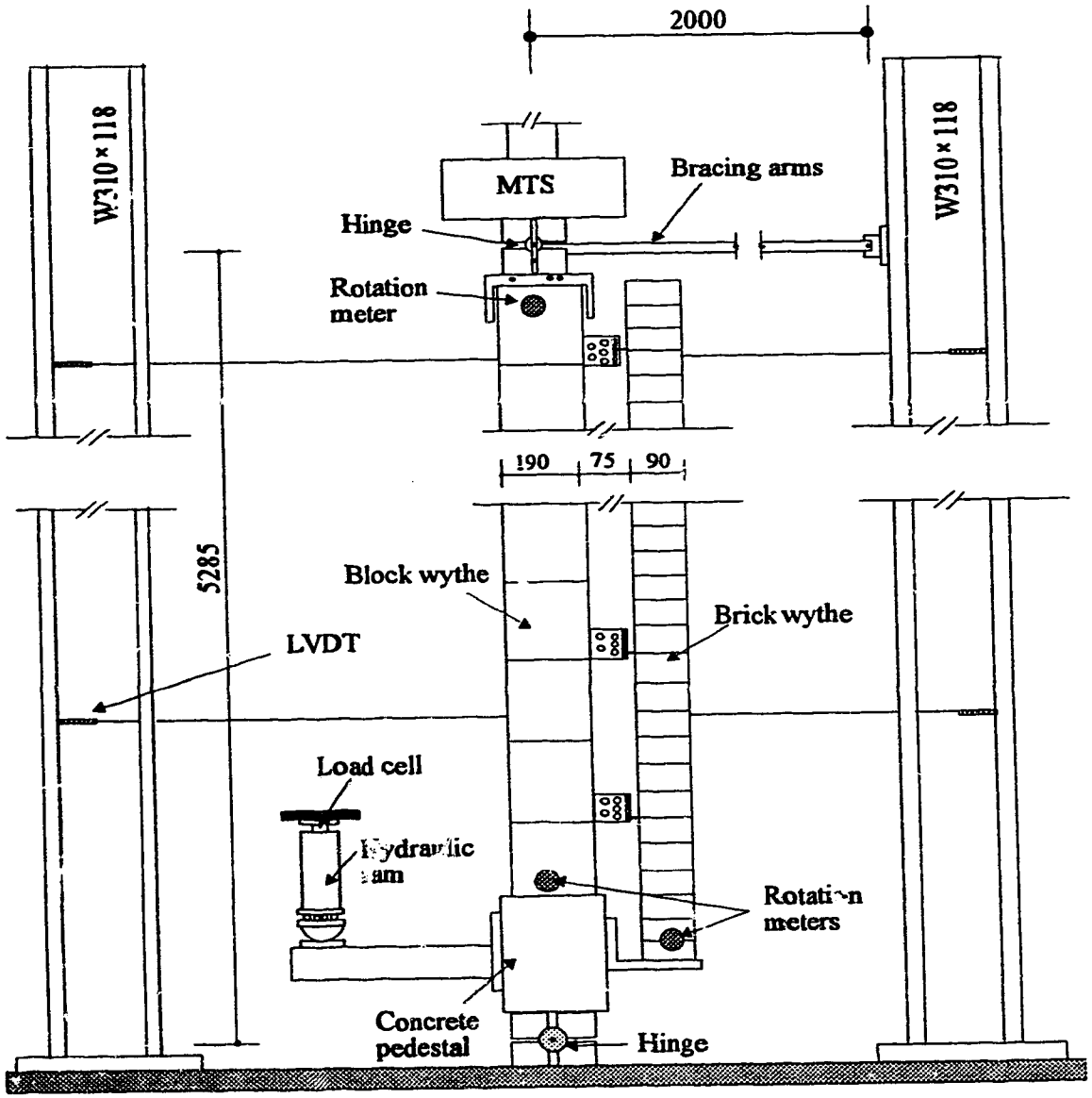

Figure 3.4 Test set-up and loading system

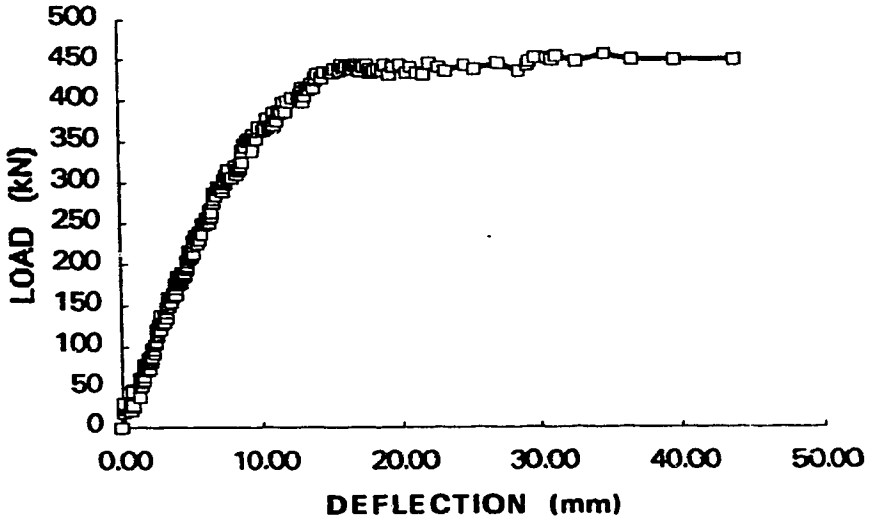

Figure 3.5 Load vs. mid-height deflection of specimen W1

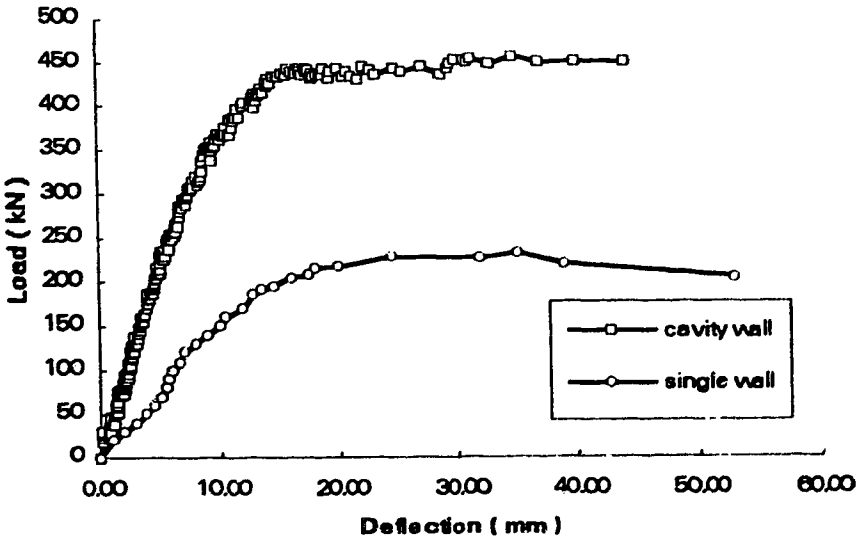

Figure 3.6 Load - deflection curves of single and cavity walls of W1

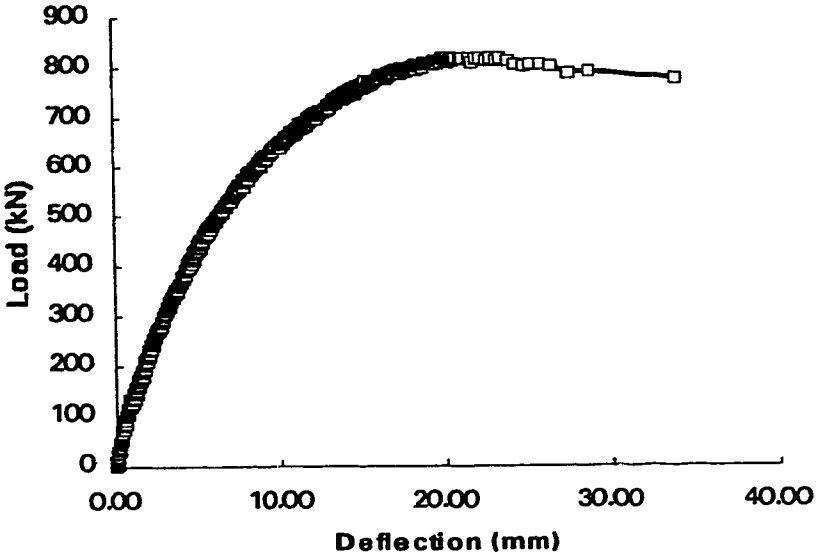

Figure 3.7 Load vs. mid-height deflection of specimen W2

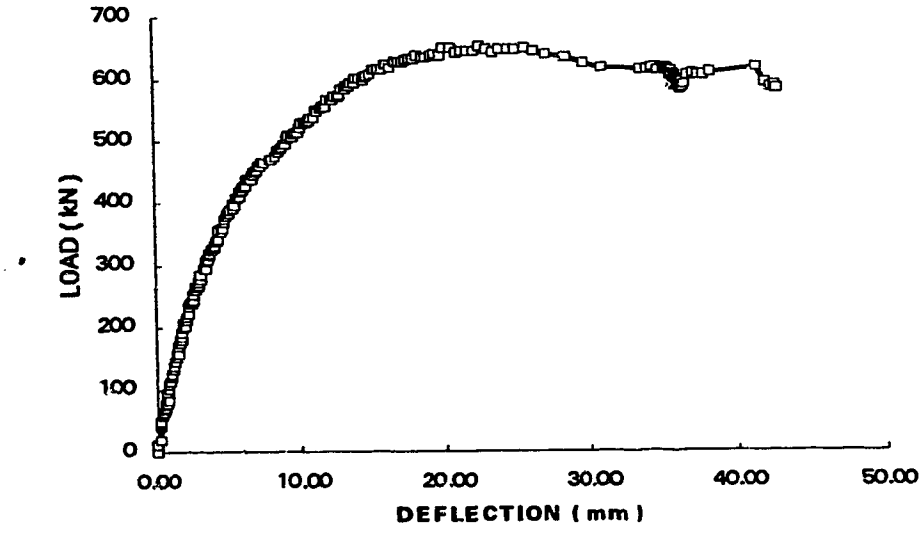

Figure 3.8 Load vs. mid-height deflection of specimen W3

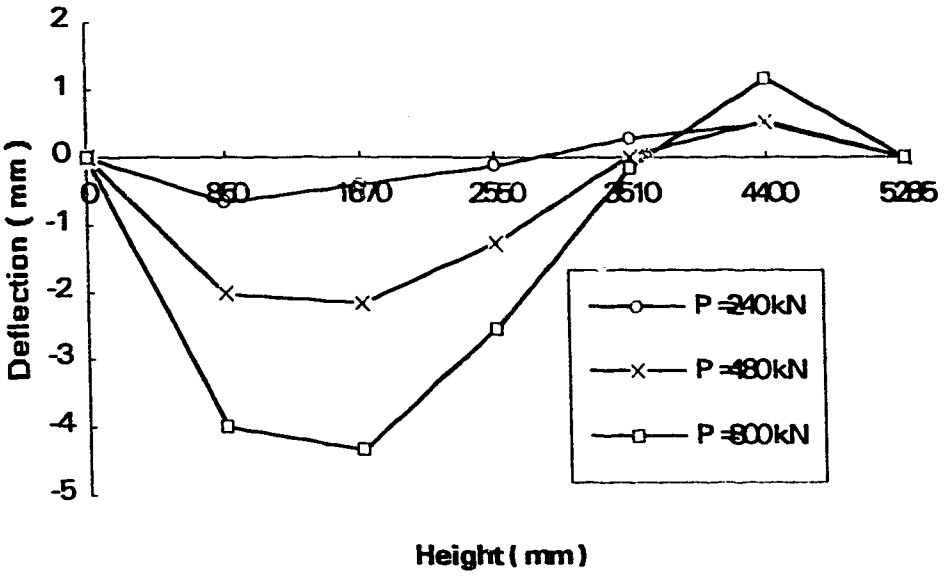

Figure 3.9 (a) Deflected shapes of specimen W4 (P ≤ 800 kN)

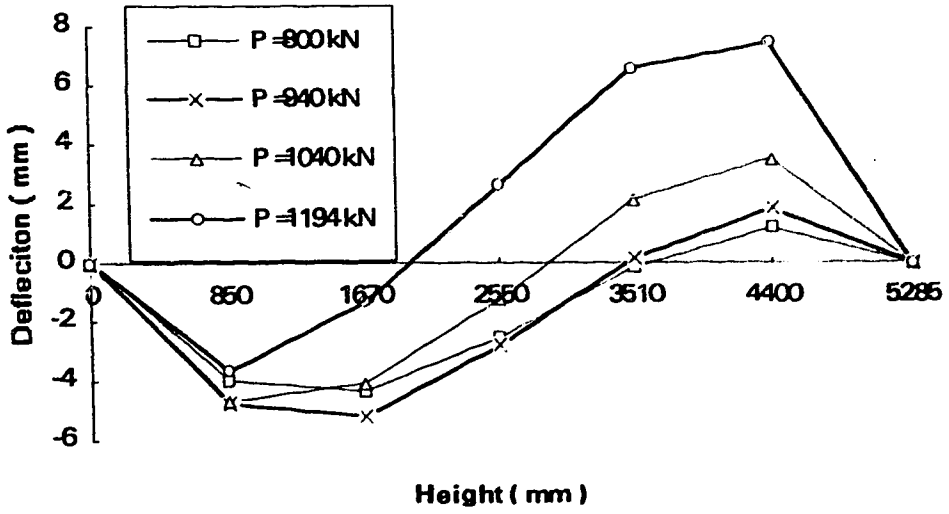

Figure 3.9 (b) Deflected shapes of specimen W4 (P ≥ 800 kN)

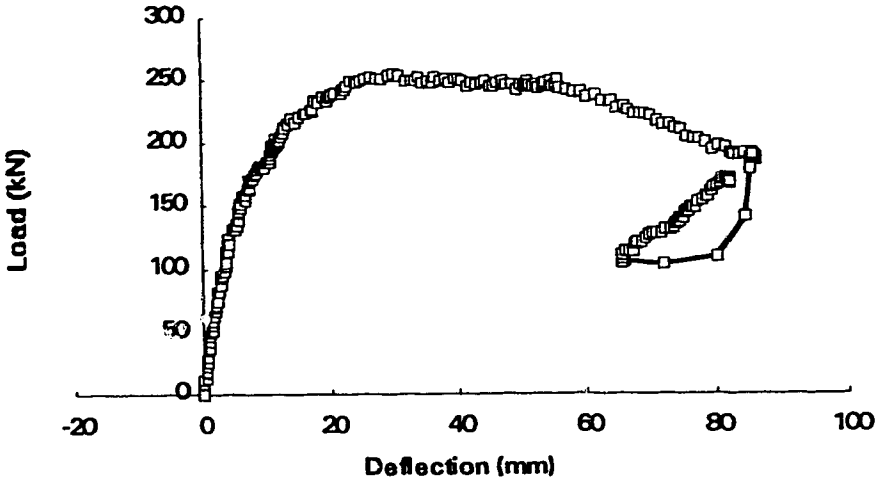

Figure 3.10 Load vs. mid-height deflection of specimen W6

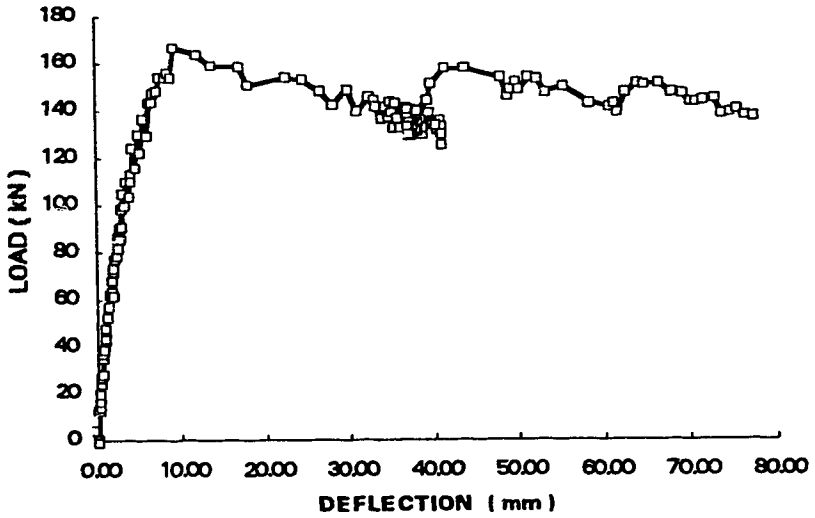

Figure 3.11 Load vs. mid-height deflection of specimen W8

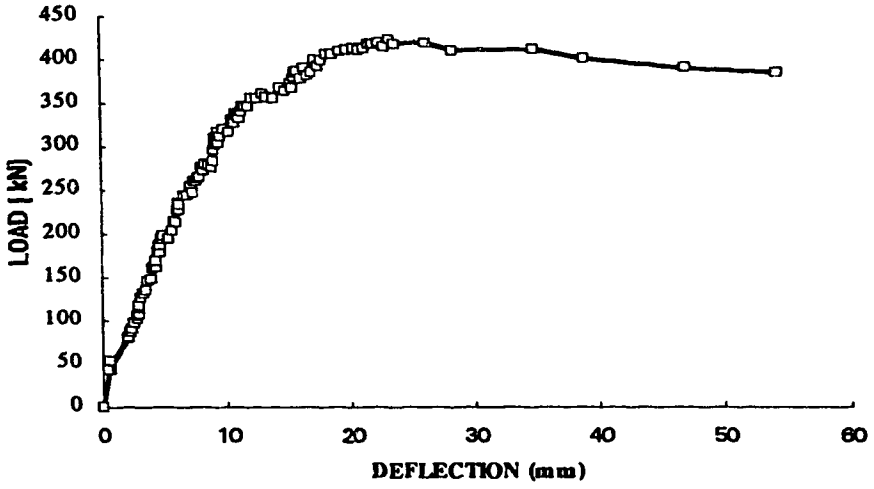

Figure 3.12 Load vs. mid-height deflection of specimen W7

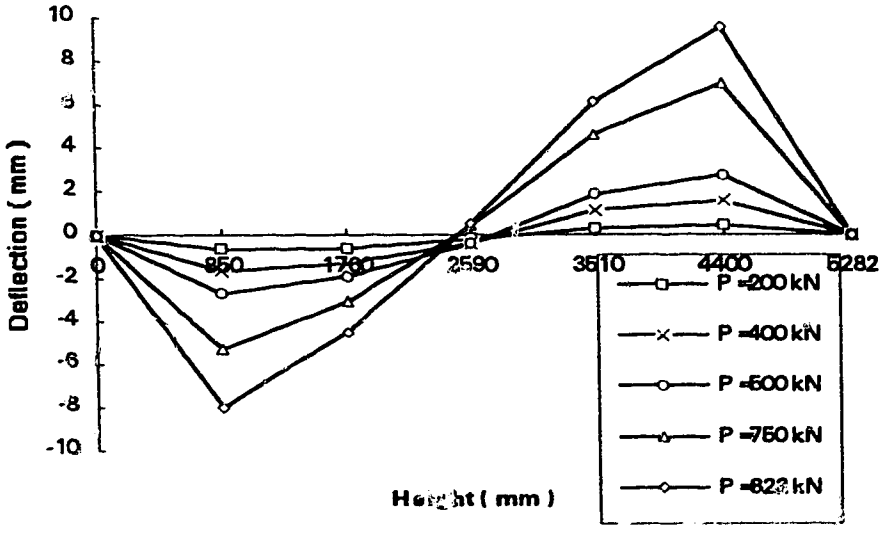

Figure 3.13 Deflected shape of specimen W9

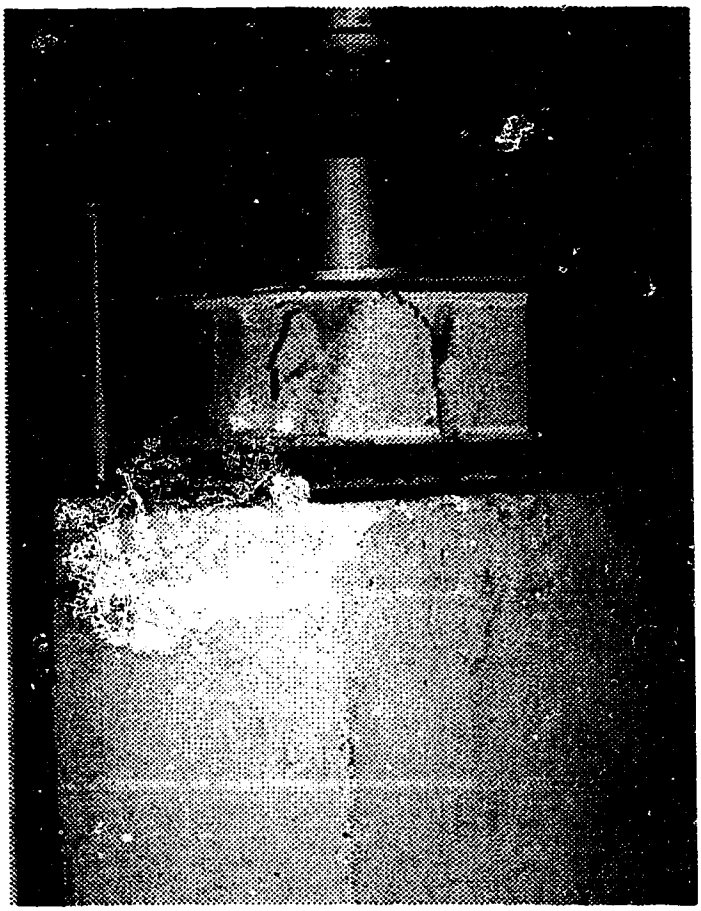

Plate 3.1 Failure of concrete block unit in compression

Plate 3.2 Failure of hollow block prism in compression

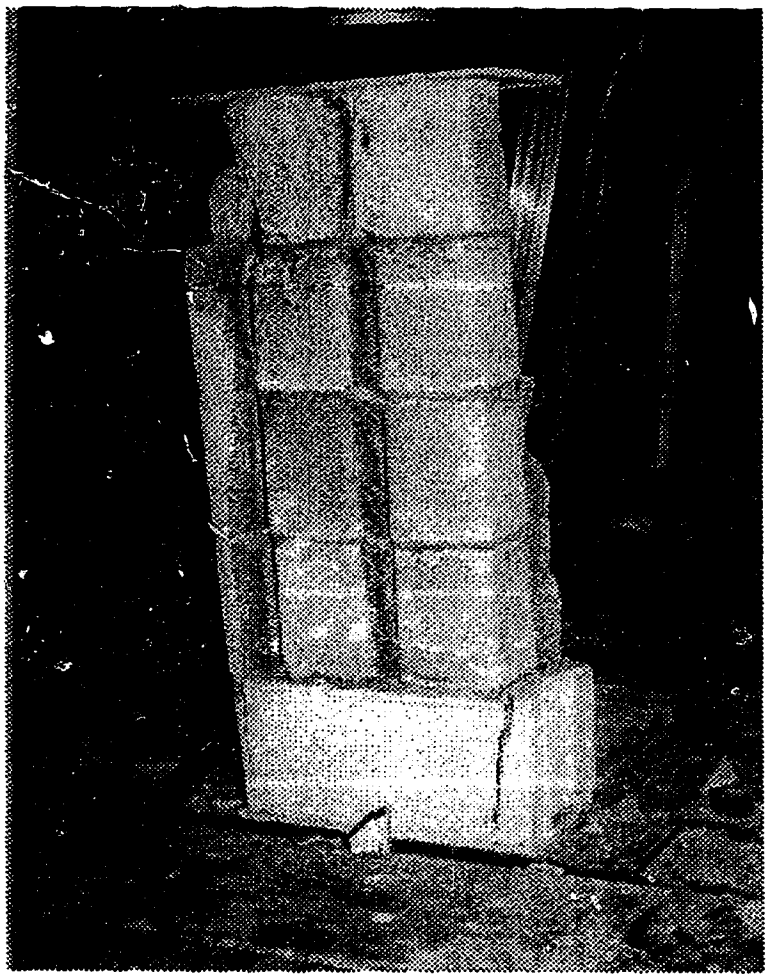

Plate 3.3 Failure of grouted block prism in compression

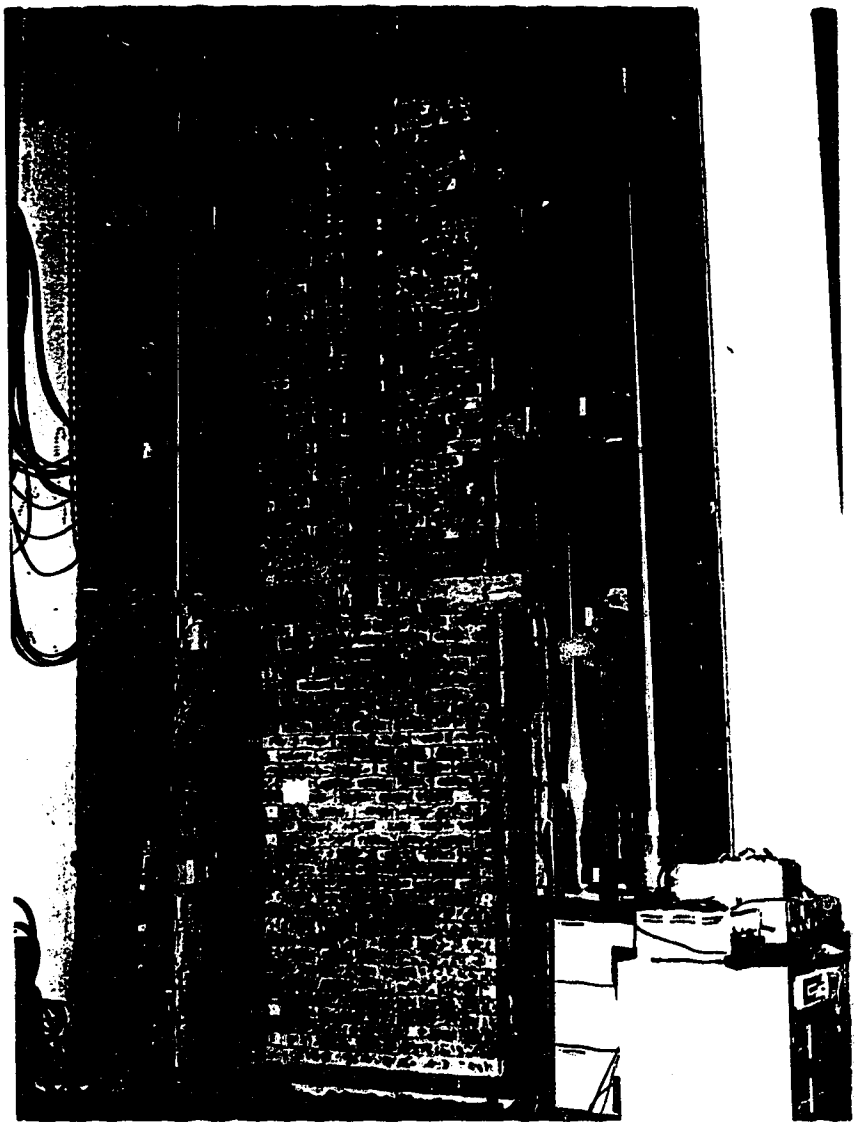

Plate 3.4 MTS loading frame

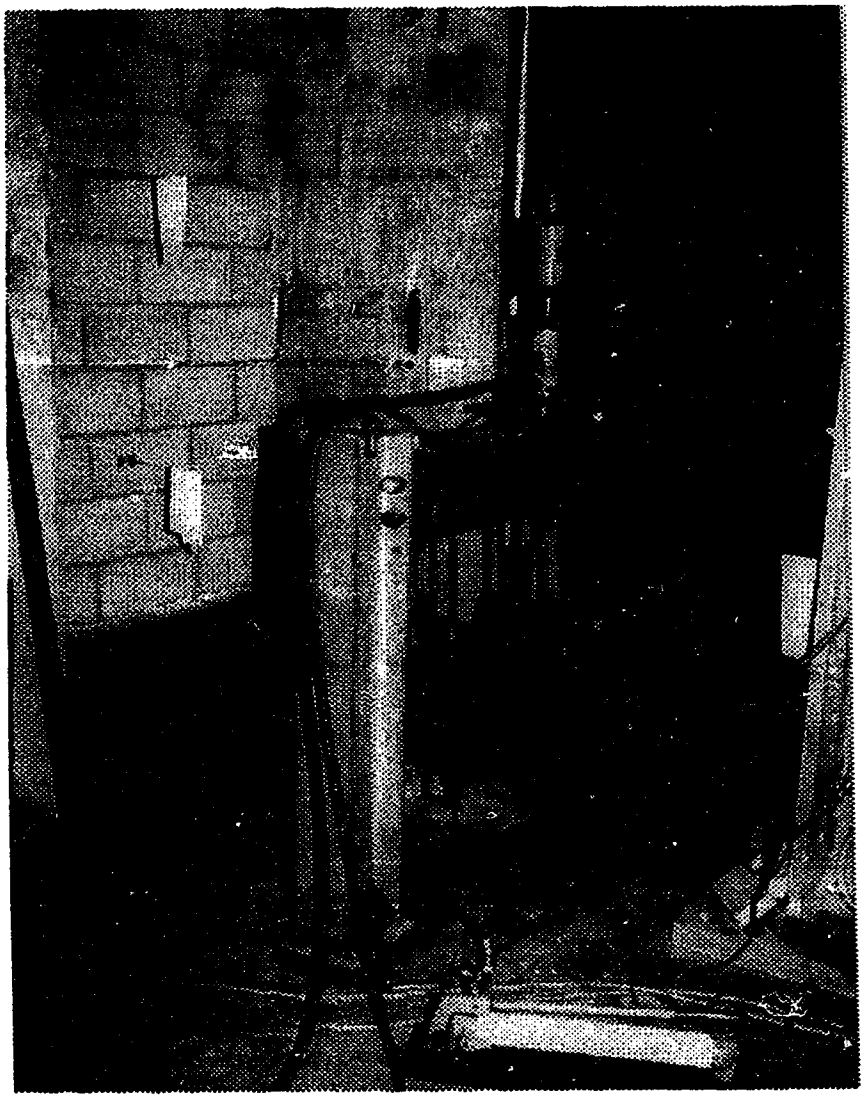

Plate 3.5 Loading frame for hydraulic ram

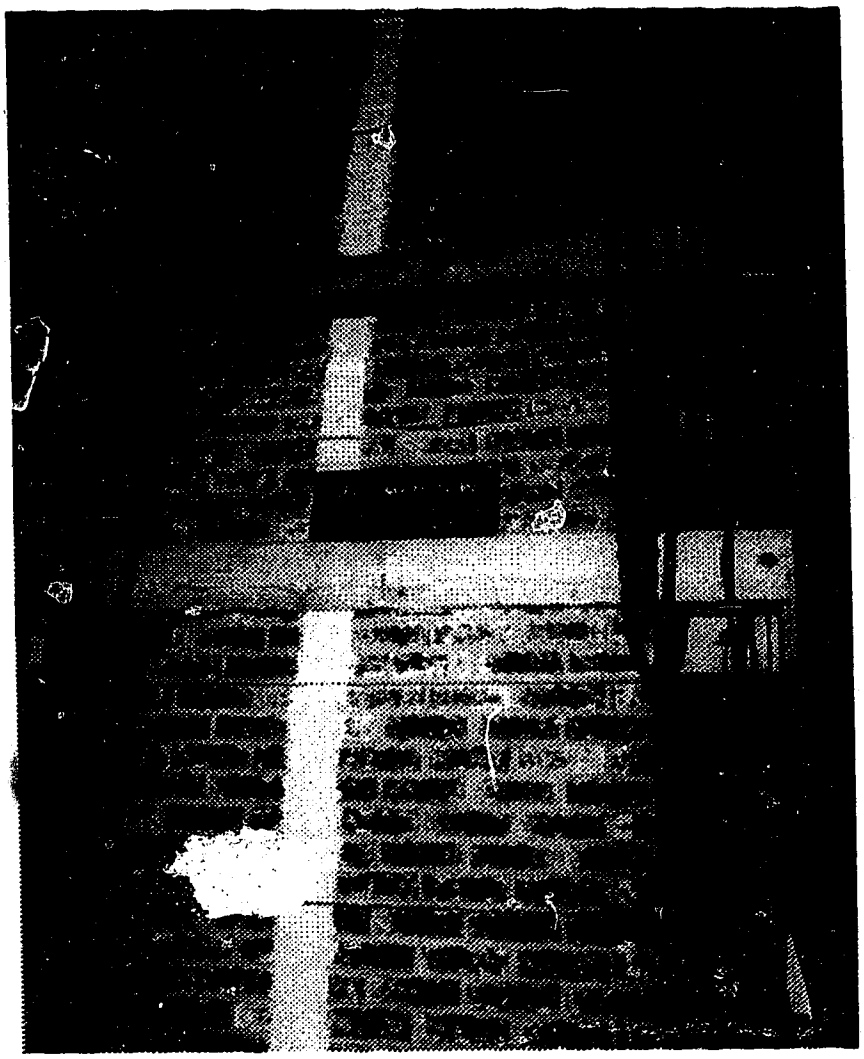

Plate 3.6 Cracks in the wall

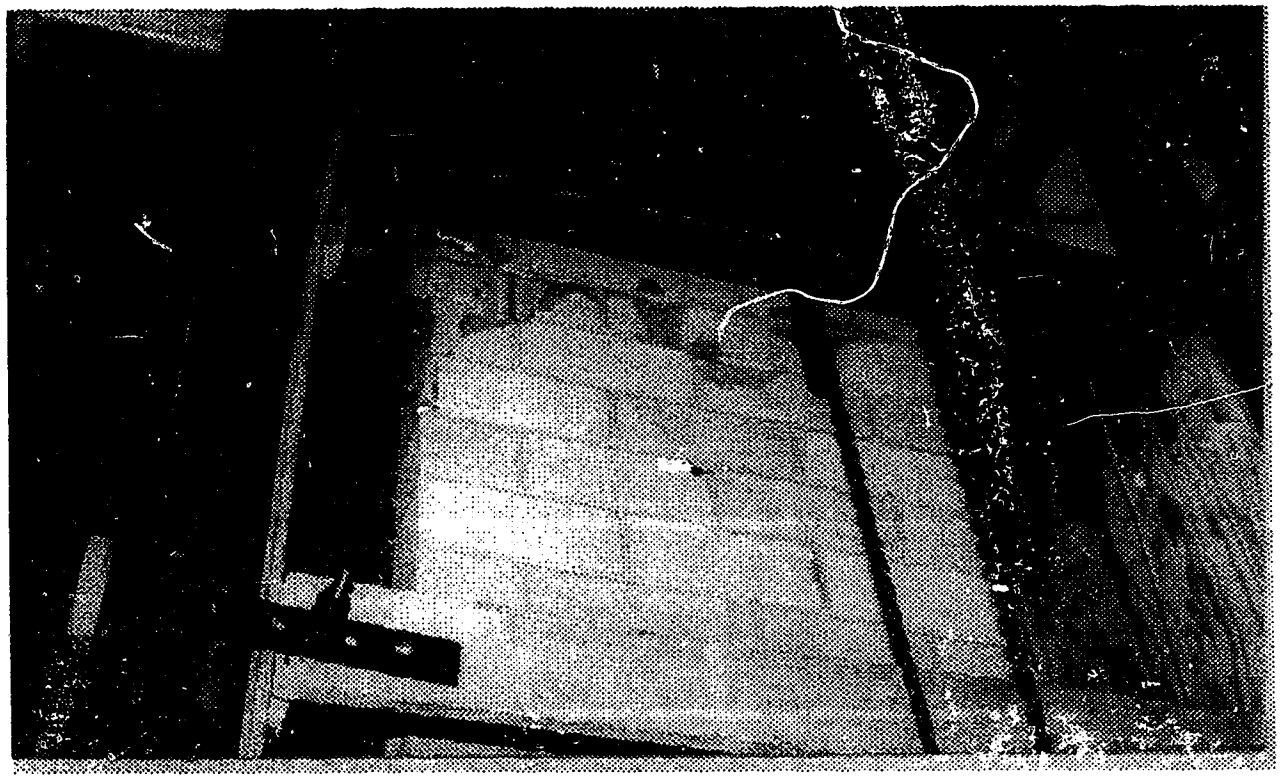

Plate 3.7 Failure of specimen W4

Plate 3.8 Debonding cracks extended into units

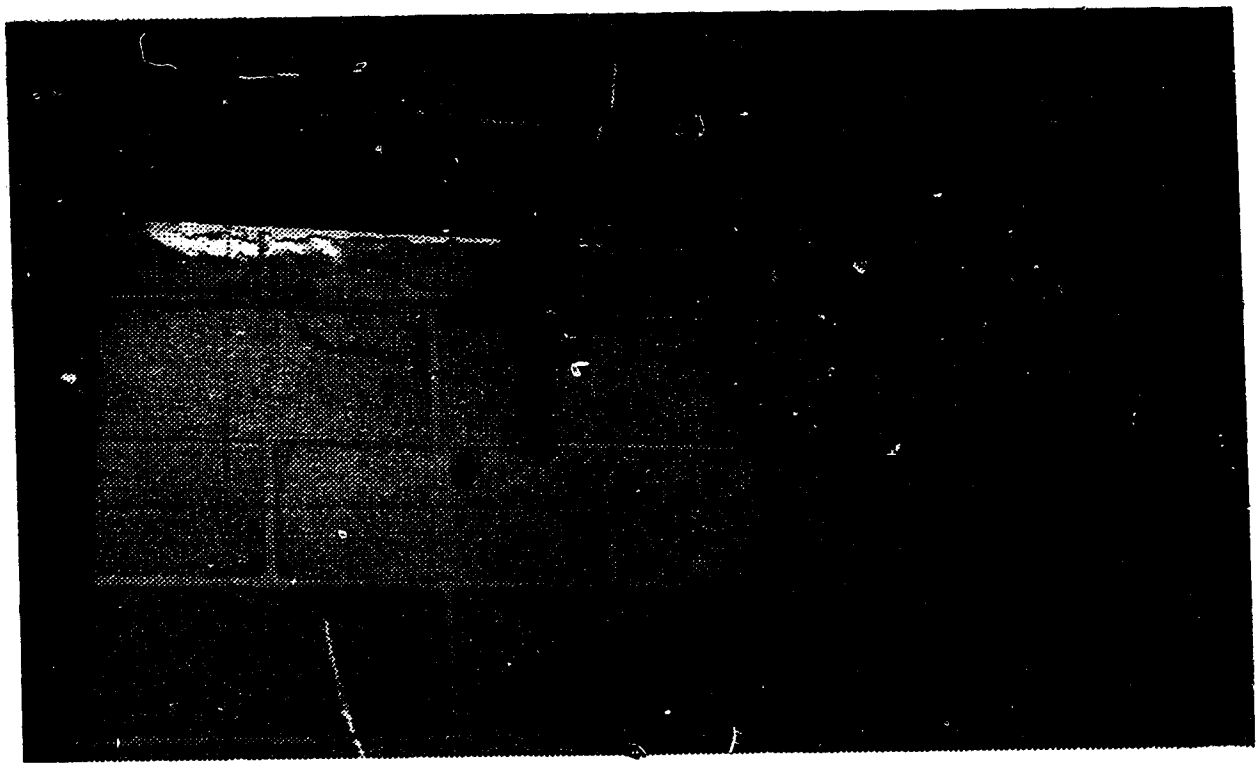

Plate 3.9 Failure of specimen W9

CHAPTER FOUR

NUMERICAL SIMULATION

4.1 Introduction

To fully understand the behaviour of the masonry cavity walls, a large number of vall tests are required in order to incorporate a wide range of performing parameters that affect wall behaviour. However, such a fully experimentally based investigation is too expensive and time consuming to be feasible in practice. A small number of full scale tests is critical, however, to provide reliable information for assessing the behaviour of the wall. In this work, the experimental database obtained at the University of Alberta consists of four plain cavity walls and three reinforced cavity walls tested by Goyal et al.(1993) and the nine reinforced cavity walls tested in the course of this study.

In order to extend the database a numerical analysis model can be used to investigate the full range of parameters not covered by the tests. The performance of this model must, first, be verified against the test results in order to develop confidence in the results and to develop an insight into the mode of failure. This chapter presents a simple and efficient nonlinear finite element model developed to complement the experimental work. The model was implemented in the general purpose finite element program ABAQUS(Hibbitt et al. 1994). The model accounts for both material and geometrical nonlinearity aspects of the tests which will be discussed in subsequent sections. In order to verify the accuracy of the simulation, a comparison between the test results and the results by finite element simulation, specifically the load-deflection response curves and critical loads P_u, will be stressed in section 4.4. It was, then, used to extend the database of tests to a wider range of variables. This will be the subject of the next chapter.

4.2 Numerical Model

4.2.1 Finite Element Mesh

4.2.1.1 Beam Element Model

Masonry walls subjected to combined axial load and out-of-plane bending moment are usually designed to span vertically. Such walls work essentially as columns with uniformly distributed deflection along the width of the wall. If, however, side supports are provided, which are usually designed to resist horizontal forces and to reduce slenderness effects, the wall can also span horizontally forming curvatures in two directions. Since the scope of this research is focused on vertically loaded walls, only vertical span walls were considered as were the cases in the experimental program. No side supports nor their beneficial effect on the deflection of the wall have been considered. Since Poisson's ratio properties in masonry walls are not clear, plain strain response was neglected, and plane stress conditions were assumed. These walls could be modeled as a two dimensional continuum or as a beam assembly. The model presented herein is a beam model with the different components modeled along their centrelines.

Two reasons were considered when selecting a beam element model instead of a two-dimensional plane stress element model. First, the beam element model is simpler with fewer nodes and is more suitable to model large dimensional structures. Second, we are more interested in the overall behaviour - the stiffness and strength for instance-of the masonry walls under consideration, rather than in the local distribution of the stresses.

There are several types of beam elements available in ABAQUS. The 3-node quadratic beam type element, B22, was selected for masonry assemblages. This type of element uses Timoshenko beam theory (Timoshenko, 1972) which takes into account the transverse shear deformation of the cross-section. Hence, the deformed cross-section may not remain normal to the beam axis. Such an assumption is consistent with the case of

masonry assemblages under out-of-plane bending where the transverse shear deformation is significant (Essawy, et al. 1985). Unlike the response to axial and flexural loads, the transverse shear deformation is treated in ABAQUS as a linear elastic response.

To model the shear connectors, a special type of element- 3-node quadratic beam elements with hybrid formulation B22H was used. This is because the shear connector is a very short element. It exhibits very large stiffness about the axis of bending. It was found from analysis that a beneficial effect is achieved by using hybrid elements which treat the axial and transverse shear forces as independent degrees of freedom. The shear connectors were modeled with an elastic perfectly plastic von Mises material model.

4.2.1.2 Element Mesh

Masonry is a composite material. In an assemblage of masonry, individual materials interact with each other rendering the behaviour of the assemblage difficult to predict by using the material properties of each individual component. As a consequence, when finite element analysis is introduced into masonry structures, a common argument arises on whether a macroscopic or a microscopic analytical model should be chosen. Microscopic models usually consider the existence of mortar joints as layers of weakness by separately modeling mortar joints and units (Arya and Hegemier, 1982, Page, 1978, Balachandran 1974). A microscopic model has been developed and tried in this research project initially. That model separately considered each mortar joint and each unit. There was no interface element between the mortar joint and unit. The mortar tension failure mode was based on the debonding limiting stresses between mortar and unit. It was found that analytical results based on this model were not satisfactory. In the author's opinion, this model was unable to simulate the crack propagation between elements after debonding. The discontinuity of deformation between a debonded mortar element and a unit element caused numerical solution problems. Some improvement to this model may be achieved by adding interface elements between joints and units(Lotfi, et al. 1994). However, adding interface elements is not practical since it would make the number of

elements which is already quite large, even larger with no guarantee that satisfactory results could be obtained.

For the above reasons, a macroscopic model was finally chosen. In this model, the wall is discretised into finite elements with no particular attention given to the position of mortar layers. Debonding would most probably occur within an element which could be modeled as a crack and allowed to propagate as a crack. Properties of the masonry assemblage as a whole, that is, the properties of masonry prisms, could thus be used instead of the different properties of each individual material component. The weakness of mortar layer in tension was considered by using the bond strengths as tensile strengths between concrete masonry units and mortar joints as well as between brick units and mortar joints respectively. Detailed material properties will be discussed in the next section.

Figure 4.1 shows the proposed finite element mesh. The concrete masonry wythe is simply supported with a hinge at the bottom and a roller at the top. A relatively stiff element was used to model the steel angle at the bottom of the brick masonry wythe. One end of this element is fixed to the bottom of the concrete masonry wythe and the other end is connected to the brick masonry wythe by a two-node constraint equation. The two nodes are overlapped at one point by a constraint equation which allows horizontal movement while constraining the vertical movement between the steel angle element and brick masonry wythe to be equal. Hinges were used to model the connection between shear connector plates and V-ties while fixed end conditions were used to model the joints between connector plates and concrete masonry elements as well as between the V-ties and brick masonry elements.

To account for the effects of embedment, the stiffness and the cross-sectional area of shear connector plates and V-ties embedded within the masonry wythes were modeled with values higher than those of the connectors or V-ties themselves. The ratios of properties between embedded and outstanding parts were one hundred for moment of

inertia and ten for cross-sectional area. A larger ratio was selected for the bending stiffness because embedment contributes more to the stiffness than to the cross-sectional area of shear connectors. The selection of those ratios was semi-empirical since little information was available from previous research. Papanikolas et al. (1990) assumed infinitely large stiffness and cross-sectional area for the embedded part of connectors in their analytical model of these walls. A preliminary analysis conducted during the work reported herein indicated that the increment in the stiffness and cross-sectional area for embedded parts has little effect on the behaviour of the whole connector if those values were increased beyond the suggested range.

4.2.2 Material and Parameters

4.2.2.1 Properties of Masonry Assemblage and Reinforcement

In the elastic range, the masonry assemblage was modeled as an isotropic elastic material. Young's modulus of both the concrete masonry and brick masonry were based on the average prism test values reported in Chapter 3. These Young's moduli and Poisson's ratios are listed in table 4.1 (a) and (b).

Beyond the elastic range, the material option *CONCRETE in ABAQUS was used to model masonry assemblages. This option provides a smeared crack propagation simulation. The cracking failure criterion is defined by a "crack detection surface" which is a function of the principal stresses. Once the stress state reaches this surface cracking is initiated. The presence of cracks will be reflected in the constitutive calculation at related integration points. That is, the stress and material stiffness at that integration point will be changed. Since at each integration point, different constitutive values may be used, the crack propagation from point to point can be simulated.

In order to use this material model, several material properties have to be defined. For the uniaxial compressive stress-strain relationship, a simplified curve with several

straight line segments was selected in which the ascending part was defined by prism test results and the descending part was obtained according to the proposed curve by Atkinson and Yan (1990). This simplified curve was used both for concrete masonry and for brick masonry with different control parameters, f'_m, which were obtained from tests.

For masonry in tension, as mentioned above, the bond strength between the units and mortar layer were used as tensile strengths since in most cases masonry experiences tensile failure by debonding of mortar and units. This bond strength is often referred to as the flexural tensile strength of masonry. The tensile strength values as defined above are listed in table 4.1(a) and 4.1 (b) where ratios of these tensile strengths to the corresponding compressive strengths are also listed as required by ABAQUS.

Another category of parameters defines the phenomenon of tension stiffening which reflects the postcracking behaviour between the cracks. Unfortunately, there is no such information for masonry to date. A reasonable way of estimating the tension stiffening effect in reinforced masonry structure is to compare it with reinforced concrete structure. In reinforced concrete structures, the tension stiffening effect is a function of the reinforcement ratio, the bond strength between rebar and concrete, as well as the finite element mesh. In reinforced masonry structures, beside those mentioned above, the grout fill, in author's opinion, has a significant effect on tension stiffening behaviour. This is because the grout fill bonded with the rebar is a continuous member from top to bottom of the wall. Moreover, the tensile strength of grout material is much higher, usually more than five times that of the bond strength of masonry. Thus, once the debonding occurs between a unit and a mortar joint, the grout fill together with rebar will act as a stiffener to resist the propagation of debonding. Therefore, the complete debonding of that joint is delayed. This effect needs to be quantified in future research. At present, the tension stiffening is modeled here with the descending part of the stress strain curve in tension. The total strain corresponding to the stress ranging from failure to zero was selected as 4.3×10^{-3}. Figure 4.2 shows the complete stress-strain curve used in this analysis including the part of tension stiffening.

4.2.2.2 Properties of Shear Connectors

In Chapter 2, an equivalent stiffness EI has been derived which converts the perforated connector plate into a plate with a solid cross-section. These values of EI were used to model the connector behaviour. The modulus of elasticity, E , of the connector plate was selected as 200 GPa. The cross-section of the connector plate was sized so that the products of moment inertia of the cross-section and the modulus of elasticity equaled the EI value derived from Chapter 2. The equivalent cross-sectional areas of the shear connectors were defined according to the load-displacement response of the shear connector tests. A value of yield strength of the connectors was defined as a nominal strength such that the capacities of the connectors based on the equivalent cross-section approach to the capacity of the connector under a combined load condition. These values are listed in table 4.1 (b).

4.2.3 Analysis Procedure

4.2.3.1 Nonlinear Solution Methods

In ABAQUS nonlinear incremental static analysis is controlled using the Newton-Raphson iteration method. However, Newton's technique is ineffective when the load-displacement curve undergoes an unstable response as shown in Fig. 4.5, where, the negative stiffness of the curve indicates buckling or collapse. ABAQUS provides another solution technique to deal with such cases - the modified Riks algorithm (Ramm 1981, Riks 1979). The principal idea of this method is to treat the load magnitude as a variable such that the equilibrium solutions are obtained by controlling the iteration path along the load-displacement curve. Fig. 4.3 shows a schematic of the modified Riks algorithm.

The solution is obtained by " moving a given distance along the tangent line to the current solution point, and then searching for equilibrium in the plane that passes through

the point thus obtained and is orthogonal to the same tangent line".(ABAQUS User's Manual, 1992).

The loading procedure was carried out incrementally in several stages using a load control solution strategy with a standard Newton-Raphson iterative procedure. Before reaching the ultimate load point, the solution strategy switched to a modified Riks algorithm to obtain ultimate load P_u and to proceed into the postbuckling load-displacement response. The increment sizes within each step were kept small because there is a finite radius of convergence for Newton's method. If the increment is too large, divergence is indicated by the program and no solution could be obtained.

4.2.3.2 Removal of the Element

Another aspect of the analysis is the treatment of the buckling behaviour of the shear connectors. Once a connector is buckled, the load on that connector will be redistributed among other connectors. This phenomenon was modeled with ABAQUS's option *MODEL CHANGE in which an element that is no longer effective is removed. It was assumed that successive failure would occur in a layer of connectors if one of them buckled first. Thus, the removal of a connector element means that the whole layer of the connectors, which usually contains two or three connectors, is removed.

4.3 Simulation of Test Results

All tests reported here were conducted on walls made with 200 mm blocks with a variety of end conditions and eccentricities. The eccentricities referred to here are measured from the centroidal axis of the block wythe. Table 4.2 summarizes the parameters of the test specimens, as well as the results of both test and analysis.

4.3.1 Group 1, Loading with $e_1 / e_2 = 1$

This group consists of specimens W1, W6, W7 and W8. Specimens W1 and W8 both had 75 mm cavities, were both loaded with eccentricities away from the brick wythe but W1 had e = t/3 while W8 had e = t/2. Specimens W6 and W7 were loaded towards the brick wythe but the first had a 75 mm cavity and eccentricity of t/2 while the second had a 100 mm cavity and a t/3 eccentricity.

Figure 4.4 shows the mid-height load-displacement responses of specimen W1 obtained from the analysis and test. It can be observed that the model performance is satisfactory since it reproduces most characteristics of the test curve. Specifically, the ultimate load P_u from analysis is consistent with that obtained in the test and the deformation of the wall obtained from analysis has good agreement with that obtained from the test even into the post-cracking range and post-ultimate range.

Figure 4.5 shows the results for specimen W7. The model performance here is also satisfactory. The deformation response from the numerical analysis is fairly consistent with that of the test result up to a load level of $P = 0.9\ P_u$.

For specimen W6, the results are shown in Fig. 4.6. It can be observed that the numerical analysis presents a load-deflection response pattern and failure mode similar to those of the test even though some difference exists between the two curves. The ultimate load P_u predicted by the analysis is below the value measured from the test by 5.9 %. It seems that the simulation curve overestimates the cracking strength and underestimates the post-cracking capacity. Those differences may result from a number of reasons. The variation in the properties of masonry materials is high, especially the variation in the bond strength between masonry units and mortar joints. Since specimen W6 was subjected to a load with large eccentricity, 90 mm, the cross-section of the wall was subjected to a strain gradient. Such a strain gradient may affect the tension stiffening behaviour. That

effect was considered constant in the analysis. Considering the two conditions, the small discrepancy between the analysis and test is understandable and acceptable.

Figure 4.7 shows the numerical and experimental responses of specimen W8. Both the ultimate load and the deflection history have been well predicted by the analysis. It was found in the analysis that the shear connectors at the top of the specimen reached their ultimate load capacity and buckled. Those connectors were removed from the wall for the subsequent load steps using the procedure described earlier. This failure mode will be discussed further in section 4.4.

4.3.2 Group 2, Loading with $e_1 / e_2 = 0$

This group consists of two specimens W2 and W3. Both had 75 mm cavities and were loaded with an eccentricity of e = t/ 3 at the top of the wall and zero at the bottom. Specimen W2 was loaded away from the brick wythe while specimen W3 was loaded towards the brick wythe. Figure 4.8 and 4.9 show the numerical analysis and the test responses for specimen W2 and W3.

For specimen W2, the analysis overestimates the ultimate load capacity by fifteen percent. Again, the variation in the material properties and in the estimation of post-cracking strength may explain the discrepancy in the response.

For specimen W3, as mentioned in Chapter 3, a lower load capacity was observed in the test than expected. Therefore, two sets of material properties were used to obtain two parallel numerical responses . In one set, average material properties obtained from prism tests were used as were the cases of other specimens. It was found that the analysis result corresponding to this set of material properties overestimates the ultimate load capacity P_u by 40 %. In the other set, a lower compression strengths $f'_m \approx 0.7\ f'_{m\ average}$ was selected both for concrete block masonry and for brick masonry. The value 0.7 was chosen to account for possible variation in the prism test results. The corresponding

tensile strengths were also changed proportionally. The numerical response based on this set of material properties agrees well with the test curve on the initial part of deflection and on ultimate load capacity as shown in Fig. 4.9. The values of P_u from both sets of analytical results are listed in Table 4.2.

4.3.3 Group 3, Loading with $e_1 / e_2 = -1$

This group consists of specimens W4 and W9. Both had 75 mm cavities and were both loaded with opposite eccentricities at the two ends of each specimen causing the walls to deflect in double curvature. The loading eccentricities for specimens W4 and W9 were t/3 and t/2 respectively.

Since both the initial conditions and the unwinding phenomena have effects on the deflected shape of specimens with double curvature, relative displacement between upper and lower curves is plotted instead of deflection at one point.

Figure 4.10 shows the relative displacement between nodes at elevations of 0.85m and 4.4m from the bottom of specimen W4 obtained from the analysis and the test. In the analysis, the loading steps were designed to follow the loading procedure of the test exactly. That is, the moment at the bottom of the wall remained unchanged after loading beyond 800 kN. The P_u obtained from analysis is fairly consistent with that from the test. In the test, the failure started from the outer face-shell of the top block of concrete masonry wythe where the top concrete block masonry reached its prism compression strength. The failure mode and the locations of failure detected by the analysis were the same as those observed in the test.

Figure 4.11 shows the test and analysis results of specimen W9. The curves obtained in the test and analysis are fairly close. The predicted ultimate load capacity is 10% less than the measured value in the test. Again, the failure mode was similar to that of the test - a material compression failure mode.

4.4 Failure Modes

A study of the failure patterns was conducted based on the numerical analysis and the test results. For the specimens under investigation, failure can be categorized into three groups: inelastic instability failure of the whole cavity wall due to large deformations, material failure, and buckling of the shear connectors.

- Buckling of the whole wall

When loading with single curvature and equal eccentricities at the two ends of the specimen, failure, in most instances, was by buckling or inelastic instability of the whole cavity wall. Specimens that experienced that failure type underwent a nonlinear deflection stage up to the ultimate load followed by a softening part in which the load reduced and the deflection increased rapidly. Such nonlinearity was due to the nonlinear constitutive relationships of the materials and the slenderness effect. In most cases, the post-buckling strength of the specimen could be traced using a stroke control technique in the test or Riks solution method in the analysis.

For specimens loaded with eccentricity only at one end, the failure mode was also inelastic instability failure of the whole specimen. Since the maximum moment was at one end of the wall, the slenderness effect might not be as obvious as in the first case where eccentric loads were added at both ends of specimens.

- Material failure

The material failure mode occurred under a double curvature loading condition. Since the maximum moment occurred at the two ends of the specimen, the slenderness effect was not significant. The failure was brittle with a sudden spalling of the face-shell at the top masonry block course. No post failure part of the response was obtained from the test nor from the analysis. It was detected from the analysis that at the failure zone, the

concrete blocks reached the compression strength obtained from the concrete masonry prism tests.

- Buckling of the shear connector

In the analysis of specimen W8, it was found that some shear connectors reached their ultimate load capacity and buckled. The buckling started at the first layer of connectors from the top of the wall at a load level of 120 kN. More connectors (the second layer from the top and the first layer from the bottom) buckled as the load increased until the whole specimen reached the ultimate load. During the test, although no buckling of the shear connectors was captured due to the difficulty of observation, it was observed that several big cracks formed in the brick wythe causing the wythe to separate into several rigid parts before reaching the ultimate load. Summarizing the observation from the test as well as from the analysis, it is believed that for the wall with designed shear connector pattern and large eccentricity (e = t/2), buckling of the shear connectors accompanied with through cracking of the brick wythe resulted in plastic hinges forming at the locations of cracks in the brick wythe. The brick wythe stopped resisting additional moment after the formation of the plastic hinges causing the redistribution of the moment among the two wythes of the cavity wall. Because of the existence of reinforcement in the block wythe, the wall could sustain significant load even after reaching the ultimate load.

4.5 Summary

Above all, it can be concluded that the numerical simulation of masonry cavity wall tests is quite satisfactory. The model reproduces most characteristics of the load-deflection curves of the test results. Table 4.2 summarizes the analytical results for P_u and their comparison to the test results. The mean of the ratio of $P_{u\ analytical} / P_{u\ test}$ is 1.0170 (or 1.0602 considering average material property for specimen W3). The standard deviation is 0.0835 (or 0.1527 considering average material property for specimen W3).

Table 4.1(a) Properties of Masonry

	Material Properties (a)	Value Used (b)	(b)/ f'_m
Concrete Block	Modulus of Elasticity	13920 MPa	721.2
	Poisson's Ratio	0.2	N / A
	Compression Strength	19.3 MPa	N / A
	Tensile (Bond) Strength	0.56 MPa	0.029
Brick Veneer	Modulus of Elasticity	6536 MPa	361.0
	Poisson's Ratio	0.2	N / A
	Compression Strength	18.1 MPa	N / A
	Tensile (Bond) Strength	0.63 MPa	0.035

Table 4.1(b) Properties of Shear Connectors

Material Properties	75 mm Connectors	100 mm Connectors
Modulus of Elasticity	200 MPa	200 MPa
Nominal Strength F_y	300MPa	300 MPa
Area (one connector)	2.95 mm^2	1.82 mm^2
Moment of Inertia (one connector)	14030 mm^4	9550 mm^4

Table 4.2 Comparison of Analysis to Test

Specimen	C*	e_1/e_2	e**	a *** or t	Slenderness	P_u Analysis	P_u Test	Analysis / Test
	mm					kN	kN	
w1	75	1	t / 3	a	27.8	447.8	451.0	0.993
w2	75	0	t / 3	a	27.8	938.0	818.5	1.146
w3	75	0	t / 3	t	27.8	662.0 913.6	651.9	1.015 1.401
w4	75	-1	t / 3	N/A	27.8	1198.0	1200.1	0.998
w5	75	0	t / 3	a	27.8	938.0	815.5	1.150
w6	75	1	t / 2	t	27.8	236.4	251.4	0.940
w7	100	1	t / 3	t	27.8	424.4	424.0	1.001
w8	75	1	t / 2	a	27.8	168.7	166.0	1.016
w9	75	-1	t / 2	N/A	27.8	738.0	822.9	0.897

* C = cavity;
** e = eccentricity
*** a = away from veneer;
t= towards veneer

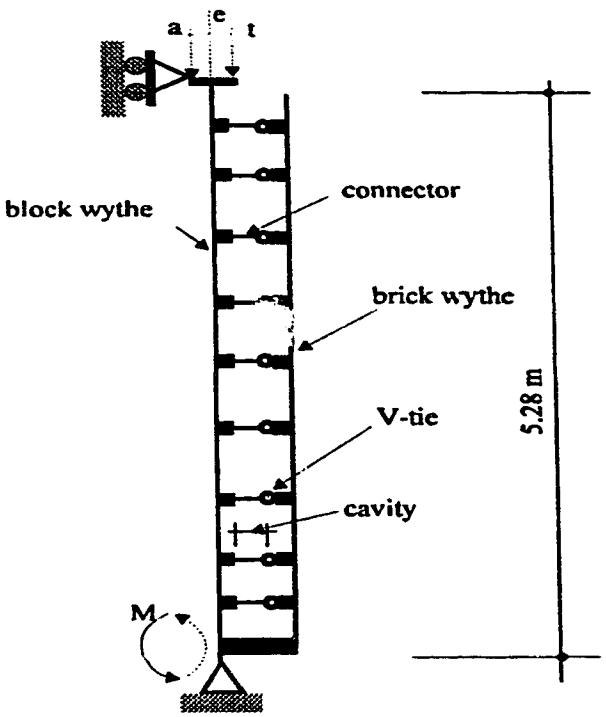

Figure 4.1 Finite element mesh

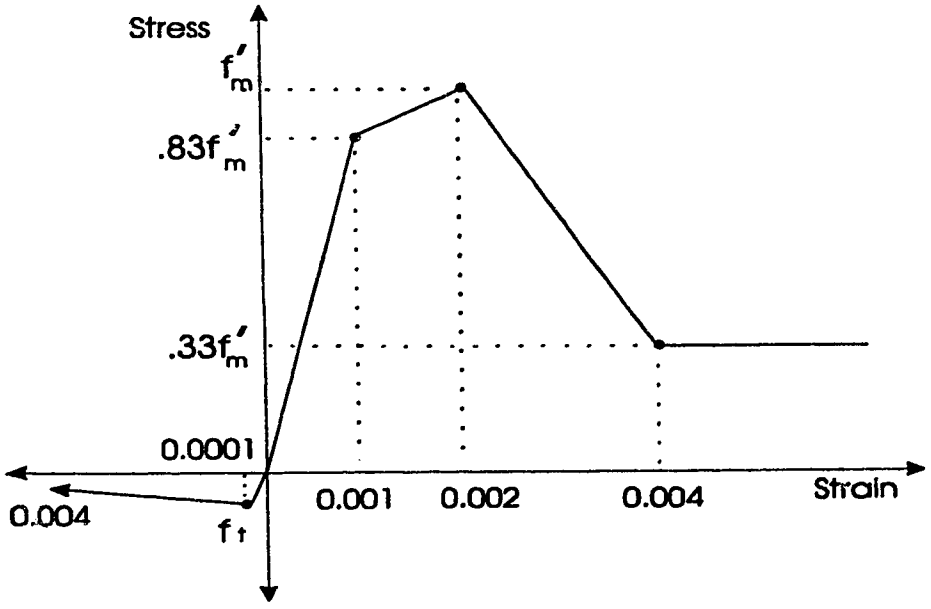

Figure 4.2 Stress-strain curve for masonry

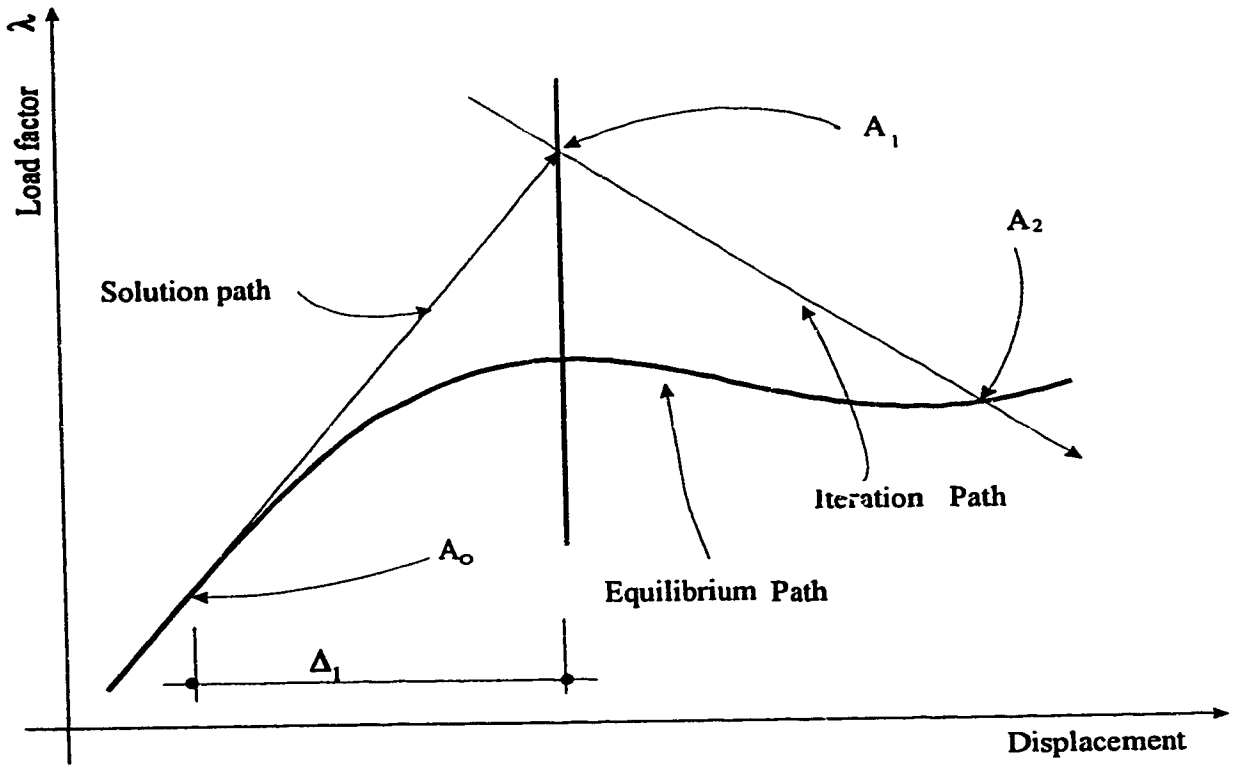

A_o — Initial solution point

A_1 — Solution point after moving Δl along solution path

A_2 — Solution point in the plane passing through A_1 and orthogonal to the first solution path

Figure 4.3 Schematic of Modified Riks Algorithm

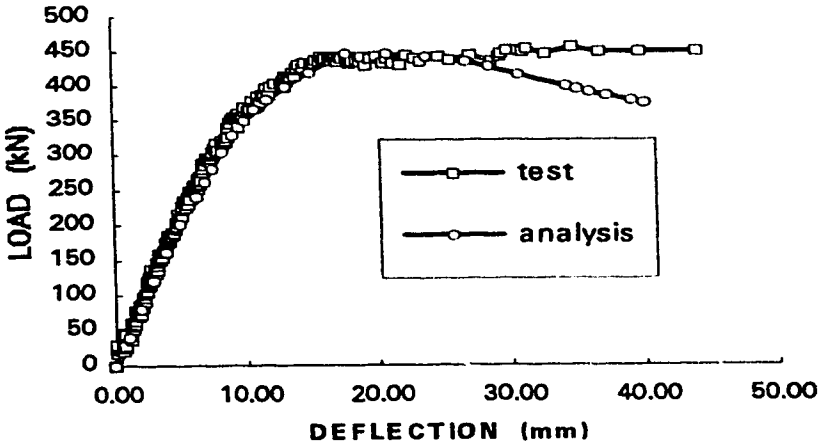

Figure 4.4 Mid-height deflection of specimen W1

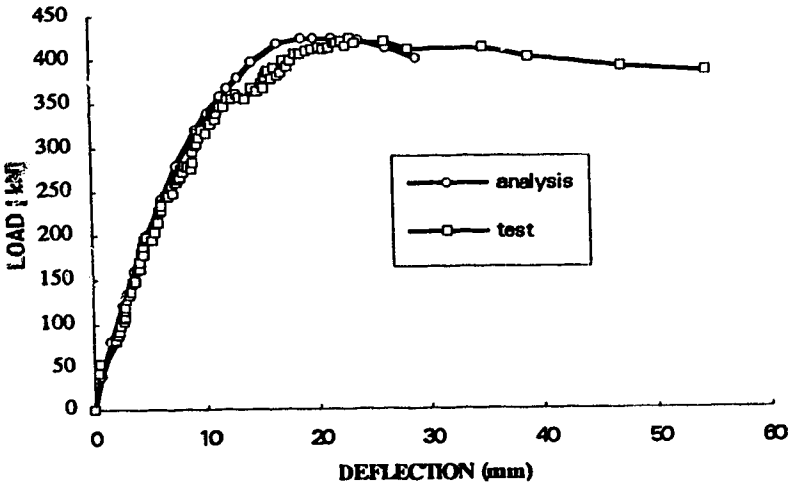

Figure 4.5 Mid-height deflection of specimen W7

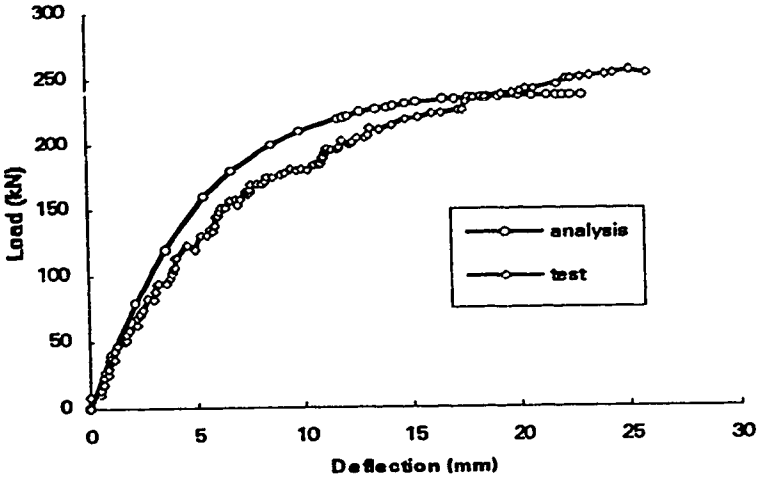

Figure 4.6 Mid-height deflection of specimen W6

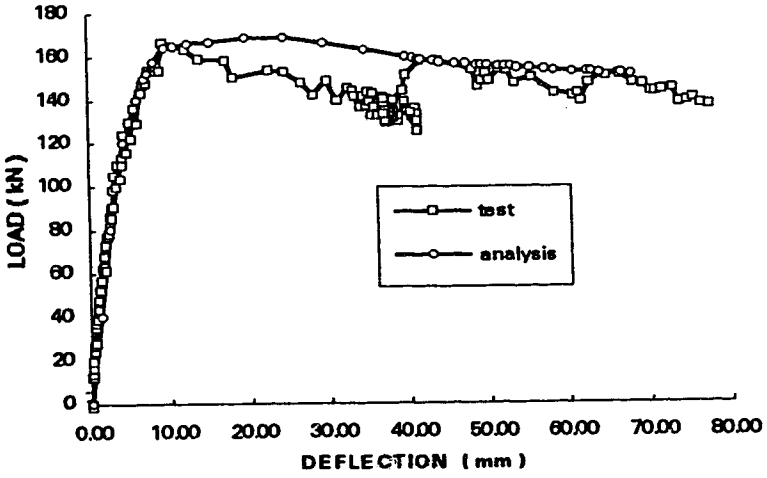

Figure 4.7 Mid-height deflection of specimen W8

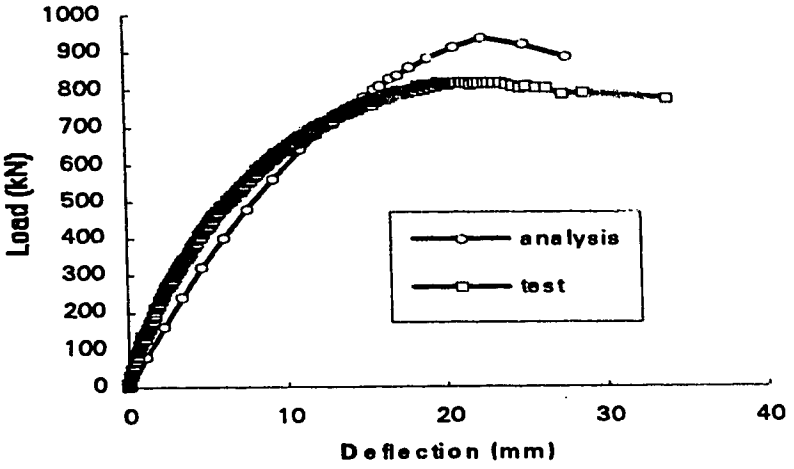

Figure 4.8 Mid-height deflection of specimen W2

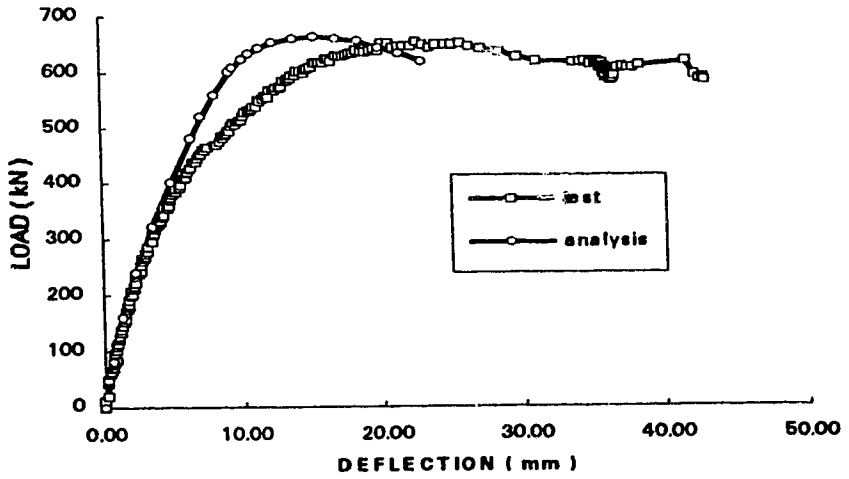

Figure 4.9 Mid-height deflection of specimen W3

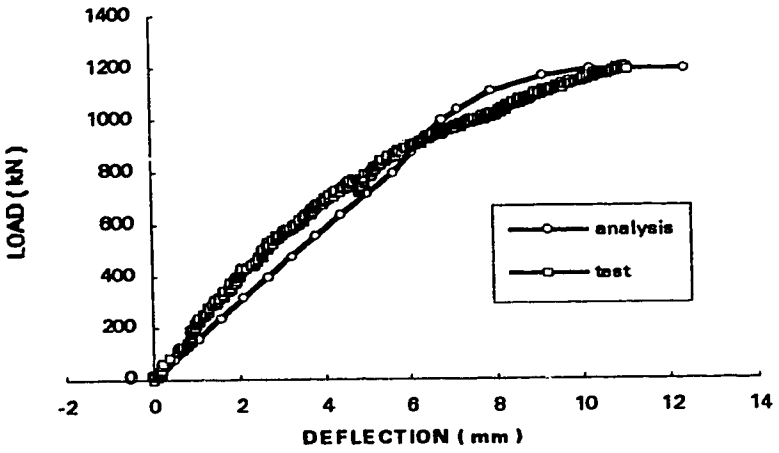

Figure 4.10 Relative displacement between height = 0.88 m and height = 4.4 m of specimen W4

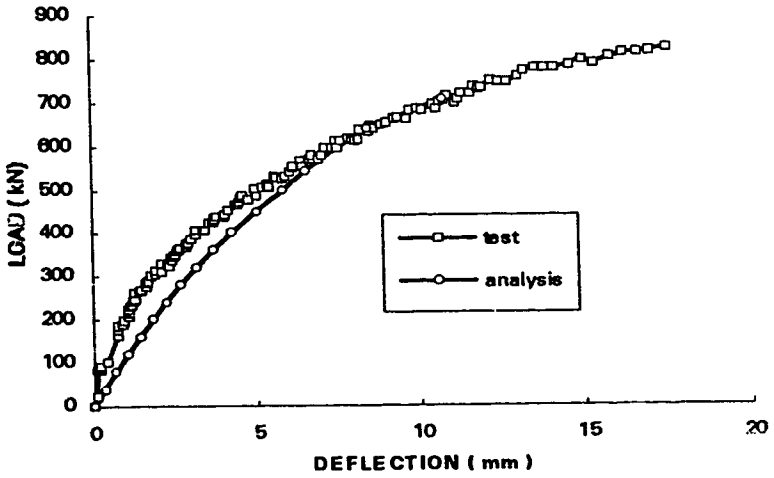

Figure 4.11 Relative displacement between height = 0.88 m and height = 4.4 m of specimen W9

CHAPTER FIVE

PARAMETRIC STUDY

5.1 Introduction

The database established by the experimental program was confined to a limited number and range of variables. In fact, many other parameters affect the ultimate load carrying capacity and the stiffness of the cavity walls. Using the finite element analysis model described in Chapter Four, an extensive parametric study was carried out to investigate the effects of these parameters. The investigation started with studying and selecting the potential variables and their range. Ninety-one hypothetical reinforced masonry cavity walls were, then, analyzed. This numerical analysis, or computer test, enlarged extensively the experimental database. It furnished sufficient information for a regression analysis which will be discussed in the next chapter. The analysis also provided a way of exploring the interrelationship between parameters. This chapter presents the selection of the variables and parametric study along with the analysis results. More results will be discussed in the next chapter.

5.2 The Variables

A cursory look at the problem suggests that a large set of parameters could have effects on the behaviour of shear connected cavity walls. These parameters are the loading conditions as well as the geometric and material properties of the walls. Rationally, these parameters are the potential predictor variables in estimating the ultimate load-bearing capacity and the effective stiffness of the cavity walls.

A parametric study could be based on a number of basic variables such as: the slenderness ratio L/t ; the eccentricity of the loading e ; the ratio between the eccentricities at the top and the lower ends of the wall e_1/e_2; the material properties of the block wythe such as: the modulus of elasticity E_m, the compressive and tensile strengths; the material properties of the brick wythe; the ratio between the stiffness of the block wythe and the brick wythe $(EI)_{brick}/(EI)_{block}$; the material and geometric properties of the shear connectors, the cavity width and the end conditions. However, not all those parameters were set as variables for several reasons.

First, some parameters have a limited variation in practice such as the physical properties of the shear connectors. For each cavity width, the connectors are manufactured with fixed dimensions hence the variations in geometric properties of the connectors are small. Furthermore, the variations in the material properties of the connectors are relatively small compared to the material properties of masonry. Hence, these parameters were not selected as variables instead they were set with fixed values in the analysis.

Second, there exists certain relationships among some parameters. For example, there is some correlation between the compressive strength and the bond strength of mortar (Neis and Chow, 1980). There is also correlation between the mortar strength and the compressive strength of the block assemblage (Drysdale and Hamid, 1979). Hence, only the compressive strength of the block assemblage which is more reliable and convenient to measure was chosen as a variable. The bond strength was expressed as a fraction of the compressive strength of the block assemblage.

Third, some parameters were difficult to estimate or have relatively small effects on the behaviour of the cavity walls. These parameters were not considered as variables in the analysis. The strength of the brick assemblage of the brick wythe for example, was considered to have less significant effect than that of the block wythe. Hence the compressive and the tensile strengths of the brick assemblage were set as constants.

However, in considering the influence on the behaviour of the cavity walls caused by the brick wythe, a general parameter $(EI)_{brick}/(EI)_{block}$ was selected as a variable to reflect the composite action.

Finally, the evaluation of some parameters such as the end condition of the cavity wall were left to the future research. In this investigation, the model for the end condition of the cavity wall both for the block wythe and the brick wythe followed common practice. The efficiency of this model has been verified by the experimental program and the numerical simulation.

For the above reasons, the parameters selected as primary variables affecting the behaviour of the cavity walls were: the slenderness ratio L/t , the eccentricity of the loading e, the ratio between the eccentricities at the top and the lower ends of the wall e_1/e_2, the modulus of elasticity of the block wythe E_m, the compressive strength of the block assemblage, the ratio between the stiffness of the block wythe and the brick wythe $(EI)_{brick}/(EI)_{block}$, and the cavity width C.

The specimens were analyzed in nine series. The names of the specimens for each series are shown in Table 5.1. The specimens in series 1, 5, 6, 7, and 8 were named WS1 to WS6, WSL1 to WSL6, WSS1 to WSS6, WSM1 to WSM15 and WSM16 to WSM30, respectively. These series were designed with the loading eccentricity, the slenderness ratio and the ratio of e_1/e_2 as the variables. Series 1, 5, and 6 had slenderness ratios of 27.8, 37.3 and 18.3, respectively. Series 1, 7, and 8 had the ratio of e_1/e_2 as 1, 0, and -1 respectively. Series 2 was designed with $(EI)_{brick}/(EI)_{block}$ as the key variable and the specimens were named WSB1 to WSB9. The modulus of elasticity of the block wythe E_m was chosen as the variable for series 3 where the specimens were named as from WSE1 to WSE6. The compressive strength of the block assemblage was the variable for series 4 and the specimens in this series were named as from WSF1 to WSF9. Series 9 was designed with the width of the cavity, the direction of the loading eccentricity and the ratio of $(EI)_{brick}/(EI)_{block}$ as the variables.

In the next few sections, a brief description of the above variables will be given along with discussions and samples of the analysis results.

5.3 The Eccentricity of the Loading

5.3.1 Definitions

The loading eccentricity is defined as the distance from the centroid of the cross-section of the block wythe measured in the direction normal to the surface of the wall. It could be measured either towards the brick wythe; or away from the brick wythe.

Regardless of whether the moment and the axial force are from the same source or not, the loading eccentricity $e = M/P$ could be used to relate the axial load and the bending moment applied at the wall. Hence in the analysis, the term *eccentricity e* refers to the cases where either a vertical eccentric load is applied or a vertical concentric load and a bending moment are applied simultaneously.

5.3.2 Mechanisms of the Wall Behaviour Under Combined Loading

The behaviour of the cavity walls under combined axial load and bending moment is a complex function of the parameters discussed in this chapter. At this stage, it is not the purpose of this section to discuss the mechanism thoroughly. However, since the loading eccentricity is believed to be a key factor affecting the behaviour of the wall and the failure mode, the important aspects of load-carrying mechanisms were considered when selecting the range of the variables and interpreting the analysis results.

The first facet is the interaction between the axial load and the bending moment. Because the wall is in general under a combined loading condition, the axial load-bearing capacity is affected by the applied bending moment. This effect could be represented by interaction diagrams which are functions of the magnitude of the loading eccentricity and

the material properties. Therefore, when selecting the range of eccentricity and other parameters, consideration was given so that a family of interaction diagrams could be constructed according to the variables and their analysis results.

The second facet is that the resistance of masonry walls to the out-of-plane bending moment is much weaker than its resistance to the axial compression. This is because of the anisotropic material properties of masonry. The low bond strength between the mortar joint and the units leads to early wall cracking when loaded with large eccentricity. The cracks cause the stiffness of the wall to drop dramatically. As a consequence, the wall deflects more and the moment increases due to the second order effects. The moment causes the cracks to grow and new cracks to form. The process could continue until the wall fails. Hence, the response of a masonry cavity wall to the different combination of the axial load and the out-of-plane bending moment is very sensitive and fundamental.

The third facet is the efficiency of the shear connector as a load transfer mechanism. The contribution of the brick wythe to the load bearing capacity depends much on how the shear connectors are loaded and how effectively they could transfer the load to the brick wythe. Some previous studies showed that the contribution of the brick wythe to the load bearing capacity increases as the eccentricity increases (Goyal et al. 1993). The analysis results confirmed the same trend as will be shown later.

5.3.3 Strain Gradient

Under combined loading conditions and for large eccentricity, the strain gradient may be significant and rather nonlinear along the thickness of the wall. The actual stress at the extreme fibre may, thus, exceed the compressive strength of the masonry assemblage. For solid masonry, the maximum stress at the extreme fibre at failure could be 1.3 to 1.5 times the strength for concentric loading. For grouted concrete masonry, the maximum stress could be 1.5 to 2.0 times the strength for concentric loading (Drysdale

and Hamid, 1982). For hollow masonry, the strain gradient effect is not significant because the stress along the thickness of the face shell of the block is relatively uniformly distributed. The walls under analysis are partially grouted and the strain gradient in the cross-section is not considered to be significant.

5.3.4 Analysis Results

In the analysis, the loading eccentricities were selected as 0, t/12, t/6, t/3, and t/2 where t was the thickness of the block wythe. These values covered the ranges of large and small eccentricities in practice. Figure5.1 shows the load-deflection curves of one group of specimens loaded with equal eccentricities at both ends of walls. The specimens were WS1, WS4, WS2, WS5 and WS6. The properties and the loading conditions of this group of specimens are listed in Table 5.1.

Specimen WS1 is loaded with zero eccentricity. It can be seen that before reaching the ultimate load, the deflection of the specimen is very small, about one millimetre. The small deflection may be caused by the difference between the actual centroid and the nominal centroid of the specimen which is based on the centroid of the loaded wythe not the centroid of the whole cross section of the cavity wall. After reaching the ultimate load, a sharp change in the slope of the load-deflection curve indicates buckling of the specimen. After this point, the curve is flat. The deflection increases without a corresponding increase in the load. Specimens WS4, WS2, WS5, and WS6 are loaded with an eccentricity of t/12, t/6, t/3 and t/2 respectively. As expected, the analysis results shown in Fig.5.1 reveal decreasing axial load-carrying capacity with increasing eccentricity. It also shows that the curves tend to become more and more smooth around the ultimate load as the eccentricity increases. This is attributed to the nonlinear material properties and the effect of second-order moment caused by large deflections. As mentioned earlier in this section, the different shapes of the load-deflection curves confirm that the response of the masonry cavity walls is sensitive to the different combinations of axial load and bending moment.

In this investigation, the effect of the direction of the eccentricity on the stiffness and the load-carrying capacity is also studied. It is found that the effect of this parameter on the stiffness and the ultimate load capacity of the wall is not significant. Therefore, as shown in Table 5.1, most specimens in the analyses are loaded with eccentricities away from the brick wythes, a few are loaded with eccentricities towards the brick wythe to serve as a comparison. These are WA11, WA12, WA16, WA17, WS102, WS104, WS108, WS205, WS205, WS207 and WS209.

5.4 The Slenderness Ratio

Under combined axial load and bending, the axial load carrying capacity of masonry walls decreases as the wall height increases. The reduction of the axial load capacity is due to the additional moment caused by the deflection of the wall, i.e. the second order moment effect. The decrease in load carrying capacity is more significant for slender walls than for short walls. This is called the slenderness effect.

The slenderness of the wall is usually expressed in terms of the height-to-thickness ratio, L/t. A more accurate expression should account for the differences between hollow and solid masonry. In this case the height-to-radius of gyration ratio, L/r, would be accurate. For convenience, the slenderness ratio is defined as the height of the wall, L, to the thickness of the block wythe, t, in this investigation.

Three slenderness ratios: 18.3, 27.8 and 37.3 were selected for analysis. The slenderness ratio of 27.8 was also used in the experimental program. These values were chosen intentionally to cover the range of "slender walls" in practice. In Table 5.1, specimens with slenderness ratios 37.8 and 22.0 are also listed. These slenderness ratios are associated with a change in the thickness of the block wythe. Specimens with these slenderness ratios were not considered in the regression analysis for slenderness ratio. However, they were used to verify the results of the full regression analysis.

Figure 5.2 shows the load-deflection curves of three specimens loaded in the same manner and having similar geometric and material properties except for the slenderness ratio. Specimens WSL3, WS5, and WSS1 have slenderness ratios of 18.3, 27.8 and 37.3 respectively. The properties and the loading conditions of these three specimens are listed in Table 5.1. The loading eccentricity is t/3 at both ends of the walls. It is obvious that the load carrying capacity of the wall decreases as the slenderness ratio increases. It can also be observed that slender walls "soften" earlier than short walls. More results will be discussed in details in the next chapter.

5.5 The Ratio Between the Eccentricity at the Top and Bottom of the Wall: e_1/e_2

The ratio of e_1/e_2 was defined according to the relative magnitude and direction of the eccentricities applied at the top and the bottom ends of the wall. Since the smaller value is always defined as e_1, hence $|e_1/e_2| \leq 1$. For the combination causing the specimen to deform in single curvature, the ratio e_1/e_2 is positive. Accordingly, the ratio of e_1/e_2 is negative if the eccentricities cause the specimen to deflect in double curvature. In the analysis, three e_1/e_2 ratios were selected as 1; 0; and -1.

Figure 5.3 shows the load-deflection curves of three specimens with e_1/e_2 ratio as 1, 0, and -1 respectively, WSL3, WSM11, and WSM30. Their properties are listed in Table 5.1. It is obvious that with other parameters constant and only the ratio of e_1/e_2 variable, the ultimate load-carrying capacity and the deflection at the same load level changed dramatically.

It should be mentioned that the maximum deflection along the height of the wall did not occur at the same location. For the specimen loaded with e_1/e_2 ratio as 1, the maximum deflection caused by both primary moment and the P-Δ effect is at mid-height. For specimens loaded with e_1/e_2 ratio equal to 0, the maximum deflection occurred at the

height between the mid-height and the loaded end. The exact location depends on the end conditions and the relative magnitude of the end moment and the moment caused by P-Δ. For slender walls, if the magnitude of the end eccentricity is not very large, the maximum deflection point is very close to the mid-height. This was verified by the test and the analysis. Thus, for simplicity, the deflection for specimen WSM11 was measured at the mid-height of the wall. For specimen loaded with e_1/e_2 ratio equal to -1, the maximum deflection occurred at the quarter point from the top and the bottom end of the wall. The deflection of specimen WSM30 was obtained as the average of the deflections at the quarter height of both the upper and the lower part of the wall. As mentioned earlier in Chapter Three, this average value eliminates the effect of initial imperfections and the unwinding effect.

5.6 The Compressive Strength of the Block Assemblage

Depending on the magnitude of the eccentricity and other parameters, the cross-section of the wall could be fully in compression or with part of the section in tension. Therefore, the compressive and tensile strength of the block assemblage are important parameters affecting the load carrying capacity and may have an effect on the stiffness of the cavity wall.

In the analysis, it has been verified that the cracks in the masonry wall caused by tensile stresses were initiated and developed mostly at the mortar joints. For this reason as mentioned in Chapter Four, the bond strength between the mortar joint and the units was used as the tensile strength of the masonry assemblage for the numerical simulation as well as the parametric study, reported here.

A simple relationship of $f_t = 0.029\ f'_m$ was used to define the tensile (bond) strength of the block assemblage. The tensile strength was determined according to the previous research (Ghosh, 1989, Sarker and Brown, 1978). Because the compressive

strength of the block assemblage is selected as a variable, the tensile strength also changes value as the compressive strength changes.

The material strength of the brick wythes is not considered a variable since the brick wythes are not directly loaded.

Three compressive strengths for block wythe were selected, 10.0, 19.3, and 25.0 MPa. Figure5.4 shows the load-deflection curves of specimens WSF1, WSF2, and WSF3. The properties of these three specimens are listed in Table 5.1. As expected the analysis results showed in Fig.5.4 reveal that the strength of the block assemblage has an influence on the ultimate load-carrying capacity of the cavity wall. However, the three curves are approximately identical before the load reaches about 65% to 75% of the ultimate load. Therefore, this variable does not seem to have much influence on the stiffness of the wall at the initial loading stage.

5.7 The Modulus of Elasticity of the Block Assemblage

The modulus of elasticity of the block assemblage exerts a direct influence on the deflection behaviour of the cavity wall. The CAN3-S304.1-94 code defines the modulus of elasticity of the block assemblage as:

$$E_m = 850\, f'_m$$

In which, E_m is the modulus of elasticity of the block assemblage ;

f'_m is the compressive strength of the block assemblage.

This relationship can be expressed as $E_m = \alpha\ f'_m$. This simple relationship between the modulus of elasticity and the compressive strength of the block assemblage was confirmed by many researchers (Hatzinikolas, 1978). In the numerical simulation of the experimental program, the values of the compressive strength and the modulus of

elasticity of the block assemblage were both obtained directly from the prism test results. The value of α was calculated as 721. This value is about 15% smaller than that suggested by the code CAN3-S304.1-94. In order to account for the variation of the value α and to cover a wider range of the block units, three values for α were used in the parametric analysis as 721, 850, and 1000 respectively.

Figure 5.5 shows the load-deflection curves of specimens WSE1, WSE2, and WSE3. The three specimens have the same properties and loading conditions except the value of α is 721, 850, and 1000, respectively. The other properties of the specimens are listed in Table 5.1. It can be observed that the E_m value affects the slope of the deflection curve almost from the beginning of the loading. The ultimate load-carrying capacity increases as the E_m value increases. The increment in capacity, however, is not significant.

5.8 The Ratio of $(EI)_{brick}/(EI)_{block}$

The ratio of $(EI)_{brick}/(EI)_{block}$ is an artificial parameter which reflects the relative stiffness between the block wythe and the brick wythe. $(EI)_{block}$ represents the multiple of the modulus of elasticity and the moment of inertia of the block wythe while, $(EI)_{brick}$ represents the same properties of the brick wythe. Since the brick wythe is not loaded directly, the material properties of the brick wythe are relatively less important. Therefore, only the parameter $(EI)_{brick}/(EI)_{block}$ was used to reflects the composite action between the two wythes of the cavity wall and to evaluate the contribution provided by the brick wythe.

Three different values of $(EI)_{brick}/(EI)_{block}$ were selected to study this parameter. They were 0.128, 0.0524, and 0.0301. There are also two other values of $(EI)_{brick}/(EI)_{block}$: 0.0469 and 0.0399 as listed in Table 5.1. These occurred from changing the value the E_m of the block wythes. The load-deflection curves of three specimens WSB1, WSB2, and WSB3 are illustrated in Fig.5.6, having $(EI)_{brick}/(EI)_{block}$ value of

0.0524, 0.128, and 0.0301 respectively. For these three specimens, the thickness of the brick wythe was 90 mm while the thickness of the block wythe was 140 mm, 190 mm, and 240 mm, respectively. The change of relative stiffness between two the wythes was reflected in the ratio of $(EI)_{brick}/(EI)_{block}$ The other properties of the specimens are listed in Table 5.1.

5.9 The Cavity Width

It is believed that the cavity wall should become stiffer with an increasing cavity width. This is mainly due to the shift of the centroid of the cross-section and the increase of the moment of inertia as a consequence. However, this increment is affected by the efficiency and stiffness of the shear connectors. In this investigation, two cavity widths have been used: 75 mm and 100 mm. The shear connectors manufactured for 100 mm cavity width were more flexible than those for 75 mm cavity width. Figure 5.7 shows the load-deflection curves of specimen W1 and W7 obtained from the test. Specimen W1 had a cavity width of 75 mm and specimen W7 had a cavity width of 100 mm. The other parameters for these two specimens were the same except for the cross-section properties of the shear connectors and the direction of the eccentricity. Specimen W1 was loaded away from the brick wythe while specimen W7 was loaded towards the brick wythe. It can be seen that at the initial loading stage, the responses of the two specimens were almost identical. There was no obvious increase in the stiffness of wall W7 as expected. The reason was that the stiffness of the specific shear connector used in this investigation decreases as the cavity width increases. The decrease in the stiffness of the connector reduces the efficiency of the connectors as a load transfer mechanism. Therefore, less contribution has been provided by the brick wythe.

Because of the contradictory effects caused by increasing the cavity width and decreasing the stiffness of the connector, no relationship in numerical quantities has been found between the behaviour of the wall and the cavity width. Nevertheless, it appears that for cavity width varying between 75 mm and 100 mm , the variations in the stiffness

and the ultimate load capacity are not significant. Therefore, using the shear connectors specified in this research, the cavity width may be eliminated from the variable set in predicting the behaviour of cavity walls.

5.10 Summary

The variables which could affect the behaviour of the cavity walls have been carefully selected. By combination of these variables, about ninety-one cavity walls have been analyzed. Table 5.1 lists all the properties, geometry and loading conditions of the specimens in the parametric study. From the preliminary discussion of the analyses results, the following conclusions could be arrived at:

(1) The loading eccentricity e, the slenderness ratio L/t, and the ratio of e_1/e_2 are the important factors affecting the stiffness and the load-carrying capacity of the cavity wall. The loading eccentricity affects the failure mode which has been reflected in the load-deflection curves shown in Fig.5.1. The other parameters may also affect the failure mode. This will be discussed in the next chapter.

(2) The compressive and tensile strengths of the block wythe have an effect on the ultimate load-carrying capacity of the cavity wall. They do not affect the initial stiffness of the wall as illustrated in Fig. 5.4.

(3) The modulus of elasticity of the block wythe influences the deflection and load-carrying capacity, obviously.

(4) The ratio of $(EI)_{brick}/(EI)_{block}$ influences the behaviour of the wall, also obviously.

(5) The influence of the cavity width on the stiffness and load-carrying capacity was counteracted by the stiffness of the shear connector. For large cavity width and the

shear connector commonly used in practice, there is no significant change in the load-carrying capacity and the stiffness of the wall.

Table 5.1 Properties, Loading Conditions and the Ultimate Capacity of the Specimens

1	2	3	4	5	6	7	8	9	10	11	12	13	14	15
Series	Specimen	f_m' block MPa	α block	b_1 brick mm	b_2 block mm	EI_{bri}/EI_{blo}	L m	L/t	C mm	e/t	a or t	e_1/e_2	M_u P = 0 kN-m	P_u kN
1	WS1	19.3	721	90	190	0.0524	5.285	27.8	75	0	N/A	N/A		2061.0
	WS2	19.3	721	90	190	0.0524	5.285	27.8	75	1/6	a	1		1115.6
	WS3	19.3	721	90	190	0.0524	5.285	27.8	75	P = 0	a	1	12.37	
	WS4	19.3	721	90	190	0.0524	5.285	27.8	75	1/12	a	1		1442.3
	WS5	19.3	721	90	190	0.0524	5.285	27.8	75	1/3	a	1		447.8
	WS6	19.3	721	90	190	0.0524	5.285	27.8	75	1/2	a	1		168.7
2	WSB1	19.3	721	90	190	0.0524	5.285	27.8	75	1/3	a	1		447.8
	WSB2	19.3	721	90	140	0.128	3.900	27.8	75	1/3	a	1		206.1

Table 5.1 (cont'd)

Series	Specimen	f_m' block MPa	α block	b_1 brick mm	b_2 block mm	EI_{brk}/EI_{blo}	L m	L/t	C mm	e/t	a or t	e_1/e_2	M_u P=0 kN-m	P_u kN
2	WSB3	19.3	721	90	240	0.0301	6.490	27.8	75	1/3	a	1		825.6
	WSB4	19.3	721	90	190	0.0524	3.485	18.3	75	1/3	a	1		667.3
	WSB5	19.3	721	90	140	0.128	2.562	18.3	75	1/3	a	1		300.9
	WSB6	19.3	721	90	240	0.0301	4.392	18.3	75	1/3	a	1		1230.0
	WSB7	19.3	721	90	190	0.0524	7.085	37.3	75	1/3	a	1		351.8
	WSB8	19.3	721	90	140	0.128	5.222	37.3	75	1/3	a	1		181.6
	WSB9	19.3	721	90	240	0.0301	8.904	37.3	75	1/3	a	1		559.9
3	WSE1	19.3	721	90	190	0.0524	5.285	27.8	75	1/3	a	1		447.8
	WSE2	19.3	850	90	190	0.0469	5.285	27.8	75	1/3	a	1		495.2
	WSE3	19.3	1000	90	190	0.0399	5.285	27.8	75	1/3	a	1		539.6
	WSE4	19.3	721	90	190	0.0524	3.485	18.3	75	1/3	a	1		667.3
	WSE5	19.3	850	90	190	0.0469	3.485	18.3	75	1/3	a	1		739.4
	WSE6	19.3	1000	90	190	0.0399	3.485	18.3	75	1/3	a	1		811.3
	WSE7	19.3	721	90	190	0.0524	7.085	37.3	75	1/3	a	1		351.8

Table 5.1 (cont'd)

Series	Specimen	f_m' block MPa	α block	b_1 brick mm	b_2 block mm	EI_{brk}/EI_{blo}	L m	L/t	C mm	e/t	a or t	e_1/e_2	M_u P = 0 kN-m	P_u kN
4	WSE8	19.3	850	90	190	0.0469	7.085	37.3	75	1/3	a	1		386.0
	WSE9	19.3	1000	90	190	0.0399	7.085	37.3	75	1/3	a	1		421.6
	WSF1	10.0	1399	90	190	0.0524	5.285	27.8	75	1/3	a	1		398.2
	WSF2	19.3	721	90	190	0.0524	5.285	27.8	75	1/3	a	1		447.8
	WSF3	25.0	560	90	190	0.0524	5.285	27.8	75	1/3	a	1		477.2
	WSF4	10.0	1399	90	190	0.0524	3.485	18.3	75	1/3	a	1		496.3
	WSF5	19.3	721	90	190	0.0524	3.485	18.3	75	1/3	a	1		667.3
	WSF6	25.0	560	90	190	0.0524	3.485	18.3	75	1/3	a	1		706.3
	WSF7	10.0	1399	90	190	0.0524	7.085	37.3	75	1/3	a	1		316.4
	WSF8	19.3	721	90	190	0.0524	7.085	37.3	75	1/3	a	1		351.8
	WSF9	25.0	560	90	190	0.0524	7.085	37.3	75	1/3	a	1		371.6
5	WSL1	19.3	721	90	190	0.0524	7.085	37.3	75	0	N/A	N/A		1560.0
	WSL2	19.3	721	90	190	0.0524	7.085	37.3	75	1/12	a	1		1095.2
	WSL3	19.3	721	90	190	0.0524	7.085	37.3	75	1/3	a	1		351.8

Table 5.1 (cont'd)

Series	Specimen	f_m' block MPa	α block	b_1 brick mm	b_2 block mm	EI_{brk}/EI_{blo}	L m	L/t	C mm	e/t	a or t	e_1/e_2	M_u P = 0 kN-m	P_u kN
5	WSL4	19.3	721	90	190	0.0524	7.085	37.3	75	1/2	a	1		208.5
	WSL5	19.3	721	90	190	0.0524	7.085	37.3	75	P = 0	a	1	11.5	
	WSL6	19.3	721	90	190	0.0524	7.085	37.3	75	1/6	a	1		734.3
6	WSS1	19.3	721	90	190	0.0524	3.485	18.3	75	1/3	a	1		667.3
	WSS2	19.3	721	90	190	0.0524	3.485	18.3	75	1/6	a	1		1451.2
	WSS3	19.3	721	90	190	0.0524	3.485	18.3	75	1/2	a	1		317.7
	WSS4	19.3	721	90	190	0.0524	3.485	18.3	75	P = 0	a	1	13.5	
	WSS5	19.3	721	90	190	0.0524	3.485	18.3	75	0	N / A	N / A		2352.0
	WSS6	19.3	721	90	190	0.0524	3.485	18.3	75	1/12	a	1		1810.7
7	WSM1	19.3	721	90	190	0.0524	5.285	27.8	75	1/3	a	0		939.0
	WSM2	19.3	721	90	190	0.0524	5.285	27.8	75	1/12	a	0		1650.6
	WSM3	19.3	721	90	190	0.0524	5.285	27.8	75	1/2	a	0		463.0
	WSM4	19.3	721	90	190	0.0524	5.285	27.8	75	1/6	a	0		1411.3
	WSM5	19.3	721	90	190	0.0524	5.825	27.8	75	P = 0	a	0	13.67	

Table 5.1 (cont'd)

Series	Specimen	f_m' block MPa	α block	b_1 brick mm	b_2 block mm	EI_{brk}/EI_{blo}	L m	L/t	C mm	e/t	a or t	e_1/e_2	M_u P = 0 kN-m	P_u kN
7	WSM6	19.3	721	90	190	0.0524	3.485	18.3	75	1/3	a	0		1201.0
	WSM7	19.3	721	90	190	0.0524	3.485	18.3	75	1/2	a	0		689.8
	WSM8	19.3	721	90	190	0.0524	3.485	18.3	75	1/12	a	0		2020.2
	WSM9	19.3	721	90	190	0.0524	3.485	18.3	75	1/6	a	0		1762.0
	SM10	19.3	721	90	190	0.0524	3.485	18.3	75	P = 0	a	0	13.75	
	SM11	19.3	721	90	190	0.0524	7.085	37.3	75	1/3	a	0		610.0
	SM12	19.3	721	90	190	0.0524	7.085	37.3	75	1/12	a	0		1261.6
	SM13	19.3	721	90	190	0.0524	7.085	37.3	75	1/2	a	0		351.6
	SM14	19.3	721	90	190	0.0524	7.085	37.3	75	1/6	a	0		1068.8
	SM15	19.3	721	90	190	0.0524	7.085	37.3	75	P = 0	a	0	13.63	
8	SM16	19.3	721	90	190	0.0524	5.285	27.8	75	1/12	N/A	-1		1919.7
	WSM17	19.3	721	90	190	0.0524	5.285	27.8	75	1/2	N/A	-1		738.0
	SM18	19.3	721	90	190	0.0524	5.285	27.8	75	1/6	N/A	-1		1756.8
	WSM19	19.3	721	90	190	0.0524	5.285	27.8	75	P = 0	N/A	N/A	13.83	

Table 5.1 (cont'd)

Series	Specimen	f_m' block MPa	α block	b_1 brick mm	b_2 block mm	EI_{brf}/EI_{blo}	L m	L/t	C mm	e/t	a or t	e_1/e_2	M_u P = 0 kN-m	P_u kN
8	WSM20	19.3	721	90	190	0.0524	5.285	27.8	75	1/3	N/A	-1		1248.0
	WSM21	19.3	721	90	190	0.0524	3.485	18.3	75	1/12	N/A	-1		2224.8
	WSM22	19.3	721	90	190	0.0524	3.485	18.3	75	1/2	N/A	-1		767.2
	WSM23	19.3	721	90	190	0.0524	3.485	18.3	75	1/6	N/A	-1		1856.0
	WSM24	19.3	721	90	190	0.0524	3.485	18.3	75	P = 0	N/A	N/A	13.73	
	WSM25	19.3	721	90	190	0.0524	3.485	18.3	75	1/3	N/A	-1		1253.6
	WSM26	19.3	721	90	190	0.0524	7.085	37.3	75	1/12	N/A	-1		1492.0
	WSM27	19.3	721	90	190	0.0524	7.085	37.3	75	1/2	N/A	-1		624.0
	WSM28	19.3	721	90	190	0.0524	7.085	37.3	75	1/6	N/A	-1		1397.5
	WSM29	19.3	721	90	190	0.0524	7.085	37.3	75	P = 0	N/A	N/A	13.66	
	WSM30	19.3	721	90	190	0.0524	7.085	37.3	75	1/3	N/A	-1		1076.0
9	WA11	19.3	721	90	190	0.0524	5.285	27.8	75	1/3	t	1		471.0
	WA7	19.3	721	90	190	0.0524	5.285	27.8	100	1/3	t	1		424.0
	WA12	19.3	721	90	190	0.0524	5.285	27.8	100	1/3	a	1		403.5

Table 5.1 (cont'd)

Series	Specimen	f_m' block	α block	b_1 brick	b_2 block	EI_{brk}/EI_{blo}	L	L/t	C	e/t	a or t	e_1/e_2	M_u P = 0	P_u
		MPa		mm	mm		m		mm				kN-m	kN
9	WA16	19.3	721	90	190	0.0524	5.285	27.8	100	1/2	t	1		224.40
	WA17	19.3	721	90	190	0.0524	5.285	27.8	100	1/2	a	1		208.4
	WS101	19.3	721	90	140	0.128	5.285	37.8	75	1/2.2	a	1		180.5
	WS102	19.3	721	90	140	0.128	5.285	37.8	75	1/2.2	t	1		191.8
	WS103	19.3	721	90	240	0.0301	5.285	22.0	75	1/3.9	a	1		1078.8
	WS104	19.3	721	90	240	0.0301	5.825	22.0	75	1/3.9	t	1		1100.0
	WS107	19.3	721	90	240	0.0301	5.285	22.0	75	1/2.7	a	1		517.6
	WS108	19.3	721	90	240	0.0301	5.285	22.0	75	1/2.7	t	1		528.6
	WS204	19.3	721	90	190	0.0524	5.285	27.8	100	1/3	a	0		908.2
	WS205	19.3	721	90	190	0.0524	5.285	27.8	100	1/3	t	0		932.4
	WS207	19.3	721	90	190	0.0524	5.285	27.8	75	1/2	t	0		480.6
	WS208	19.3	721	90	190	0.0524	5.285	27.8	100	1/2	a	0		437.7
	WS209	19.3	721	90	190	0.0524	5.285	27.8	100	1/2	t	0		456.4

Table 5.1 (cont'd)

Note:

Column 1: Series number;
Column 2: Name of the specimens;
Column 3: f_m' = Compressive strength of the block assemblage;
Column 4: $\alpha = E_m / f_m'$, Coefficient between the compressive strength and the modulus of elasticity of the block assemblage;
Column 5: b_1 = Thickness of the brick wythe;
Column 6: b_2 = Thickness of the block wythe;
Column 7: EI_{bri}/EI_{blo} = Ratio of $(EI)_{brick}/(EI)_{block}$;
Column 8: L/t = Slenderness ratios;
Column 9: C = Cavity width;
Column 10: e/t = Ratios of the loading eccentricity to the thickness of the walls;
Column 11: a or t = The direction of the eccentricity was away (a) or towards (t) the brick wythe;
Column 12: e_1 / e_2 = Ratios of the eccentricities at the top and the bottom ends of the walls;
Column 13: M_u = The maximum moment capacity of the specimen under pure bending;
Column 14: P_u = The maximum load carrying capacity of the specimen.

Specimens WS3, WSE1, WSB1 and WSF2 are identical; Specimens WSB4,WSE4 , WSF5 and WSS1 are identical; Specimens WSB7, WSE7, WSF8 and WSL8 are identical.

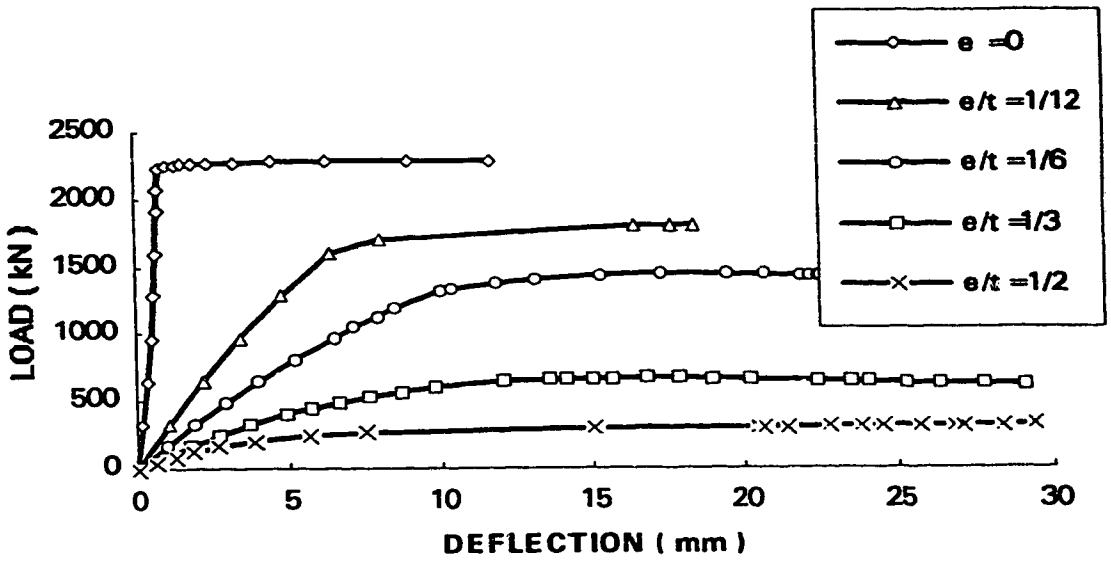

Figure 5.1 Load deflection curves of specimens WS1, WS4, WS2, WS5, and WS6

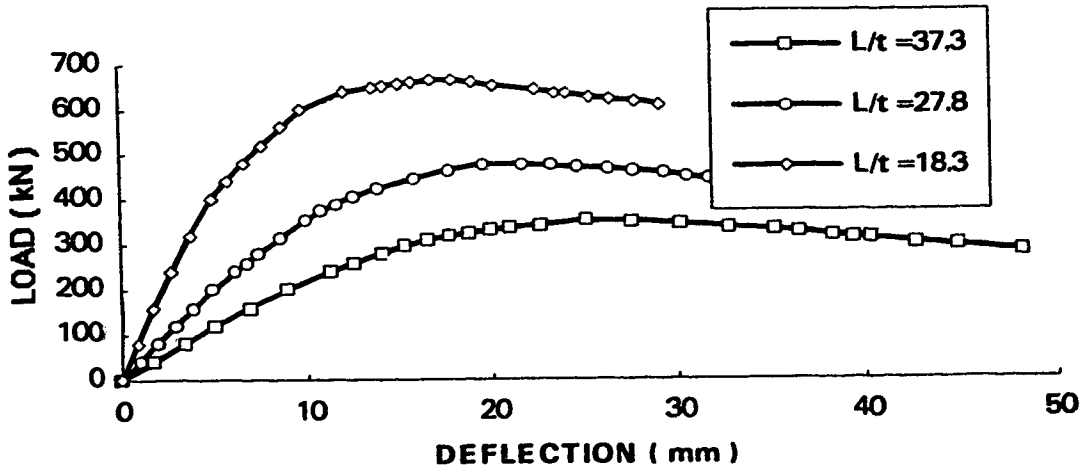

Figure 5.2 Load deflection curves of specimens WSL3, WS5, and WSS1

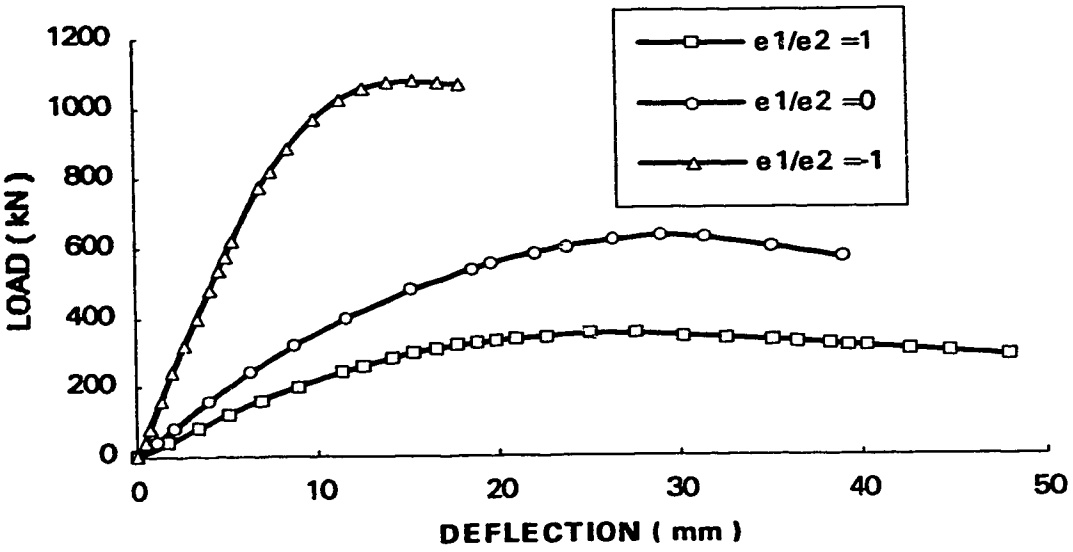

Figure 5.3 Load-deflection curves of specimens WSL3, WSM11, and WSM30

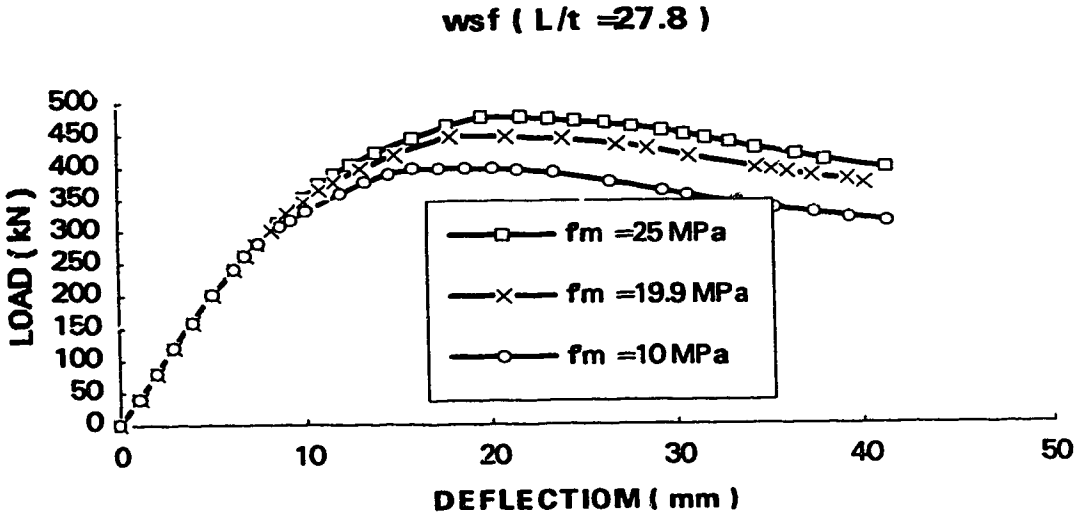

Figure 5.4 Load-deflection curves of specimens WSF1, WSF2, and WSF3

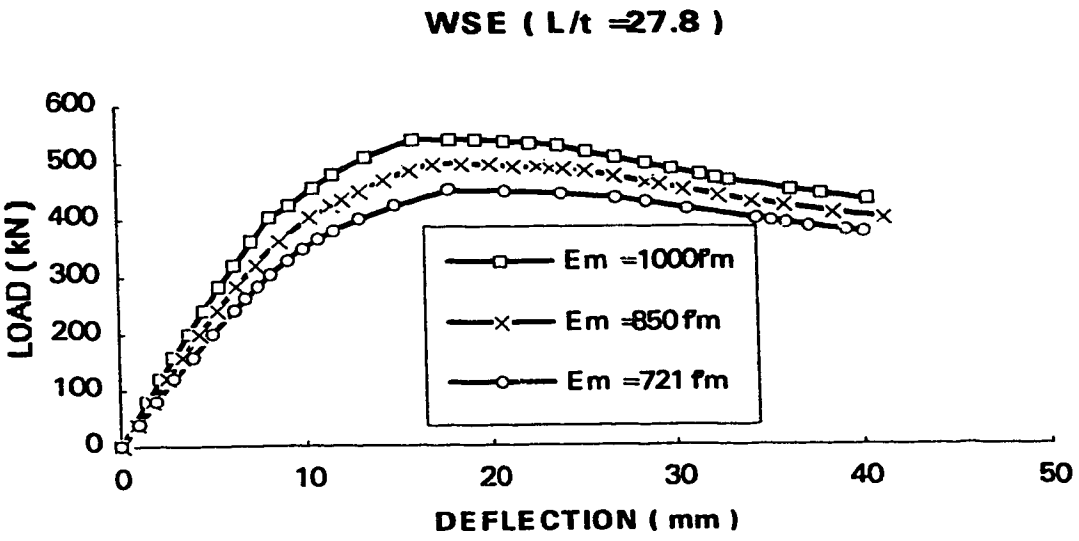

Figure 5.5 Load-deflection curves of specimens WSE1,WSE2, and WSE3

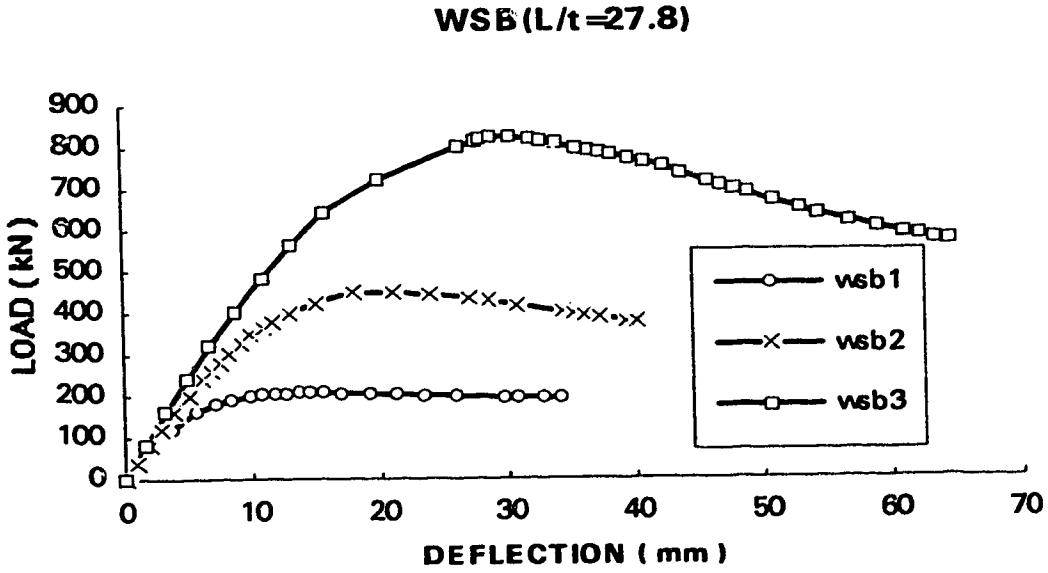

Figure 5.6 Load-deflection curves of specimens WSB1, WSB2, and WSB3

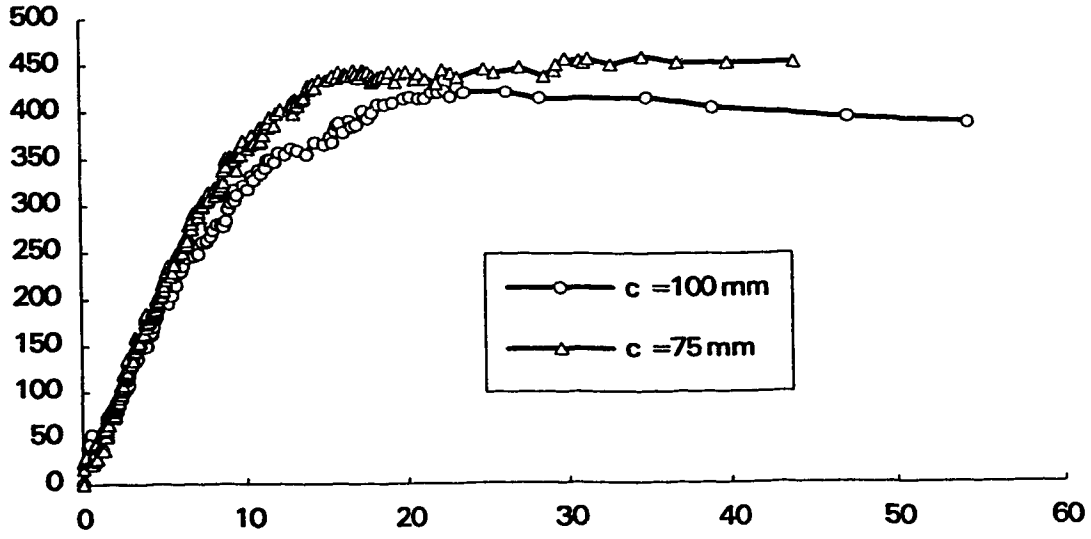

Figure 5.7 Load-deflection curves of specimens W1 and W7

CHAPTER SIX

DESIGN OF SLENDER MASONRY CAVITY WALLS

6.1 Introduction

Slender masonry cavity walls exhibit a non-linear load-deflection response when subjected to combined axial load and out-of-plane bending. As analyzed and discussed in the previous chapters, the response of each specimen was a complex function of the loading conditions, the geometry, and the material properties of the wall. As a result, rigorous analysis as a design method for slender masonry cavity walls is a rather complicated matter and is generally too complex to be efficiently used in practice. On the other hand the moment magnifier method is generally accepted as a rational approximate approach. The difficulty in executing this method lies in the proper evaluation of the effective stiffness of the wall, *EI*. For this purpose, nine full scale cavity walls have been tested and about ninety-one computer simulated cavity walls subjected to short-time loads have been analyzed by this investigation. Based on the results of the experiments and analyses, a multi-linear regression analysis was carried out to evaluate the value of effective stiffness of the wall. This will be presented in the following sections.

To demonstrate the effects of the parameters analyzed in the computer tests, more analysis results will be presented in this chapter along with a further discussion on the behaviour of the masonry cavity walls under combined axial load and bending moment. A rational design procedure for slender masonry cavity walls is proposed in which the effects of the variations of the major variables are considered. A comparison between the proposed design formula and the tests as well as the analysis results will be addressed in section 6.8.

6.2 Behaviour of Slender Masonry Cavity Walls

The behaviour of slender masonry cavity walls is influenced by a number of variables. A large number of cavity walls has been analyzed using the finite element model tested and verified in Chapter Five against the results of physical tests. In Chapter Five, the analysis results have been displayed in the form of load-deflection curves of the specimens. In this section, a more detailed discussion of the analysis results is presented through a number of different curves and diagrams which demonstrate the relationship between some of the significant variables.

6.2.1 Slenderness Effects

An efficient way of discussing the slenderness effect on the walls is through the interaction diagrams. When a pin-ended wall loaded with a vertical load, P, at an eccentricity, e, giving rise to symmetric end moments $M = Pe$ at its two ends, the wall deflects at mid-height laterally by an amount Δ. The magnitude of Δ is dependent among other factors on the slenderness ratio of the wall and on its geometric and material properties. The maximum moment is, thus, is $P(e + \Delta)$ and occurs at mid-height of the wall. Figure 6.1 shows an interaction diagram of a wall. The curve DABCG is the interaction diagram for the cross-section. It represents the combined axial load and the bending moment required to cause the failure of the cross-section. The line O-A represents the axial load versus the end moment of the wall, Pe, while the line O-B describes the axial load versus the maximum moment at mid-height of the wall. The difference between the two lines is usually referred to as the second order effect.

For slender walls, the second order moment caused by the lateral deflection Δ can be significant. As shown in Fig. 6.1, the actual failure occurs when the second order response line O-B intersects the interaction diagram DABCG at point B. The difference of the moments between the points B and B' is the additional moment caused by lateral deflection. The corresponding increase in longitudinal stresses results in material damage which shows as the reduction in the axial load capacity between the theoretical point A

and the second order point B'. In order to study the effect of the slenderness and other variables, the slender wall interaction diagrams need to be plotted. The construction of such interaction diagrams for slender walls can be based on the results obtained from the parametric results of Chapter 5. For each failure case of slender wall, a point corresponding to the axial load capacity and the nominal end moment *Pe* is plotted as represented by points B' or C' as shown in Fig. 6.1. The broken line DB'C'G passing through points B' and C' is the slender wall interaction diagram corresponding to a slenderness ratio *L/t*. By varying the slenderness ratio, a family of slender wall interaction diagrams can be constructed. The construction of the slender wall interaction diagram was based on the end moment not the maximum moment because in practice, the end moment is readily available to designers as opposed to the maximum moment.

The group of figures 6.2 shows a family of slender cavity wall interaction diagrams of the specimens analyzed in Chapter 5. Figure 6.2(a) shows the interaction diagrams for the specimens loaded with equal end moment at the two ends, $e_1/e_2 = 1$. Figures 6.2(b) and (c) show the interaction diagrams for the specimens loaded with $e_1/e_2 = 0$, and $e_1/e_2 = -1$, respectively. Within each of these figures, three curves are plotted for three slenderness ratios of 13.3, 27.8 and 37.3. It is clear from Fig. 6.2(a) that the interaction diagram with larger slenderness ratio always falls inside that with a smaller slenderness ratio. This indicates that an increase of the slenderness ratio reduces the load carrying capacity. However, as shown in Fig. 6.2(c), in the presence of a large eccentricity and an end moment ratio $e_1/e_2 = -1$, i.e. the specimen bent in double curvature, the reduction of the capacity due to the slenderness is not obvious. This is because when the wall is loaded with equal end moment, the moment caused by deflection will always contribute to the total maximum moment thus the slenderness ratio play a part in the load carrying capacity. When the wall is loaded with $e_1/e_2 = -1$ and forced to deflect in double curvature, the second order effects are not as high and failure is primarily governed by material failure.

6.2.2 Magnitude of Load Eccentricity

In Chapter Five, Fig. 5.3 presented the load deflection curves for five specimens with a slenderness ratio of 27.8 and five different load eccentricities of 0, *t/12*, *t/6*, *t/3* and *t/2*. Figure 6.3 shows a family of curves of load-carrying capacity versus loading eccentricity to reveal the influence of the loading eccentricity, *e/t*, on the strength of the cavity walls. The three curves are for three slenderness ratios, *L/t*, of 18.3, 27.8, and 37.3. It is clear that the ultimate load-carrying capacity is significantly reduced as the eccentricity ratio, *e/t*, increases. Also the figure shows that the reduction of the load carrying capacity is more severe in the range of small eccentricities and less so for large eccentricities.

6.2.3 Effect of Material Properties

To study the effects of the material properties on the behaviour of the cavity walls, the analysis results of Chapter 5 with varying material properties have been plotted into a series of curves. Figure 6.4 shows a family of ultimate load versus slenderness ratio *L/t* curves for three different compressive strength values, f'_m, of 10.0, 19.3, and 25.0 MPa, a corresponding curve of ultimate load versus slenderness ratio, *L/t*, is plotted as shown in Figure 6.4. Each point in the curve represents the analysis result from one specimen. The specimens were all pin-ended and were loaded with an equal end eccentricity of *t/3* at both ends of the walls. Increasing the strength of the block masonry, naturally, increases the capacity of the wall. The influence of the strength, however, is less significant in the range of large eccentricity because the second order effect is then more severe.

To explore the influence of the modulus of elasticity, E_m , of the block wythe, a family of curves from the analysis results are presented in Fig. 6.5. Each curve plots the ultimate load versus The slenderness ratio for three different values of $E_m = 721 f'_m$, $850 f'_m$, and $1000 f'_m$. Here f'_m is 19.3 MPa. The specimens were loaded with an equal end eccentricity of *t/3* at both ends of the wall. It can be observed that increasing the E_m value enhances the capacity of the wall. The enhancement is not affected by the height of the wall.

6.2.4 Effect of Stiffness Ratio $(EI)_{brick}/(EI)_{block}$

The stiffness ratio, $(EI)_{brick}/(EI)_{block}$, stands for the relative stiffness of the block wythe and the brick wythe. It reflects, partially, the degree of the composite action between the two wythes. Since the brick wythe has a fixed width of 90 mm, the stiffness ratio is changed by changing the size of the block wythe. Figure 6.6 shows the ultimate load versus the slenderness ratio for three different values of the stiffness ratio, 0.0301, 0.0524 and 0.128. For each value of $(EI)_{brick}/(EI)_{block}$ ratio, two curves are plotted, one for a cavity wall and the other for a single wythe wall with the same block size. All the specimens were loaded with an equal end eccentricity of $t/3$ at both ends of the walls. It can be seen from the curves that the ultimate load capacity of the cavity walls is significantly higher than that of the corresponding single walls. The percentage increase is higher for the wall with larger stiffness ratio. This is because the larger the ratio of $(EI)_{brick}/(EI)_{block}$, the more the brick wythe contributes to the total capacity of the wall. Figure 6.6 also show that the strength gained by slender cavity walls is slightly higher than that by the shorter cavity walls.

6.2.5 Summary

Figures 6.2 and 6.3 indicate that the slenderness ratio L/t, the end moment ratio e_1/e_2 and the loading eccentricity e/t are important variables which influence the capacity of the cavity wall. The above discussion revealed that these three variables are, in some extent, interrelated. In addition one would expect the material properties, represented by f'_m and E_m, and the geometric construction of the wall, $(EI)_{brick}/(EI)_{block}$, also to influence the wall response to varying degrees.

6.3 The Moment Magnifier Method

From the above discussion, it is clear that a rational design method for masonry cavity walls should meet a number requirements. It should consider the secondary moment effect. It should be able to reflect the effect of slenderness, the effect of nonlinear material properties as well as the contribution to the load capacity provided by the brick wythe. In

addition, it should be accurate but with reasonable simplicity. At present, a rigorous second-order analysis is not practical in the design of masonry cavity walls. The moment magnifier method is an approximate approach that could meet the above requirements. Here the wall is designed for the expected axial load in combination with the applied bending moment magnified to reflect the second order effects. The moment magnifier should be a function of the slenderness ratio and the geometry and effective stiffness of the wall. Compared to the other approximate methods, the moment magnifier method has the advantages of rationality, accuracy, and ease of use (MacGregor 1970). The current masonry design code-Code S304.1-94 has adopted the moment magnifier method. However, up to the present, there is no direct guide for estimating the moment magnifier for cavity walls. In addition, the contribution of the brick wythe to the effective stiffness of the wall is neglected.

To apply the moment magnifier method efficiently to masonry cavity walls, simple semi-rational expressions of the moment magnifier that could be applied directly to the cavity wall are derived in the following. The derivation of the moment magnifier is conducted in such a way that the existence of the brick wythe is considered in the context of an effective stiffness of the whole wall. First, the derivation of the theoretical moment magnifier for both equal and unequal end moment situations is described in this section along with a discussion of the moment magnifier method adapted by Code CAN3-304.1-94. Later the effective stiffness of the cavity wall is obtained through a linear regression analysis of the results of Chapter 5.

6.3.1 Moment Magnifier for Pin-Ended Cavity Wall Loaded with Equal End Eccentricity

To derive the moment magnifier expression, the masonry cavity walls under discussion are simplified as a beam-column loaded and restrained at the ends as shown in Fig. 6.7(a). The general differential equation that governs the behaviour of the beam-column is:

$$EI\ v'' + Pv = M_2 - \frac{z}{L}(M_1 + M_2) \tag{6.1}$$

in which v is the deflection. For equal end moments $M_1 = -M_2 = M$. Let $M = Pe$, and $k^2 = P/EI$. The general solution form for this equation is well known:

$$v = A\sin(kz) + B\cos(kz) - e$$

By applying the boundary conditions, the maximum lateral deflection v_{max} occurs at the mid-height of the beam-column and is expressed as:

$$v_{1/2} = v_{max} = e\left(\tan\left(\frac{kL}{2}\right)\sin\left(\frac{kL}{2}\right) + \cos\left(\frac{kL}{2}\right) - 1\right) = e\left(\sec\left(\frac{kL}{2}\right) - 1\right)$$

Expanding $\sec\left(\frac{kL}{2}\right)$, and substitute $(kL)^2 = \pi^2\left(\frac{P}{P_{cr}}\right)$, the mid-height deflection is obtained as,

$$\Delta = v_{max} = v_o\left(\frac{1}{1 - P/P_{cr}}\right) \tag{6.2}$$

In which, $v_o = \frac{PeL^2}{8EI}$ is the deflection under the initial end moment Pe, and P_{cr} is Euler buckling load, $P_{cr} = \frac{\pi^2 EI}{L^2}$. The maximum magnified moment is, thus, obtained as:

$$M_{max} = Pe + Pv_{max} = Pe\left(1 + \frac{\pi^2}{8}\frac{P}{P_{cr}}\left(\frac{1}{1 - P/P_{cr}}\right)\right) = Pe\left(\frac{1 + 0.23\,P/P_{cr}}{1 - P/P_{cr}}\right) \tag{6.3}$$

Or simply

$$M_{max} = Pe\delta = M_o\delta \tag{6.4}$$

In which, δ is the so called moment magnifier. For the pin-ended wall with equal end moment:

$$\delta = \left(\frac{1 + 0.23 P/P_{cr}}{1 - P/P_{cr}} \right) \tag{6.5}$$

6.3.2 Moment Magnifier for Pin-Ended Wall with e_1 / e_2 Ratio Equals to 0, and -1

In the case of equal end eccentricity the maximum second order moment occurs at the same section as the applied end moment (Pe is uniform along the length of the specimen). Therefore, the maximum total moment can be obtained by adding the maximum moments from the two sources directly. However, for the beam-column subjected to unequal end moments, i.e. with a moment gradient along the length of the element as shown in Fig. 6.7(b), the maximum moments caused by the applied force and the deflection do not necessarily occur at same location. The moment magnifier for this case is discussed as follows:

The governing equation (6.1) can be simplified as:

$$EIv'' + Pv = -M_2 \left(1 - (1+\beta)\frac{z}{L} \right) \tag{6.6}$$

in which, $\beta = \frac{M_1}{M_2}$ is the end moments ratio. Note that in the derivation of the moment magnifier, $\beta = 1$ stands for the moments in the direction as labelled in Fig. 6.7(b), that is $\beta = 1$ when the beam-column bent in double curvature, whereas $\beta = -1$ when the beam-column bent in single curvature, and therefore $-1 \le \beta \le 1$.

The general solution is obtained as:

$$v = A\sin(kz) + B\cos(kz) - e\left(1 - (1+\beta)\frac{z}{L} \right)$$

in which $k^2 = \frac{P}{EI}$ and $M_o = Pe$. Introducing the boundary conditions it is easy to obtain an expression for the deflection:

$$v = e\left(\frac{\sin k(L-Z) - \beta \sin kZ}{\sin kL} - 1 + (1+\beta)\frac{Z}{L}\right) \tag{6.7}$$

By differentiating Eq.6.7 an expression for the bending moment distributions obtained:

$$M = -EIv'' = Pe\left(\frac{\sin(k(L-z)) - \beta \sin(kz)}{\sin(kL)}\right) \tag{6.8}$$

The condition for maximum moment can also be obtained by differentiating Eq. 6.8 once and setting the derivative equal = 0:

$$\tan kZ = \frac{\beta - \cos kL}{-\sin kL} \tag{6.9}$$

Here Z is the location of maximum moment. From Eq. 6.9, $\beta > cos(kL)$ only if Z is negative. Therefore , $M_{max} = M_o$, i.e. , the maximum moment occurs at the end of the specimen. This situation occurs for a shorter beam-column, or a very large eccentricity applied at the end of the specimen.

On the other hand, for a slender beam-column with a small end eccentricity $\beta < cos(kL)$, and Z is positive. Extracting β from Eq. 6.9 and substituting in Eq. 6.7 , the maximum moment is obtained as:

$$M_{max} = M_o \sec kZ \tag{6.10}$$

It is clear that the location of the maximum moment and the moment magnifier is a function of the end moment ratio β and the load level P/P_{cr}. As a result, the maximum moment Pe_{max} and the maximum second order moment Pv_{max} (or as usually called $P\Delta_{max}$)

can not be added directly. It is also clear that the maximum total moment is smaller than the sum of the maximum primary moment and the maximum secondary moment. i.e. $M_{max} \leq M_{o\,max} + Pv_{max}$.

The Case for $\beta = 0$:

It is easy here to consider the deflection at mid-height, $Z = L/2$ The corresponding deflection is obtained form Eq. 6.7 as:

$$\Delta = v = \frac{M_o}{P}\left(\frac{\sin\frac{kL}{2}}{\sin kL} - \frac{1}{2}\right) = \frac{M_o}{2P}\left(\sec\frac{kL}{2} - 1\right) \tag{6.11}$$

Noting :that $k^2 = \frac{P}{EI}$, and expanding $\sec\frac{kL}{2}$ the deflection Δ is obtained as:

$$\Delta = v = \frac{M_o}{16}\frac{L^2}{EI}\left(\frac{1}{1-\frac{P}{P_{cr}}}\right) = \Delta_o \frac{1}{1-\frac{P}{P_{cr}}} \tag{6.12}$$

In which, $\Delta_o = \frac{M_o L^2}{16EI}$, is the first-order deflection at mid-height of the beam-column subjected to a moment of M_o at one end of the specimen. The magnified moment at this section is:

$$M_o = P\left(\frac{e}{2} + \Delta\right) = P\frac{e}{2}\left(\frac{1 + 0.23\frac{P}{P_{cr}}}{1-\frac{P}{P_{cr}}}\right) = Pe\delta \tag{6.13a}$$

$$\delta \approx \frac{P(0.5e + \Delta)}{Pe} = \frac{1}{2}\left(\frac{1 + 0.23\frac{P_u}{P_{cr}}}{1-\frac{P_u}{P_{cr}}}\right) \tag{6.13b}$$

The Case for $\beta = 1$:

This is the case of double curvature with equal eccentricities. Here the maximum second order deflection occurs at $Z = \frac{3L}{4}$ or $Z = \frac{L}{4}$. Substitute $Z = \frac{3L}{4}$, and $\beta = 1$ into equation (6.7) to obtain the corresponding deflection as :

$$\Delta = \frac{M_o}{P}\left(\frac{\sin\left(\frac{kL}{4}\right) - \sin\left(3\frac{kL}{4}\right)}{\sin(kL)} - 1 + 2 \times \frac{3L}{4L}\right) \tag{6.14}$$

Eq. 6.4 can be simplified as:

$$\Delta = \frac{M_o}{2P}\left(1 - \sec\left(\frac{kL}{4}\right)\right) \tag{6.15}$$

Expanding $\sec\frac{kL}{4}$, and noting that $k^2 = \frac{P}{EI}$, $(kL)^2 = \pi^2\left(\frac{P}{P_{cr}}\right)$,

$$\Delta = \frac{M_o L^2}{64EI}\left(\frac{1}{1 - \frac{P}{4P_{cr}}}\right) \tag{6.16}$$

The magnified moment at this section is:

$$M = \frac{M_o}{2} + P\Delta = P\left(\frac{e}{2} + \Delta\right) = Pe\delta \tag{6.17a}$$

$$\delta \approx \frac{P(0.5e + \Delta)}{Pe} = \frac{1}{2}\left(\frac{1 + 0.23\frac{P_u}{4P_{cr}}}{1 - \frac{P_u}{4P_{cr}}}\right) \tag{6.17b}$$

6.3.3 The Moment Magnifier Method Adopted by the Current Masonry Code

The current Canadian masonry design code S304.1 requires that the effect of slenderness should be considered for a masonry wall with

$$kL/t > \left(10 - 3.5\left(\frac{e_1}{e_2}\right)\right) \tag{6.18}$$

The wall shall be designed to resist the factored axial load P_f obtained from first-order analysis and the magnified moment that includes the second-order effect caused by lateral displacement of the wall. The magnified moment is obtained from the factored primary moment magnified by δ as:

$$M_{tot} = \delta M_{pf} \tag{6.19a}$$

$$\delta = \frac{C_m}{1 - \frac{P_f}{P_{cr}}} \tag{6.19b}$$

Here C_m accounts for the end moment ratio and P_{cr} is the Euler buckling load.

$$C_m = 0.6 + 0.4M_1/M_2 \geq 0.4 \tag{6.20a}$$

$$P_{cr} = \frac{\pi^2 \phi_e (EI)_{eff}}{[(1 + 0.5\beta_d)(kL)^2]} \tag{620b}$$

in which, $(EI)_{eff}$ is the effective stiffness. The stiffness is calculated from the modulus of elasticity, $E_m = 850f'_m$, and the prism moment of inertia, I_o. it is taken as

$$(EI)_{eff} = 0.4\, E_m I_o \qquad \textit{For unreinforced masonry} \tag{6.21a}$$

$$(EI)_{eff} = E_m\left(0.25I_o - (0.25I_o - I_{cr})\left(\frac{(e - e_k)}{(2e_k)}\right)\right) \qquad \textit{For reinforced masonry} \tag{6.21b}$$

in which:

$e = M_f/P_f$

$e_k = S/A_e$

S = section modulus

A_e = the effective cross-sectional area used for design.

$(EI)_{eff}$ shall not be taken greater than $0.25\ E_m I_o$, but need not be taken as less than $E_m I_{cr}$. Here I_{cr} = the moment of inertia of the compression zone and the transformed area of the tension steel and /or the tied compression reinforcement about the centroidal axis of the cracked section when subjected to a pure moment, M_o.

Comparing the formula specified by Code CAN3-304.1-94 with the theoretical derivation discussed in Section 6.3.1 and 6.3.2, there are some aspects that need to be noted. First, in the theoretical derivation the materials are assumed to be linear elastic. To consider the effect of cracking, creep, and the inelastic non-homogenous material properties for masonry wall, the code uses the effective moment of inertia $(EI)_{eff}$ to replace the EI in the theoretical formula. However in dealing with cavity walls, it is not convenient to use the expression given by the code to consider the existence of the brick wythe. The difficulty lies in the proper evaluation of the effective values for I_o and I_{cr} for cavity wall. Therefore the contribution provided by the brick wythe is usually neglected. This will underestimate the capacity of the cavity wall. In the next section, the evaluation of the $(EI)_{eff}$ for cavity wall carried out by this research is described.

Second, as has mentioned earlier, when the wall is subjected to unequal end moments, the maximum total moment is smaller than the sum of the maximum primary moment and the maximum secondary moment. i.e. $M_{max} \leq M_{omax} + Pv_{max}$. Therefore, if a unique expression of the moment magnifier is used for all the loading situations as is the case in the current code expression, consideration should be given to the beneficial effect caused by unequal end moments. Austin's equivalent moment factor C_m (Austin 1961) is

accepted by the current code to relate the actual moment diagram to an equivalent uniform moment diagram

Third, comparing equation (6.5) with equation (6.19b), it can be seen that the term *0.23P/Pcr* in the theoretical formula (6.3) has been neglected by the code. For slender masonry walls loaded with large eccentricity, the ultimate load carrying capacity decreases considerable from the Euler buckling load due to the effect of slenderness. Thus, $0.23P/Pcr << 1$. The simplification of neglecting item *0.23P/Pcr* is acceptable. However, for a small or moderate eccentricity, this simplification is on the unconservative side.

Fourth, because the end conditions for cavity walls described in the tests and analyses are typical and assume no restriction of rotation at the two ends of the wall, the effective length factor k is taken as 1.0. This is acceptable and assumed throughout this investigation.

6.4 Effective Stiffness of Cavity Walls

The proper evaluation of the effective stiffness $(EI)_{eff}$ is the major difficulty in applying the moment magnifier method to masonry compression members. This is because of the high variability of the factors reflected in this term. For masonry cavity walls, the effective stiffness should be able to reflect the effect of slenderness, the effect of the nonlinear stress-strain response as well as the contribution provided by the brick wythe to the load capacity of the cavity wall. This section will present the evaluation of $(EI)_{eff}$.

Noting that the nominal stiffness value E_mI_o of the block wythe can be calculated directly as long as the cross-section dimensions and the prism material properties are known, a simple approach would express $(EI)_{eff}$ as a function of the nominal stiffness value E_mI_o as:

$$(EI)_{eff} = \alpha (E_m I_o) \tag{6.23}$$

in which, α is a non-dimensional factor which depends on the variables including the load eccentricity, the material properties as well as the geometry of the cavity wall:

$$\alpha = F(L/t,\ e/t,\ f'_m,\ (EI)_{brick}/(EI)_{block},\ \text{etc.}) \tag{6.24}$$

If one can evaluate the effective stiffness $(EI)_{eff}$ corresponding to each specimen in the tests and numerical analyses, the factor α is then easily calculated from Eq. 6.23 through a multi-linear regression analysis of different combinations of the variables in Eq. 6.24

6.4.1 Test and Analysis Results of EI

The value of $(EI)_{eff}$ can be obtained by rearranging the magnified deflection derived in Section 6.3. In the case of equal end moments (e1/e2=1), rearrange Eq. 6.5:

$$P_{cr} = \frac{P(1.23e + \Delta)}{\Delta} \tag{6.25}$$

Substitute $P_{cr} = \frac{\pi^2 E I_{eff}}{L^2}$ into the above equation, and rearrange again to extract $(EI)_{eff}$:

$$E I_{eff} = \frac{PL^2}{\pi^2}(1.23\frac{e}{\Delta} + 1) = PL^2(0.1246\frac{e}{\Delta} + 0.1013) \qquad (\beta = -1) \tag{6.26}$$

For a specimen with a specified length and loading condition, an $(EI)_{eff}$ value corresponding to each failure case with the load capacity P_u and the deflection Δ can be obtained from Eq. 6.26.

The same approach applies to the cases of unequal end moments. For, rearrange Eq. 6.8, note that $\Delta_o = \frac{M_o L^2}{16EI}$, substitute for P_{cr} and extract $(EI)_{eff}$:

$$EI = PL^2\left(0.0625\frac{e}{\Delta} + 0.1013\right) \qquad (\beta = 0) \tag{6.27}$$

For the case of $\beta = 1$, i.e. $e_1/e_2 = -1$, rearrange Eq. 6.17, note that $\Delta_o = \frac{M_o L^2}{64EI}$, and substitute for P_{cr}:

$$EI = PL^2\left(0.01562\frac{e}{\Delta} + 0.02604\right) \qquad (\beta = 1) \qquad (6.28)$$

For each specimen conducted by the tests and analyses, the deflections corresponding to each load step were recorded throughout the tests and analyses. Using Eqs. 6.16, 6.17 and 6.18 a value of $(EI)_{eff}$ corresponding to each load step of the tests and the analyses can be obtained because the values of e and L in the equations are constant for a specified specimen. A curve of the stiffness $(EI)_{eff}$ versus the load P was plotted for each specimen. Figures 6.8(a) to 6.8(e) show such curves of a number of specimens. It can be seen that almost all the curves exhibit two distinct parts. The first part is from initial loading up to a load level of about $P = 0.67P_u$. The curves are fairly flat indicating that the $(EI)_{eff}$ value for this part is almost constant for a given specimen for a specific loading condition. The second part is from about $P = 0.67\,P_u$ to failure. The $(EI)_{eff}$ value in this stage changes dramatically. For the design purpose, two $(EI)_{eff}$ values have been evaluated for each specimen from these curves.

The first value of $(EI)_{eff}$ corresponds to the serviceability limit state design of the wall and is estimated from the flat part of the curves. This $(EI)_{eff}$ value is to be used in the calculation of the deflection under specified load and will be called $(EI)_{spec}$. Even though the derivation of the $(EI)_{spec}$ for the calculation of the deflection is not the main objective of this research and the proper evaluation of $(EI)_{spec}$ may need more considerations, the $(EI)_{spec}$ value evaluated here aims to provide more information for the research in this field. After carrying out a regression analysis, a simple expression has been found as:

$$EI_{spec} = \left(0.754 + 0.28\frac{e}{t} + 0.0075\frac{L}{t} + 1.36\frac{(EI)_{brick}}{(EI)_{block}}\right)E_m I_o \qquad (6.29)$$

The second value is the so called effective stiffness, $(EI)_{eff}$, which is the primary objective of this thesis, and is intended to estimate the ultimate load carrying capacity of cavity walls. From the curves EI versus P, it was found that the failure mode of specimen could have influence on the value $(EI)_{eff}$ corresponding to the ultimate load P_u. For a brittle failure, the EI value corresponding to the failure load P_u can be easily obtained from the curve. This failure mode occurs for a specimen with a small eccentricity and little slenderness effect. However, for a ductile failure, there is some difficulty in estimating the EI value corresponding to the ultimate load P_u. As can be observed from the curve that a small change in the value of P_u could results in a large difference in the estimated EI value. In other words, the estimated effective stiffness is sensitive to the load P_u defined in the curve. For such cases, the EI value was obtained immediately before the load reached the value of P_u.

6.4.2 Regression Analysis for the Effective Stiffness $(EI)_{eff}$

A multi-linear regression analysis was carried out for an expression of α, the effective stiffness ratio defined in Eqs. 6.23 and 6.24. A linear regression analysis was chosen because it yields simple expressions for α and because the trend analyses shown in Figs. 6.2, 6.4, 6.5 and 6.6 indicate a near linear dependence. The final expression was examined statistically using the test and analysis samples. The prediction accuracy of the expression was monitored by the standard error of the equation and of each variable. The regression analyses for α was conducted in several groups using different combinations of the variables:

1. e/t, L/t, $(EI)_{brick}/(EI)_{block}$, f'_m, e_1/e_2, E_m;
2. e/t, L/t, $(EI)_{brick}/(EI)_{block}$, e_1/e_2;
3. e/t, L/t, $(EI)_{brick}/(EI)_{block}$;
4. e/t, L/t;

Where, e/t stands for loading eccentricity, L/t for the slenderness ratio, $(EI)_{brick}/(EI)_{block}$ for the ratio of the stiffness of the two wythes, f'_m for the compressive strength of the block wythe, and E_m for the modulus of elasticity of the block wythe.

The first combination includes all the major variables which has effects on the effective stiffness. The result of the regression analysis is:

$$\alpha = 0.663 - 0.353\left(\frac{e}{t}\right) + 0.0137\left(\frac{L}{t}\right) + 0.179\left(\frac{EI_{brick}}{EI_{block}}\right) + 0.00375 f_m - 0.071\left(\frac{e_1}{e_2}\right) - 0.0002\left(\frac{E_m}{f_m}\right) \quad (6.30)$$

Equation 6.30 shows the influence of each of the variables on the stiffness of the wall. A positive sign of the coefficient of a variable indicates a proportional increase of the effective stiffness. A negative sign indicates an inversely proportional effect. As expected, the second term reflects a decrease of the effective stiffness as the loading eccentricity increases. This is obvious since the larger the eccentricity, the larger the moment, and more cracks develop in the cavity wall. The third term reflects an increase of the effective stiffness with an increase of the slenderness ratio. The reason is that there are longer uncracked segments in a longer wall than in a shorter wall. Hence, the uncracked section in a longer wall contributes more to the effective stiffness than in a shorter wall. This results seems to contradict the fact that the ultimate load capacity of the wall decreases as the slenderness ratio increases. However by observing the equation of moment magnifier, it is clear that the effect of length is counted twice in the equation of the moment amplifier, once explicitly in the equation and once implicitly in the expression of EI. Therefore, the results is believed to be reasonable. Equation 6.30 also indicates that the ratio of $(EI)_{brick}/(EI)_{block}$ has a positive effect on the effective stiffness. An increase in $(EI)_{brick}/(EI)_{block}$ means more contribution from the brick wythe to the effective stiffness of the whole cavity wall. The fifth term shows a slight increase in the effective stiffness as the strength of the block masonry increases. Here the strength f'_m represents both the variation in compressive strength and the tensile strength since the ratio between these two strengths is usually considered constant. It is understandable that higher strengths of the masonry wall delay the occurrence of cracks and are associated with an increase in the

modulus of elasticity E_m. However, this term is not a significant predictor of the response variable. The sixth term indicates a decrease of the effective stiffness as the end moment ratio changes from negative to positive within the range of -1 to 1. This indicates that the end moment ratio plays a role in the effective stiffness of the wall. With unequal end moments, less cracks will developed, therefore, larger effective stiffness is expected. The last coefficient accounts for the modulus of the elasticity of the block wythe. This variable seems redundant since the modulus of the elasticity was already considered.

It is found that the e/t, L/t , $(EI)_{brick}/(EI)_{block}$ and e_1/e_2 are the important variables in the expression of the effective stiffness of the wall. Thus, Eq. 6.30 can be simplified as:

$$\alpha = 0.641 - 0.359\left(\frac{e}{t}\right) + 0.0135\left(\frac{L}{t}\right) + 0.210\left(\frac{(EI)_{brick}}{(EI)_{block}}\right) - 0.073\left(\frac{e_1}{e_2}\right) \tag{6.31}$$

For practical design purposes, the expression for α might further simplified as a function of three or two variables as:

$$\alpha = 0.582 - 0.7\left(\frac{e}{t}\right) + 0.0151\left(\frac{L}{t}\right) + 0.821\left(\frac{(EI)_{brick}}{(EI)_{block}}\right) \tag{6.32}$$

$$\alpha = 0.65 - 0.396\left(\frac{e}{t}\right) + 0.0121\left(\frac{L}{t}\right) \tag{6.33}$$

The large change in the coefficients is due to differences in the size of the data base. For instance, the points reflecting the ratio e_1/e_2 were dropped when performing the regression analysis for Equation 6.32.

6.5 Effect of Unequal End Moments

In Section 6.4, the expression of the effective stiffness of the wall was analyzed The effective stiffness obtained from the expression is thus ready to be used in estimating moment magnifier. Recalling the pin-ended wall loaded with equal end moments, th

maximum moment of the wall is the sum of the end moment and the maximum secondary moment, and the moment magnifier as described by Eq. 6.5 is:

$$\delta = \left(\frac{1 + 0.23 \, P/P_{cr}}{1 - P/P_{cr}} \right)$$

However, in Section 6.3.2 it was also shown that for the wall with unequal end moments, the maximum moment Pe_{max} and the maximum second order moment $P\Delta_{max}$ can not be added directly. The maximum total moment is smaller than the sum of the maximum primary moment and the maximum secondary moment. i.e. $M_{max} \leq M_{omax} + P\Delta_{max}$. In order to consider the resulting beneficial effect, the equivalent moment factor C_m in the current code is intended to relate the actual case to an equal end moment case. To verify the validity of this expression for a cavity wall, the C_m value is expressed as:

$$C_m = a + b\left(\frac{M_1}{M_2} \right) \tag{6.34}$$

in which the constants a and b can be evaluated from a regression analysis. Thus, the complete expression of the moment magnifier should be:

$$\delta = \frac{C_m \left(1 + 0.23 \frac{P_u}{P_{cr}} \right)}{1 - \frac{P_u}{P_{cr}}} \tag{6.35}$$

Rearranging Eq. 6.35, C_m is isolated as:

$$C_m = \delta \left(\frac{1 - \frac{P_u}{P_{cr}}}{1 + 0.23 \frac{P_u}{P_{cr}}} \right) \tag{6.36}$$

The term inside the large brackets on the right hand side of Eq. 6.36 and the moment magnifier δ were evaluated based on the test results and the expression for the effective stiffness $(EI)_{eff}$ derived above, Eq. 6.30. The expressions for δ are obtained from Eq. 6.5 ($e_1/e_2 = 1$), Eq.6.13b ($e_1/e_2 = 0$) and Eq. 6.17b ($e_1/e_2 = -1$). These too have to be evaluated. A linear regression analysis was carried out using these values for Cm to obtain the constants a and b in Eq.6. 34. This resulted in:

$$C_m = 0.647 + 0.401\frac{M_1}{M_2} \tag{6.37}$$

Equation (6.37) is very close to that adopted by the code, Eq. 6.20a. The code expression is, thus, recommended herein in the form:

$$1.0 \geq C_m = 0.6 + 0.4\frac{M_1}{M_2} \geq 0.4 \tag{6.38}$$

The lower limit on $C_m \geq 0.4$ was initially used by steel design codes to prevent lateral torsional buckling. For a masonry cavity wall, this mode is not possible. This limit may, therefore, appear to be conservative. However, to account on the uncertainties of the behaviour of masonry cavity walls, this limitation should be kept in the design code.

6.6 Other Considerations

The above discussion was based on the assumption of a short-time loading condition. The effect of creep under sustained load has not been considered. It is believed that the effective stiffness of the wall will be reduced as a result of the effect of sustained load and creep. The long-term behaviour of a cavity wall is left for future research. At present, the S304.1 code accounts for long term effects using a modification factor $(1+0.5\beta_d)$ so that:

$$(EI)_{eff} = \frac{\alpha}{1+0.5\beta_d} E_m I_o \tag{6.39}$$

in which, β_d is the ratio of factored dead load moment to total factored moment. The validity of this expression needs to be verified by future research.

In design practice, consideration should be given to the variations in the effective stiffness. The resistance factor ϕ_e = 0.65 given by the Code S304.1 should be used whenever the effective stiffness is to be used in the ultimate limit states design.

Throughout this investigation, the effective height factor K is taken as 1.0 which is suitable for the end constraints as described in the tests and analyses. For design purposes, the determination of the height factor should follow the Code S304.1 Clause 11.1.2.1.

6.7 Proposed Design Equations for Slender Masonry Cavity Walls

For the purpose of deflection calculations at specified loads, the effective moment of inertia of the cavity walls can be estimated by equation:

$$EI = \left(0.75 + 0.3\frac{e}{t} + 0.0075\frac{L}{t} + 1.35\frac{(EI)_{brick}}{(EI)_{block}}\right)E_m I_o \qquad (6.40)$$

For the ultimate limit state, the masonry cavity wall should be designed to resist the factored load P_f and the magnified moment M_{tot}. The magnified moment is obtained following the equations:

$$M_{tot} = \delta M_p \qquad (6.41)$$

in which, M_p is the primary moment applied at the ends of the block wythe and δ is the moment magnifier:

$$\delta = \frac{C_m}{1 - \frac{P_f}{P_{cr}}} \qquad (6.42)$$

The factor C_m should be obtained as a function of the end moment ratio $\frac{M_1}{M_2}$ as:

$$1.0 \geq C_m = 0.6 + 0.4\frac{M_1}{M_2} \geq 0.4 \tag{6.43}$$

P_{cr} is the Euler buckling load:

$$P_{cr} = \frac{\pi^2 \phi_e (EI)_{eff}}{(kL)^2} \tag{6.44}$$

in which, ϕ_e is the resistance factor, $\phi_e = 0.65$. k is the effective length factor. For the cavity wall as described, k should be taken as 1.0. $(EI)_{eff}$ is the effective stiffness of the wall. For cavity wall $(EI)_{eff}$ should be determined by the proposed equation:

$$(EI)_{eff} = \frac{1}{1+\beta_d}\left(0.6 - 0.7\left(\frac{e}{t}\right) + 0.015\left(\frac{L}{t}\right) + 0.82\left(\frac{(EI)_{brick}}{(EI)_{block}}\right)\right)E_m I_{bl} \tag{6.45}$$

A design example is provided in Appendix A.

6.8 Comparison of Proposed Design Method with Tests and Analyses

It is desirable to check the proposed design formula against the tests and analyses. The $(EI)_{eff}$ value calculated by the proposed formula were examined with the values obtained by the tests and analyses. In the comparison, the resistance factor is taken as 1.0, i.e. $\phi_e = 1.0$. With 95% confidence limit, the mean of $(EI_{eff})_{comp} / (EI_{eff})_{analy}$ is 1.016, the standard error is 0.0241 and the standard deviation is 0.198. The magnified moments calculated by the proposed equations were checked against the values obtained theoretically using the $(EI)_{eff}$ value obtained from tests or analyses. In the calculation $\phi_e = 1.0$, and the limitation of $C_m \geq 0.4$ was not considered. With 95% confidence limit, the mean is 0.986, the standard deviation is 0.1297, and the standard error is 0.0158.

Figure 6.9 (a) to 6.9(e) show a series of comparisons of the proposed design approach to the test results and the current code. Figure 6.9(a) shows the comparison of proposed design approach with the test results of this study and the results from Goyal's tests. The figure shows that the proposed design approach agrees well with the test

results. When the resistance factor ϕ_e is introduced, there is a significant safety margin as shown in Figure 6.9(b). Figure 6.9(c) shows the comparison of the proposed approach to the tests and the current code. Where, the capacity of the wall calculated by the current code was computed without considering the structural performance of the brick wythe. It can be observed that the current code is too conservative and may not be even applicable when the ratio of e_1/e_2 is negative. Figure 6.9(d) and 6.9(e) show the comparison of the proposed approach to the tests when $e_1/e_2 = 0$, and -1. Again a large safety margin is observed when the resistance factor is introduced.

6.9 Summary

In this chapter the analysis results of the cavity walls were further discussed. The theoretical expressions of the moment magnifier were derived. Based on the results of the tests and analyses, expressions for the effective stiffness were evaluated by means of linear regression analyses. The final proposed expression for the effective stiffness is easy to use in the design of a cavity wall. The expression was shown to be of adequate accuracy.

Table 6.1 Properties, Loading Conditions and the Stiffness of the Specimens

1	2	3	4	5	6	7	8	9	10	11	12	13	14
Series	Specimen	f_m' block MPa	α block	b_1 brick mm	b_2 block mm	EI_{brk}/EI_{blo}	L/t	C mm	e/t	a or t	e_1/e_2	$(EI)_{spec}$ $\times 10^{12}$ N·mm^2	$(EI)_{eff}$ $\times 10^{12}$ N·mm^2
1	WS1	19.3	721	90	190	0.0524	27.8	75	0	N/A	N/A	N/A	N/A
	WS2	19.3	721	90	190	0.0524	27.8	75	1/6	a	1	8.75	7.76
	WS3	19.3	721	90	190	0.0524	27.8	75	P = 0	a	1	N/A	N/A
	WS4	19.3	721	90	190	0.0524	27.8	75	1/12	a	1	8.07	7.82
	WS5	19.3	721	90	190	0.0524	27.8	75	1/3	a	1	9.25	6.83
	WS6	19.3	721	90	190	0.0524	27.8	75	1/2	a	1	9.56	5.01
2	WSB1	19.3	721	90	190	0.0524	27.8	75	1/3	a	1	9.25	6.83
	WSB2	19.3	721	90	140	0.128	27.8	75	1/3	a	1	4.25	2.85

Table 6.1 (cont'd)

Series	Specimen	f_m' block MPa	α block	b_1 brick mm	b_2 block mm	EI_{brk}/EI_{blo}	L/t	C mm	e/t	a or t	e_1/e_2	$(EI)_{spec}$ $\times 10^{12}$ N·mm^2	$(EI)_{eff}$ $\times 10^{12}$ N·mm^2
2	WSB3	19.3	721	90	240	0.0301	27.8	75	1/3	a	1	16.95	13.0
	WSB4	19.3	721	90	190	0.0524	18.3	75	1/3	a	1	8.38	4.86
	WSB5	19.3	721	90	140	0.128	18.3	75	1/3	a	1	3.28	1.45
	WSB6	19.3	721	90	240	0.0301	18.3	75	1/3	a	1	16.23	11.90
	WSB7	19.3	721	90	190	0.0524	37.3	75	1/3	a	1	9.94	7.36
	WSB8	19.3	721	90	140	0.128	37.3	75	1/3	a	1	4.63	2.89
	WSB9	19.3	721	90	240	0.0301	37.3	75	1/3	a	1	17.52	13.5
3	WSE1	19.3	721	90	190	0.0524	27.8	75	1/3	a	1	9.25	6.83
	WSE2	19.3	850	90	190	0.0469	27.8	75	1/3	a	1	11.07	7.84
	WSE3	19.3	1000	90	190	0.0399	27.8	75	1/3	a	1	12.34	8.19
	WSE4	19.3	721	90	190	0.0524	18.3	75	1/3	a	1	8.38	4.86
	WSE5	19.3	850	90	190	0.0469	18.3	75	1/3	a	1	9.45	5.51
	WSE6	19.3	1000	90	190	0.0399	18.3	75	1/3	a	1	11.09	6.45
	WSE7	19.3	721	90	190	0.0524	37.3	75	1/3	a	1	9.94	7.36

Table 6.1 (cont'd)

Series	Specimen	f_m' block MPa	α block	b_1 brick mm	b_2 block mm	EI_{brk}/EI_{blo}	L/t	C mm	e/t	a or t	e_1/e_2	$(EI)_{spec}$ $\times 10^{12}$ N·mm^2	$(EI)_{eff}$ $\times 10^{12}$ N·mm^2
3	WSE8	19.3	850	90	190	0.0469	37.3	75	1/3	a	1	11.3	8.81
	WSE9	19.3	1000	90	190	0.0399	37.3	75	1/3	a	1	12.97	9.79
4	WSF1	10.0	1399	90	190	0.0524	27.8	75	1/3	a	1	9.30	6.24
	WSF2	19.3	721	90	190	0.0524	27.8	75	1/3	a	1	9.25	6.83
	WSF3	25.0	560	90	190	0.0524	27.8	75	1/3	a	1	9.30	7.11
	WSF4	10.0	1399	90	190	0.0524	18.3	75	1/3	a	1	8.68	5.55
	WSF5	19.3	721	90	190	0.0524	18.3	75	1/3	a	1	8.38	5.87
	WSF6	25.0	560	90	190	0.0524	18.3	75	1/3	a	1	8.42	6.01
	WSF7	10.0	1399	90	190	0.0524	37.3	75	1/3	a	1	9.92	7.15
	WSF8	19.3	721	90	190	0.0524	37.3	75	1/3	a	1	9.94	7.36
	WSF9	25.0	560	90	190	0.0524	37.3	75	1/3	a	1	9.81	7.64
5	WSL1	19.3	721	90	190	0.0524	37.3	75	0	N/A	N/A	N/A	N/A
	WSL2	19.3	721	90	190	0.0524	37.3	75	1/12	a	1	8.28	8.14

Table 6.1 (cont'd)

Series	Specimen	f_m' block MPa	α block	b_1 brick mm	b_2 block mm	EI_{brk}/EI_{blo}	L/t	C mm	e/t	a or t	e_1/e_2	$(EI)_{spec}$ $\times 10^{12}$ N·mm^2	$(EI)_{eff}$ $\times 10^{12}$ N·mm^2
5	WSL3	19.3	721	90	190	0.0524	37.3	75	1/3	a	1	9.94	7.36
	WSL4	19.3	721	90	190	0.0524	37.3	75	1/2	a	1	10.12	6.09
	WSL5	19.3	721	90	190	0.0524	37.3	75	P = 0	a	1	N/A	N/A
	WSL6	19.3	721	90	190	0.0524	37.3	75	1/6	a	1	8.88	8.0
6	WSS1	19.3	721	90	190	0.0524	18.3	75	1/3	a	1	8.38	4.42
	WSS2	19.3	721	90	190	0.0524	18.3	75	1/6	a	1	8.42	5.82
	WSS3	19.3	721	90	190	0.0524	18.3	75	1/2	a	1	8.02	2.20
	WSS4	19.3	721	90	190	0.0524	18.3	75	P = 0	a	1	N / A	N / A
	WSS5	19.3	721	90	190	0.0524	18.3	75	0	N / A	N / A	N / A	N / A
	WSS6	19.3	721	90	190	0.0524	18.3	75	1/12	a	1	7.98	7.21
	WSM1	19.3	721	90	190	0.0524	27.8	75	1/3	a	0	8.37	7.27
	WSM2	19.3	721	90	190	0.0524	27.8	75	1/12	a	0	7.10	7.44
	WSM3	19.3	721	90	190	0.0524	27.8	75	1/2	a	0	8.27	5.84

Table 6.1 (cont'd)

Series	Specimen	f_m' block MPa	α block	b_1 brick mm	b_2 block mm	EI_{brk}/EI_{blo}	L/t	C mm	e/t	a or t	e_1/e_2	$(EI)_{spec}$ $\times 10^{12}$ N·mm^2	$(EI)_{eff}$ $\times 10^{12}$ N·mm^2
7	WSM4	19.3	721	90	190	0.0524	27.8	75	1/6	a	0	7.95	7.27
	WSM5	19.3	721	90	190	0.0524	27.8	75	P = 0	a	0	N/A	N/A
	WSM6	19.3	721	90	190	0.0524	18.3	75	1/3	a	0	8.01	6.[illegible]
	WSM7	19.3	721	90	190	0.0524	18.3	75	1/2	a	0	7.31	4.63
	WSM8	19.3	721	90	190	0.0524	18.3	75	1/12	a	0	6.82	6.32
	WSM9	19.3	721	90	190	0.0524	18.3	75	1/6	a	0	7.67	5.57
	WSM10	19.3	721	90	190	0.0524	18.3	75	P = 0	a	0	N/A	N/A
	WSM11	19.3	721	90	190	0.0524	37.3	75	1/3	a	0	8.82	7.55
	WSM12	19.3	721	90	190	0.0524	37.3	75	1/12	a	0	7.0	8.22
	WSM13	19.3	721	90	190	0.0524	37.3	75	1/2	a	0	9.02	6.50
	WSM14	19.3	721	90	190	0.0524	37.3	75	1/6	a	0	8.17	8.03
	WSM15	19.3	721	90	190	0.0524	37.3	75	P = 0	a	0	N/A	N/A
8	WSM16	19.3	721	90	190	0.0524	27.8	75	1/12	N/A	-1	14.8	8.01
	WSM17	19.3	721	90	190	0.0524	27.8	75	1/2	N/A	-1	7.95	5.16

Table 6.1 (cont'd)

Series	Specimen	f_m' block MPa	α block	b_1 brick mm	b_2 block mm	EI_{brk}/EI_{blo}	L/t	C mm	e/t	a or t	e_1/e_2	$(EI)_{spec}$ $\times 10^{12}$ N·mm^2	$(EI)_{eff}$ $\times 10^{12}$ N·mm^2
8	WSM18	19.3	721	90	190	0.0524	27.8	75	1/6	N/A	-1	8.67	6.41
	WSM19	19.3	721	90	190	0.0524	27.8	75	P=0	N/A	N/A	N/A	N/A
	WSM20	19.3	721	90	190	0.0524	27.8	75	1/3	N/A	-1	8.70	7.44
	WSM21	19.3	721	90	190	0.0524	18.3	75	1/12	N/A	-1	8.55	7.36
	WSM22	19.3	721	90	190	0.0524	18.3	75	1/2	N/A	-1	7.90	6.32
	WSM23	19.3	721	90	190	0.0524	18.3	75	1/6	N/A	-1	8.23	7.32
	WSM24	19.3	721	90	190	0.0524	18.3	75	P=0	N/A	N/A	N/A	N/A
	WSM25	19.3	721	90	190	0.0524	18.3	75	1/3	N/A	-1	8.33	7.60
	WSM26	19.3	721	90	190	0.0524	37.3	75	1/12	N/A	-1	13.62	10.7
	WSM27	19.3	721	90	190	0.0524	37.3	75	1/2	N/A	-1	9.99	4.5
	WSM28	19.3	721	90	190	0.0524	37.3	75	1/6	N/A	-1	10.27	8.02
	WSM29	19.3	721	90	190	0.0524	37.3	75	P=0	N/A	N/A	N/A	N/A
	WSM30	19.3	721	90	190	0.0524	37.3	75	1/3	N/A	-1	9.95	7.98

Table 6.1 (cont'd)

Series	Specimen	f_m' block MPa	α block	b_1 brick mm	b_2 block mm	EI_{brf}/EI_{blo}	L/t	C mm	e/t	a or t	e_1/e_2	$(EI)_{spec}$ $\times 10^{12}$ N·mm^2	$(EI)_{eff}$ $\times 10^{12}$ N·mm^2
9	WA11	19.3	721	90	190	0.0524	27.8	75	1/3	t	1	10.14	6.94
	WA7	19.3	721	90	190	0.0524	27.8	100	1/3	t	1	9.47	6.16
	WA12	19.3	721	90	190	0.0524	27.8	100	1/3	a	1	8.59	6.25
	WA16	19.3	721	90	190	0.0524	27.8	100	1/2	t	1	9.71	4.46
	WA17	19.3	721	90	190	0.0524	27.8	100	1/2	a	1	7.74	4.25
	WS101	19.3	721	90	140	0.128	37.8	75	1/2.2	a	1	4.46	2.67
	WS102	19.3	721	90	140	0.128	37.8	75	1/2.2	t	1	5.01	2.77
	WS103	19.3	721	90	240	0.0301	22.0	75	1/3.9	a	1	16.38	12.4
	WS104	19.3	721	90	240	0.0301	22.0	75	1/3.9	t	1	17.3	12.5
	WS107	19.3	721	90	240	0.0301	22.0	75	1/2.7	a	1	15.53	9.02
	WS108	19.3	721	90	240	0.0301	22.0	75	1/2.7	t	1	16.23	9.33
	WS204	19.3	721	90	190	0.0524	27.8	100	1/3	a	0	8.03	6.84
	WS205	19.3	721	90	190	0.0524	27.8	100	1/3	t	0	9.44	7.24
	WS207	19.3	721	90	190	0.0524	27.8	75	1/2	t	0	10.35	4.82

Table 6.1 (cont'd)

Series	Specimen	f_m' block MPa	α block	b_1 brick mm	b_2 block mm	EI_{bri}/EI_{blo}	L/t	C mm	e/t	a or t	e_1/e_2	$(EI)_{spec}$ $\times 10^{12}$ N·mm^2	$(EI)_{eff}$ $\times 10^{12}$ N·mm^2
9	WS208	19.3	721	90	190	0.0524	27.8	100	1/2	a	0	7.88	4.70
	WS209	19.3	721	90	190	0.0524	27.8	100	1/2	t	0	9.89	4.92

Notes:

Column 1: Series number;
Column 2: Name of the specimens;
Column 3: f_m' = Compressive strength of the block assemblage;
Column 4: $\alpha = E_m / f_m'$, Coefficient between the compressive strength and the modulus of elasticity of the block assemblage;
Column 5: b_1 = Thickness of the brick wythe;
Column 6: b_2 = Thickness of the block wythe;
Column 7: EI_{bri}/EI_{blo} = Ratio of $(EI)_{brick}/(EI)_{block}$;
Column 8: L/t = Slenderness ratios;
Column 9: C = Cavity width;
Column 10: e/t = Ratios of the loading eccentricity to the thickness of the walls;
Column 11: a or t = The direction of the eccentricity was away (a) or towards (t) the brick wythe;
Column 12: e_1 / e_2 = Ratios of the eccentricities at the top and the bottom ends of the walls;
Column 13: $(EI)_{spec}$ = Stiffness for the purpose of deflection calculation at specified load;
Column 14: $(EI)_{eff}$ = Effective stiffness of the wall.

Specimens WS3, WSE1, WSB1and WSF2 are identical; Specimens WSB4,WSE4 , WSF5 and WSS1 are identical; Specimens WSB7, WSE7, WSF8 and WSL8 are identical.

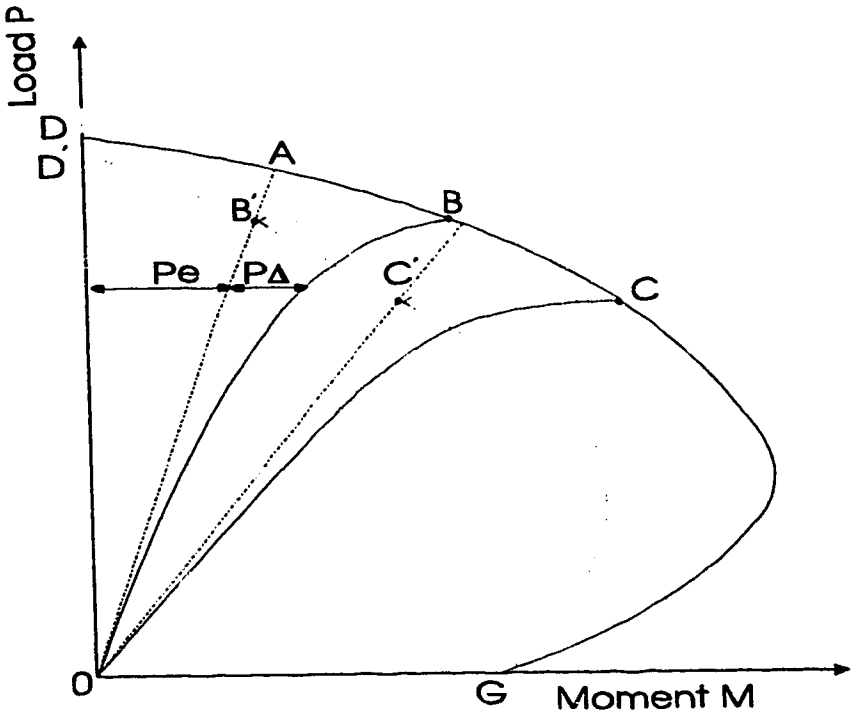

Figure 6.1 Interaction diagram

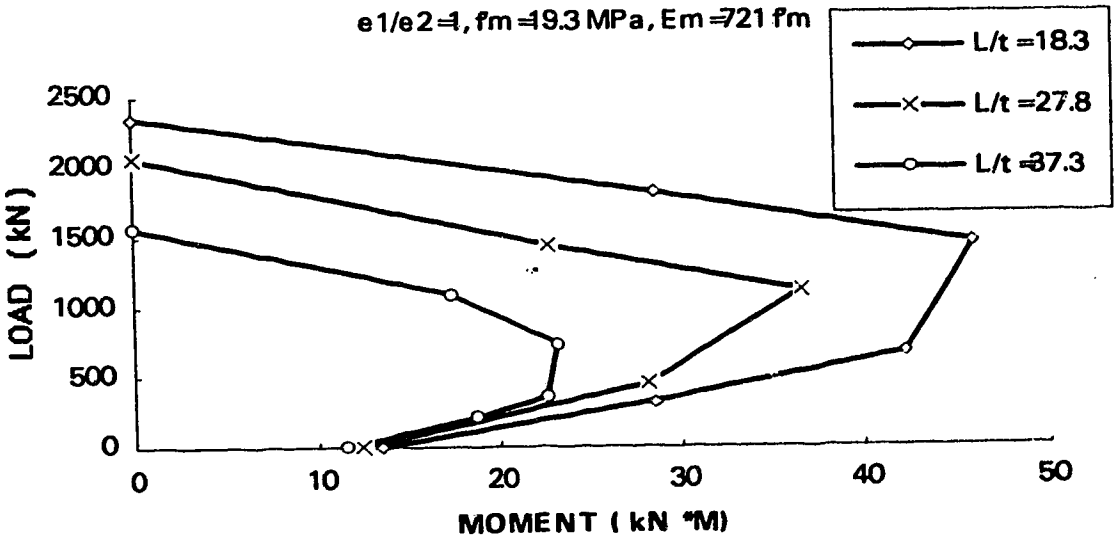

Figure 6.2 (a) Slender wall interaction diagram

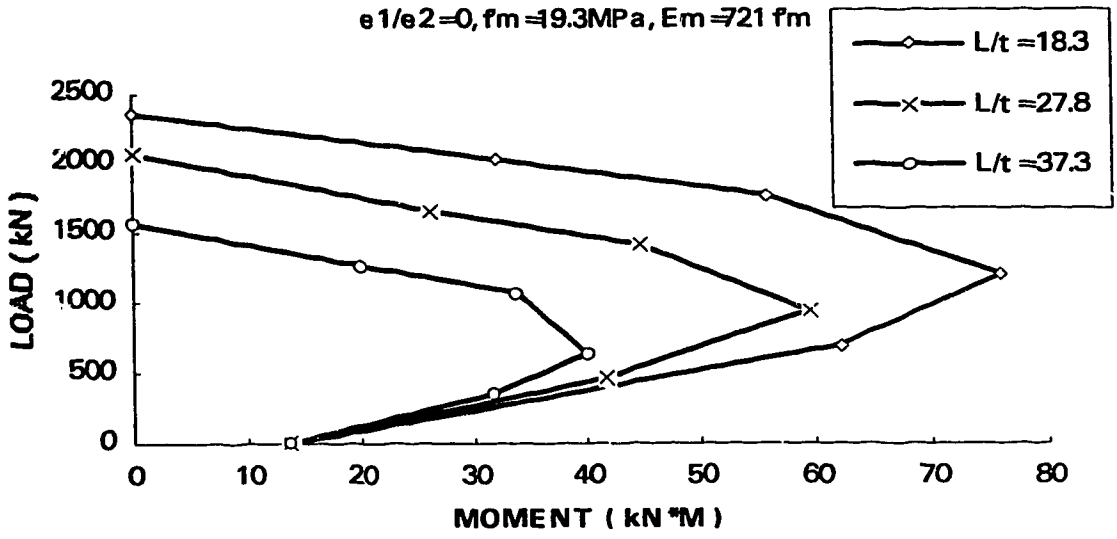

Figure 6.2 (b) Slender wall interaction diagram

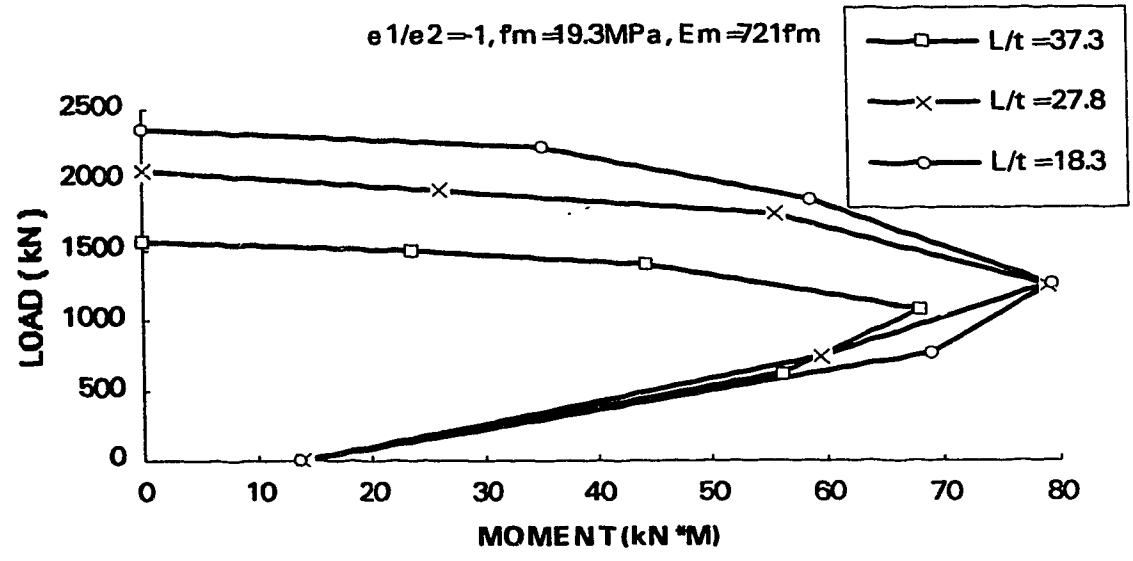

Figure 6.2 (c) Slender wall interaction diagram

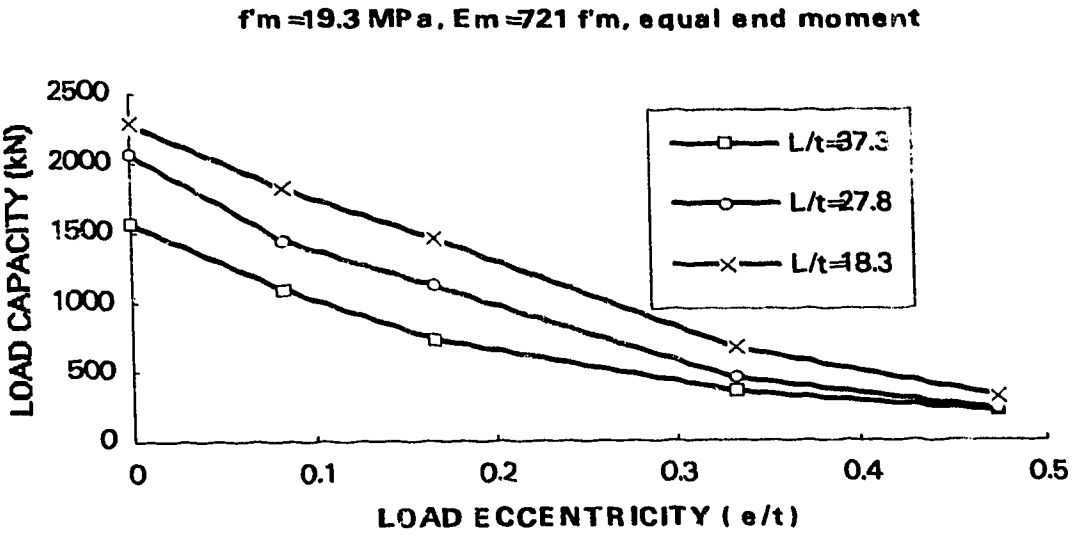

Figure 6.3 Effect of loading eccentricity

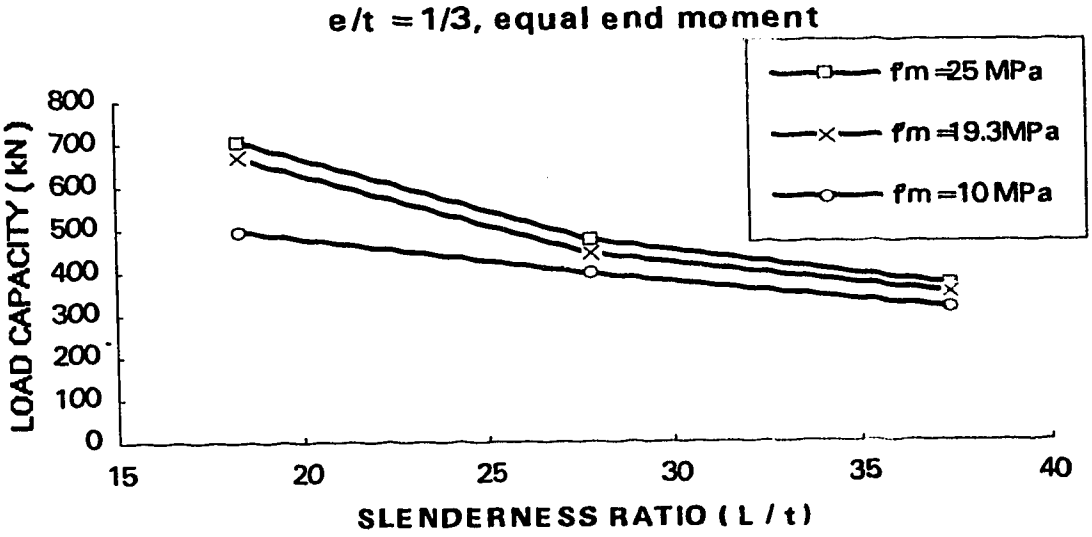

Figure 6.4 Effect of block strength

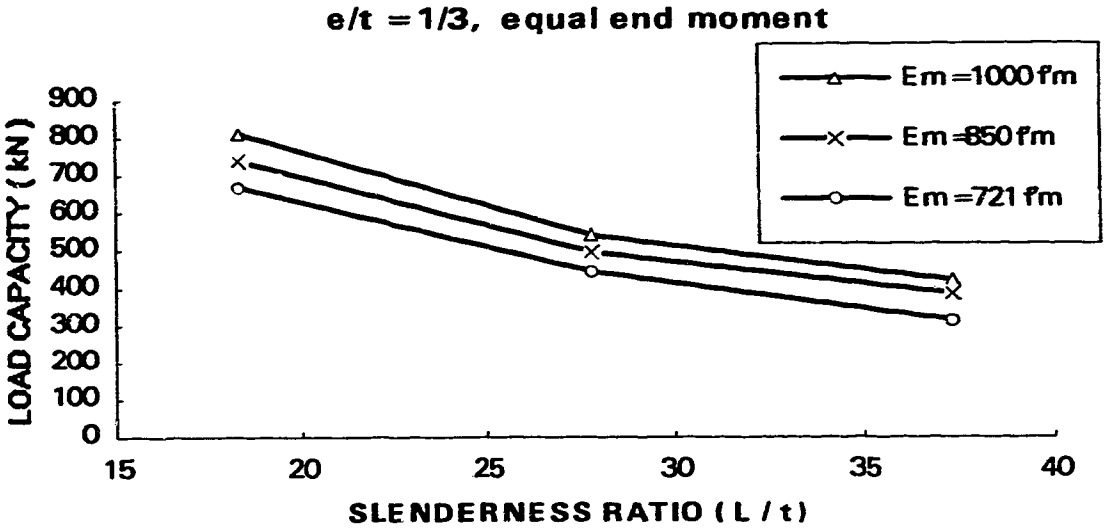

Figure 6.5 Effect of modulus of elasticity

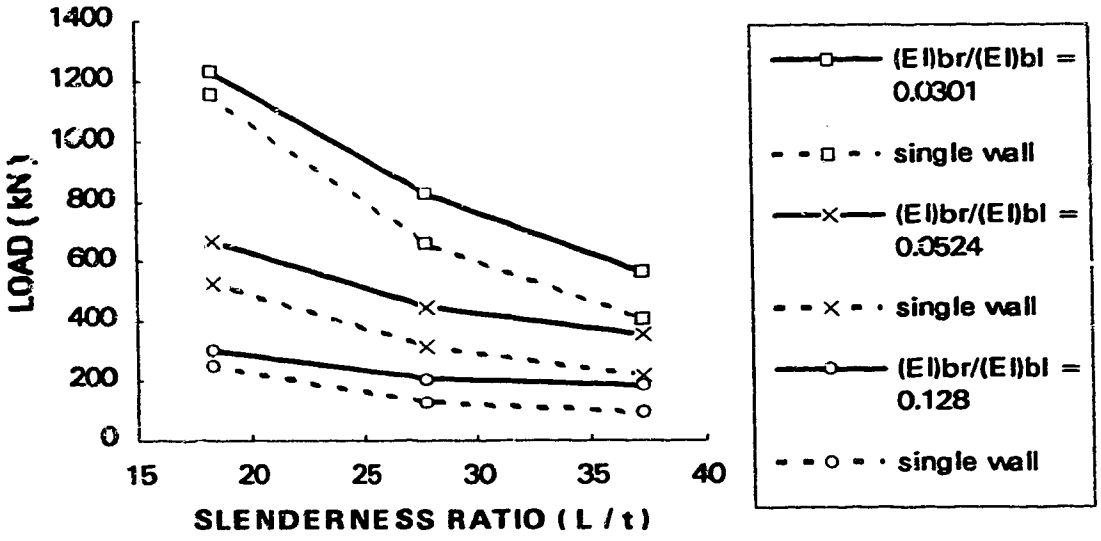

Figure 6.6 Effect of the ratio of $(EI)_{brick}/(EI)_{block}$

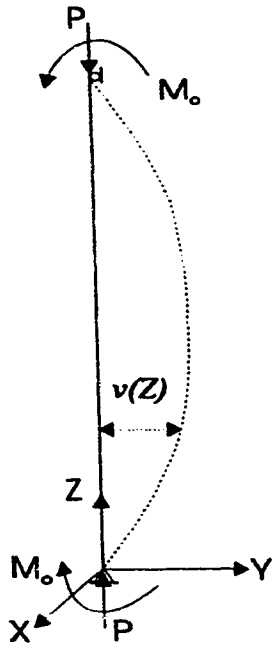

(a) Single curvature

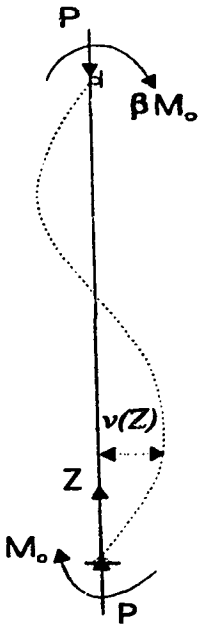

(b) Double curvature

Figure 6.7 Simplified schematic of the cavity walls

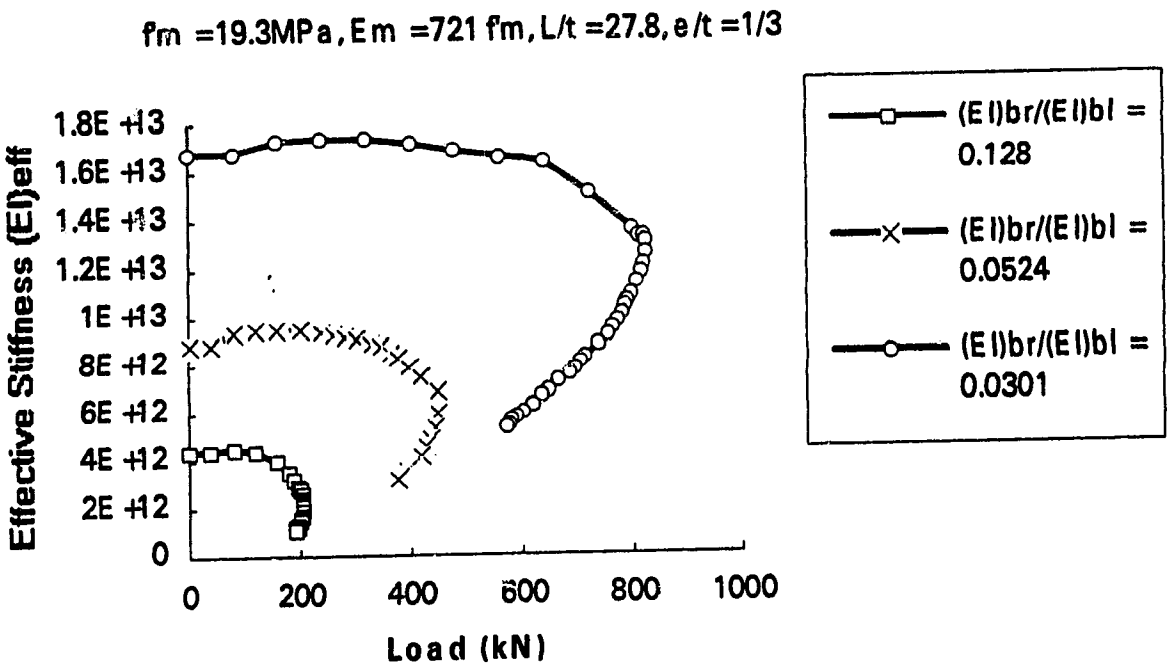

Figure 6.8 (a) Stiffness EI vs. load P curves of specimen WSB1, WSB2 and WSB3

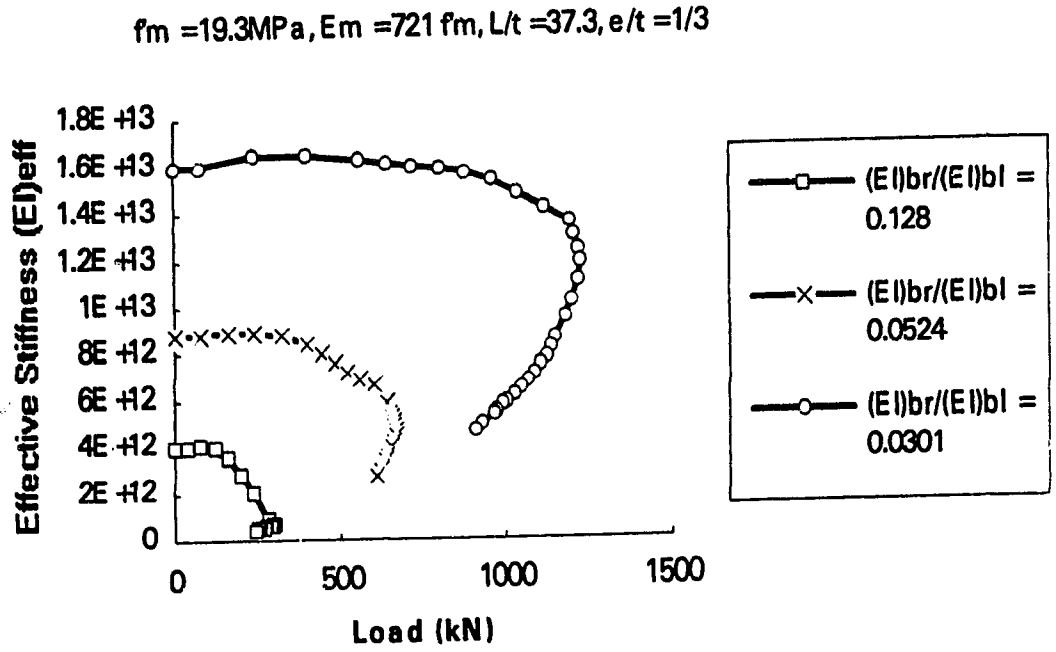

Figure 6.8 (b) Stiffness EI vs. load P curves of specimen WSB4, WSB5 and WSB6

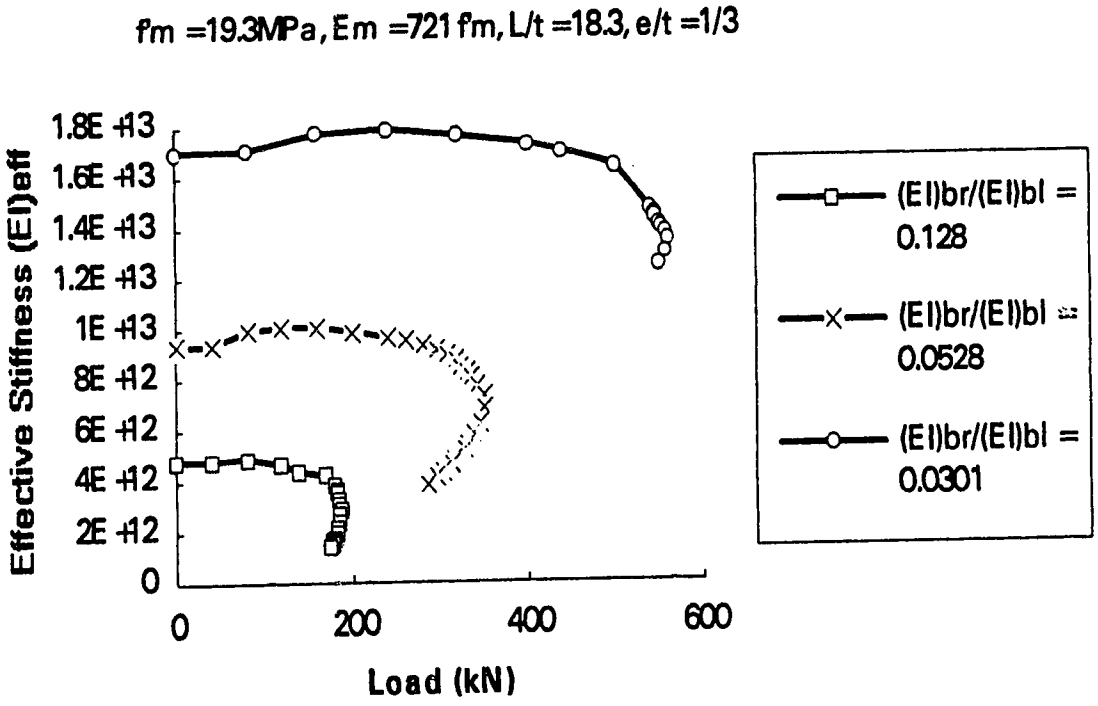

Figure 6.8 (c) Stiffness EI vs. load P curves of specimen WSB7, WSB8 and WSB9

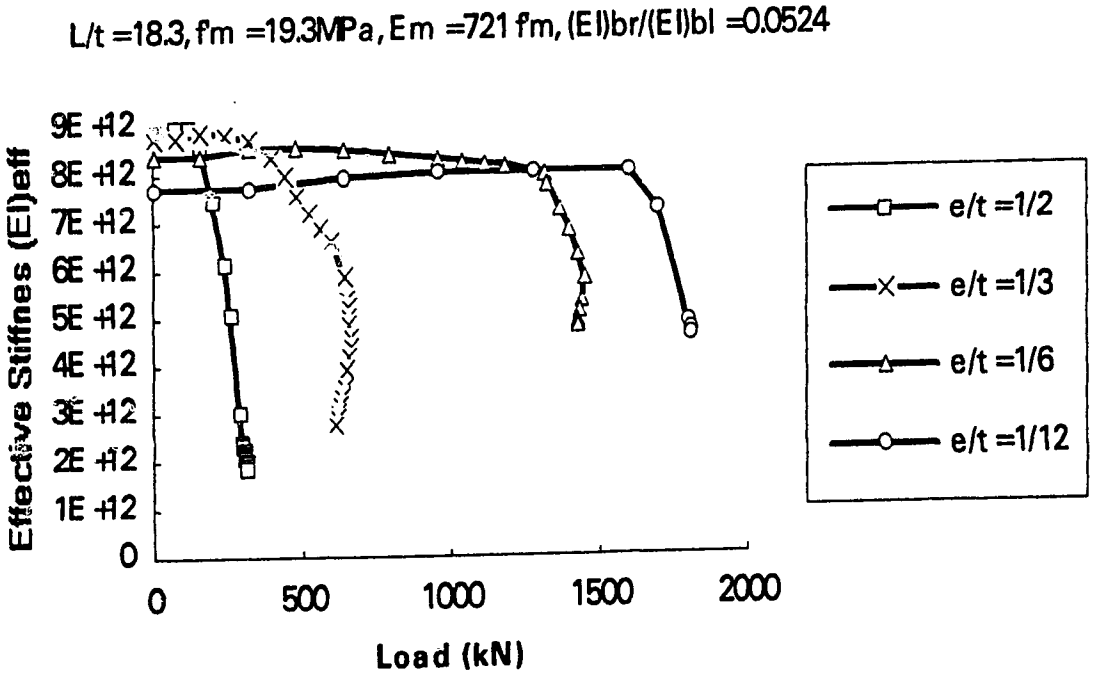

Figure 6.8 (d) EI vs. load curves of specimen WS2, WS4, WS5 and WS6

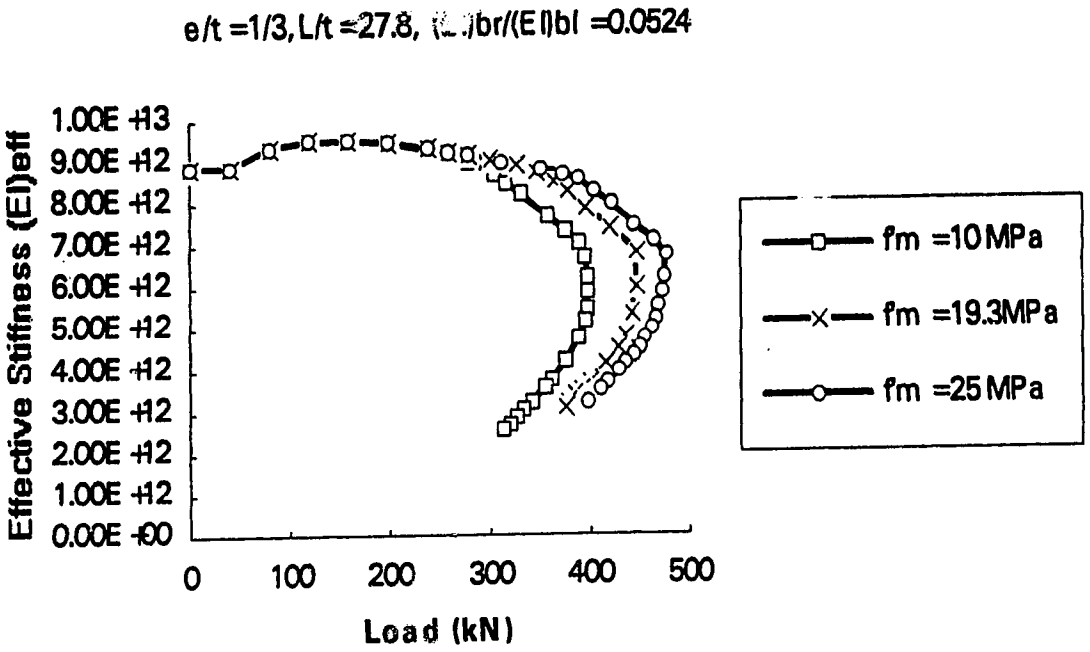

Figure 6.8 (e) EI vs. load curves of specimen WSF1, WSF2, and WSF3

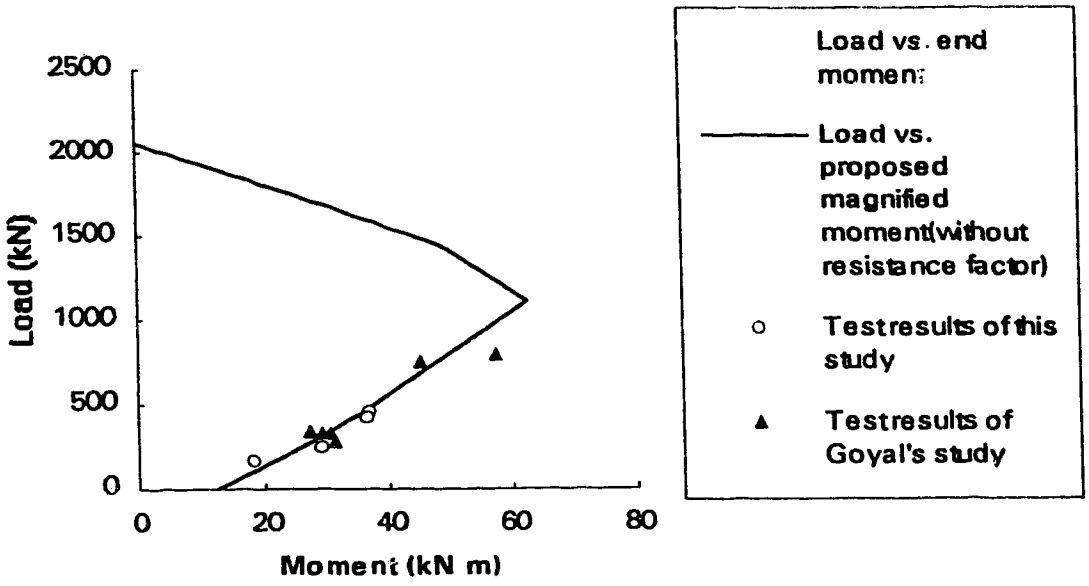

Figure 6.9(a) Comparison of proposed approach($\phi_e = 1.0$) to test results

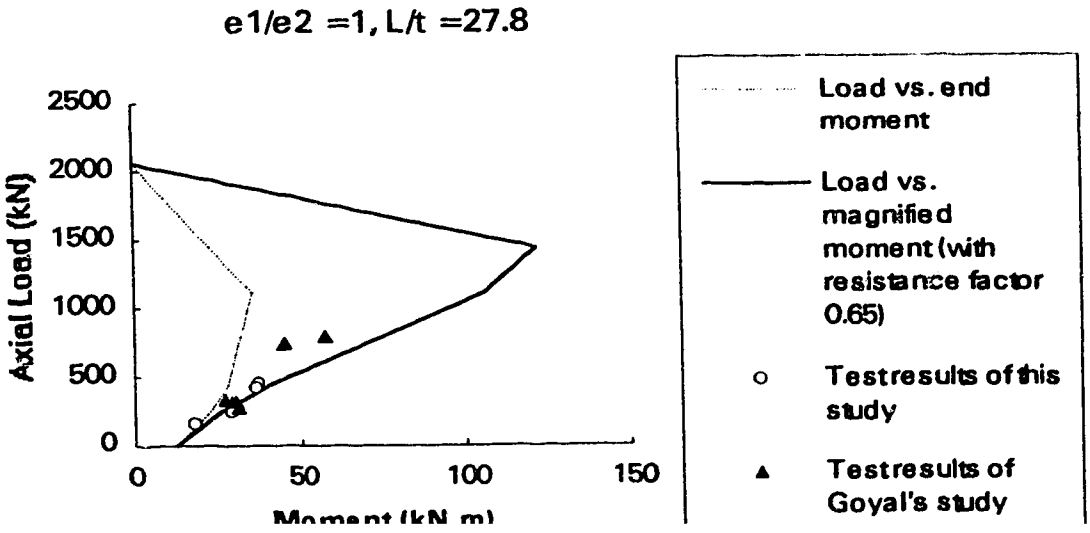

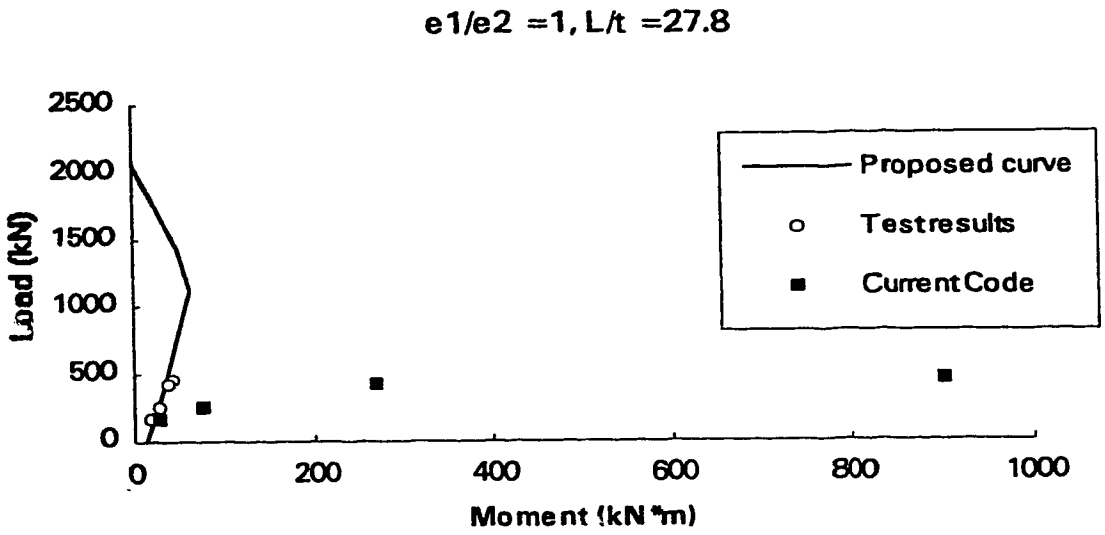

Figure 6.9(c) Comparison of proposed approach ($\phi_c = 0.65$) to the current Code CAN3-304.1-94 and test results

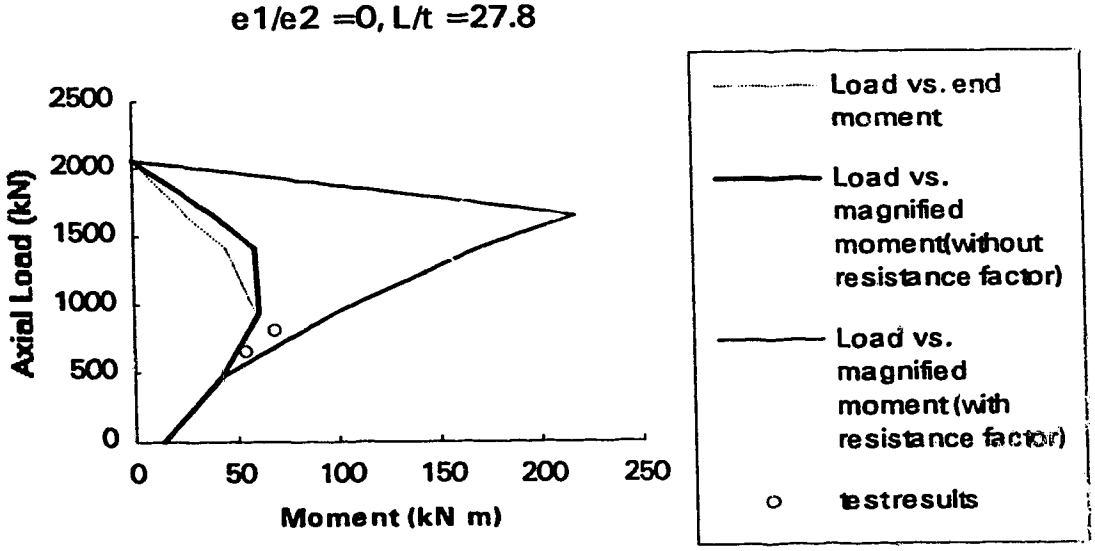

Figure 6.9(d) Comparison of proposed approach to test results

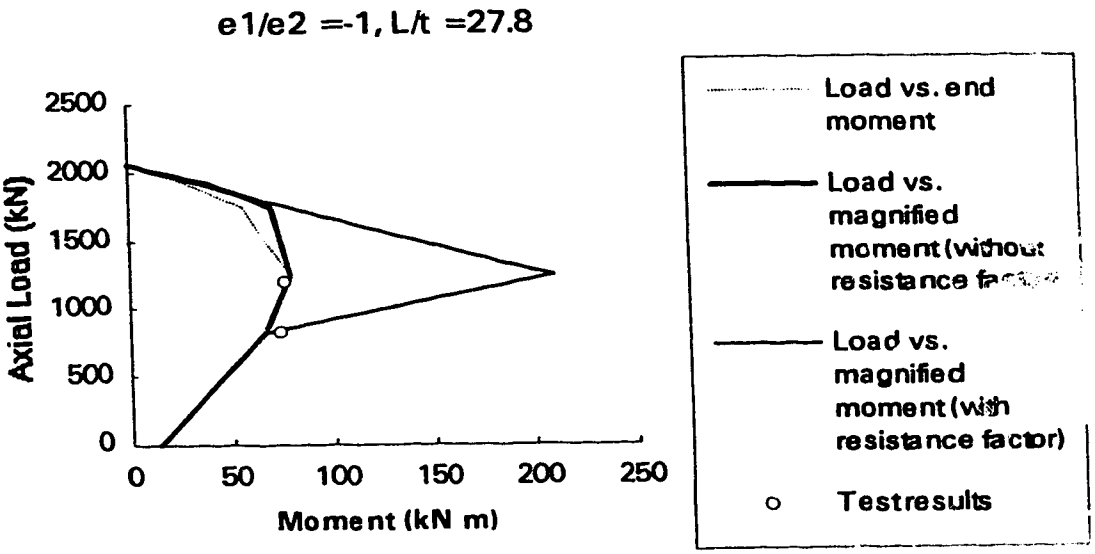

Figure 6.9(e) Comparison of proposed approach to test results

CHAPTER SEVEN

SUMMARY AND CONCLUSIONS

7.1 Summary

In this study, full scale wall tests have been carried out on shear connected slender masonry cavity walls. The behaviour of the wall at various loading stages has been observed. The experimental investigation was focused on the effects of the loading eccentricities including the magnitude, the direction, as well as the ratio of the eccentricities at the two ends. The full scale wall tests were simulated by a finite element analysis model which was shown to be of adequate accuracy in predicting the behaviour of a cavity wall. The data base established by the experimental program was then extended by means of the numerical analyses. The experimental and numerical analysis results have been used in a regression analysis through which the equations for the design of shear connected slender masonry cavity walls have been derived and proposed.

The experimental program has also been conducted on shear connectors under tension, compression, shear and bending loads. The test results have provided useful information regarding the capacity and the stiffness of the connectors under various loading conditions. The cross-sectional properties of the connectors have been evaluated from the test results. The stiffness matrices of a short beam model for both the 75 mm and 100 mm connectors have been evaluated.

7.2 Conclusions

According to the experimental and analytical investigation, the following conclusions are arrived at:

(1) Owing to the structural contribution of the brick wythe, the capacity and the stiffness of the shear connected slender masonry cavity wall have been increased considerably when subjected to the vertical eccentric loads. The increase in the capacity and the stiffness is in proportion to the ratio of the relative stiffness of the brick to block wythe. The increase in the capacity and the stiffness is also affected by the slenderness ratio of the wall; the slender walls show better improvement than the shorter walls.

(2) The failure of the slender masonry cavity walls was detected as one of three modes: the inelastic instability failure of the wall due to large deformation caused by the initial moments, the vertical load and the second order effects; the material compression failure pattern and the failure of the shear connectors. A material compression failure pattern occurs when the wall is loaded with a small eccentricity or the ratio of the eccentricity at the two ends of the wall causes the wall to deflect in double curvature. The failure mode caused by the failure of the shear connectors could be prevented by specifying a closer spacing between the connectors.

(3) The response of the shear connected masonry cavity wall subjected to vertical eccentric load is a function of the loading eccentricity, the slenderness ratio, the ratio of the end moments, the material properties of the block wythe, the cavity width, the properties of the connectors and their arrangement, etc. Among them, the slenderness ratio, the loading eccentricity, the ratio of the end moments and the

ratio of the stiffness of the two wythes are the most significant factors affecting the strength and the stiffness of the shear connected cavity walls:

- Increasing the slenderness ratio reduces the load carrying capacity. The slenderness effect becomes less significant as the ratio of the end moments changes from positive to negative within the range of +1 to -1, single curvature to double curvature.
- Increasing the loading eccentricity reduces the capacity of the wall considerably. Also the capacity of the wall decreases while the ductility increases, when the ratio of the end eccentricities changes from -1 to +1.

(4) The influence of the cavity width on the wall stiffness and the load-carrying capacity was counteracted by the stiffness of the shear connector. For a large cavity width spanned the shear connector commonly used in practice, there is no significant change in the load-carrying capacity and the stiffness of the wall.

7.3 Recommendations

(1) The design procedure proposed in Chapter 6 is recommended for the design of shear connected cavity walls not covered by CAN3-304.1-94.

(2) Further research should be performed to examine the long-time behaviour of the cavity walls and to evaluate the effects of sustained loads.

(3) The examination of the end effects on the behaviour of the cavity walls and the evaluation of the effective length factor should be performed.

(4) Further experimental and analytical research is recommended to extend the database and to develop rational safety factors that are suitable for limit state design.

REFERENCES

Arya, S.K. and Hegemier, G.A.(1982), "Finite Element Method for Interface Problems", *Journal of Structures Division, ASCE.* Vol. 108, No. ST2, February 1982, pp.327-342

Atkinson, R.H. and Yan, G.G. , (1990)," Results of a Statistical Study of Masonry Deformability ", *The Masonry Society Journal 9*, No.1.

Austin, W.J., (1961), " Strength and Design of Metal Beam-Columns", *Proceedings ASCE, Journal of the Structural Division*, Vol. 87, No.ST4, April 1961, pp.1-34.

Balachandran, K., (1974), " An Investigation of the Strength of Concrete masonry Shear Wall Structures", Ph.D. Thesis, University of Florida, 1974

CSA Standard, (1984), " CAN3-S304-84 Masonry Design for Buildings", Canadian Standard Association, Ontario, Canada

CSA Standard, (1994), " CAN3-S304.1-94 Masonry Design for Buildings (Limit States Design)", Canadian Standards Association, Ontario, Canada.

Drysdale R.G. and Hamid, A.A., (1979), " Behavior of Concrete Block Masonry under Axial Compression", *ACI Journal*, Vol. 76, No.6, 1979, pp. 707-721.

Drysdale R.G. and Hamid, A.A., (1983), " Capacity of Concrete Block Masonry Prisms Under Eccentric Compressive Loading", *ACI Journal*, Vol. 80, No. 11, March-April, 1983, pp.102-108.

Drysdale R.G. and Hamid, A.A.,(1982), " Effect of Eccentricity on the Compressive Strength of Brickwork", *Journal of the British Ceramic Society*, No. 30. September 1982, pp. 140-149.

Drysdale, R.G. and Essawy, A., (1988), " Out-of-Plane Bending of Concrete Block Walls," *Journal of the Structural Division, ASCE*, Vol.114, No.1, January 1988, pp.121-133.

Essawy, A.S., Drasdale, R.G., and Mirza, F.A., (1985), " Nonlinear Macroscopic Finite Element Model for Masonry Walls ", *New Analysis Techniques for Structural Masonry*, Proceedings of a session held in conjunction with Structural Congress' 85. Illinois, September, 1985.

Ghali, A. and Neville, A.M. (1989) *Structural Analysis - A Unified Classical and Matrix Approach* Third Edition, Chapman and Hall, New York, 1989.

Ghosh, S., (1989)," Flexural Bond Strength of Masonry -- An Experimental Review," *Proceedings of the Fifth North American Masonry Conference*, University of Illinois at Urbana-Champaign, 1989, pp.701-712.

Glanville, J.I. and Hatzinikolas, M.A., (1989), *Engineering Masonry Design* Winston House, Winnipeg, Canada.

Goyal, A., Hatzinikolas, M.A. and Warwaruk, J.,(1993), " Shear Connected Cavity Walls Under Vertical Loads", Structural Engineering Report No. 182, Department of Civil Engineering, University of Alberta, January 1993, Edmonton, Alberta.

Hatzinikolas, M.A., Longworth, J. and Warwaruk, J., (1978), "Concrete masonry Walls", Structural Engineering Report No. 70, Department of Civil Engineering, University of Alberta, September 1978.

Hibbitt, Karlsson and Sorensen, (1994), ABAQUS User's Manuals, Version 5.3, Hibbitt, Karlsson and Sorenson Inc., Providence, RI.

Lotfi, H.R., Hamid, R., Shing, P.B. and Benson, (1994), "Interface Model Applied to Fracture of Masonry Structures", *Journal of the Structural Division, Proceedings of ASCE*, Vol. 120 No.1, pp. 63-80.

Macgregor, J.G., Breen, J.E. and Pfrang, E.O., (1970), " Design of Slender Concrete Columns", *ACI Journal, Proceedings* Vol. 67, No.1, January 1970, pp.6-28.

Mullins, P. and O'Connor, O., (1987), " The Use of Steel Reinforcement System to Improve the Strength and Stiffness of Laterally Loaded Cavity Brick Walls", *Journal of Structural Engineering, ASCE*, Vol. 113, No.2, February 1987. pp. 334-348.

Neis, V.V. and Sakr, K.M., (1993), " Factors Affecting the Ultimate Strength of Masonry Cavity Walls", *Proceedings, The Sixth North American Masonry Conference*, June 6-9, 1993, Philadelphia, U.S.A., pp. 61-72.

Neis, V.V. and Chow, D.Y.T., (1980), " Tensile Bond Testing of Structural Masonry Units", *Proceedings, Second Canadian Masonry Symposium*, June 9-11, 1980, Ottawa, Canada, pp. 381-395

Ojinaga, J. and Turkstra, C.J., (1980), " Design of Plain Masonry Walls", *Canadian Journal of Civil Engineering*, Vol. 7, 1980, pp. 233-242.

Pacholok, K.W., (1988), " Shear Connectors in Masonry Cavity Walls", M.Sc. Thesis, University of Alberta, Department of Civil Engineering, September 1988, Edmonton, Alberta.

Page, A.W. , (1978), " A Finite Element Model for Masonry", *Journal of Structural Division, ASCE*, Vol. 104, No. ST8, August 1978, pp.1267-1285.

Papanikolas, P. K., Hatzinikolas, M.A. and Warwaruk, J.,(1990), "Behavior of Shear Connected Cavity Walls". Structural Engineering Report No. 169, Department of Cavil Engineering, University of Alberta, September 1990, Edmonton, Alberta.

Papanikolas, P.A., Hatzinikolas, M.A., Warwaruk, J. and Elwi, A.E. (1989), "Experimental and Analytical Results for Shear Connected Cavity Walls", *Fifth Canadian Masonry Symposium*, department of Civil Engineering, University of British Columbia, Vancouver, B.C.

Ramm, E.(1981). " Strategies for Tracing the Nonlinear Responses Near Limit Points", in *Nonlinear Finite Element Analysis in Structural Mechanics, Proceedings of the U.S. Workshop*, edited by Wunderlich, W. et al., Springer-Verlag, pp.63-89.

Riks, E., (1979), "An Incremental Approach to the Solution of Snapping and Buckling Problems" *International Journal of Solids and Structures*, Vol. 15, pp. 529-551.

Sarker, A. and Brown, R., (1987), " Flexural Strength of Brick Masonry Using the Bond Wrench," Research Report No.20, Brick Institute of America, Reston, VA, 1987.

Timoshenko, S.P. and Gere, J.M., (1972), *Mechanics of Materials*, Van Nostrand, New York, 1972; p. 372.

Yokel, F.Y. and Dikkers, R.D., (1971), "Strength of Load Bearing Masonry Walls", *Journal of the Structural Division, Proceedings of ASCE*, Vol. 97, May 1971, pp. 1593-1609.

APPENDIX A

Design Example

Design a cavity wall, using a concrete block wythe as back-up, 90 mm clay brick as brick wythe, the two wythes are tied with shear connectors. The height of the wall between points of lateral supports is 4800 mm. The wall is vertically loaded with a factored dead load of 100 kN/m and a factored live load of 100 kN/m acting at an eccentricity of 60 mm away from the centroid of the cross-section of the block wythe. The cavity is 75 mm.

Use: f'_m = 15 MPa for the concrete block, f'_m = 10 MPa for the brick, f_y = 300 MPa for steel .

Solution Trial 1

1. Estimate the thickness of the block wythe:
   Try 200 mm.

2. Is the wall slender? (CAN3-S304.1-94)

$$\frac{kh}{L} = \frac{4800}{190} = 25.3 > 10 - 3.5\left(\frac{e_1}{e_2}\right) = 6.5$$

   The wall is quite slender.

3. Grouting and reinforcement:
   Partially grouted at 400 mm, and reinforced with 15M bars @ 400 mm o.c.

4. Check if the moments are less than the minimum primary moment(CAN3-S304.1-94):

$$e_{min} = 0.1t = 0.1 \times 200 = 20 \text{ mm} < 60 \text{ mm}$$

5. Compute $(EI)_{eff}$:

The modulus of elasticity of the block wythe: $E_m = 850\times15 = 12750$ MPa

The moment of inertia of the block wythe: $I_{block} = I_o = 507\times10^6$ mm^4 / m

The modulus of elasticity of the brick wythe: $E_m = 850\times10 = 8500$ MPa

The moment of inertia of the brick wythe: $I_{brick} = 60.75\times10^6$ mm^4 / m

$$\frac{(EI)_{brick}}{(EI)_{block}} = \frac{60.75\times10^6\times8500}{507\times10^6\times12750} = 0.0799$$

L/t = 4800/190 = 25.3, e/t = 60/190 = 0.3158

$$\therefore \quad (EI)_{eff} = \left(0.6 - 0.7\left(\frac{e}{t}\right) + 0.015\left(\frac{L}{t}\right) + 0.82\left(\frac{(EI)_{brick}}{(EI)_{block}}\right)\right)E_mI_o \qquad \text{Eq.(6.45)}$$

$$= (0.6 - 0.7\times0.3158 + 0.015\times25.3 + 0.82\times0.0799)\times6.46\times10^{12}$$

$$= 0.82\times6.46\times10^{12} = 5.29\times10^{12} \text{ N}\cdot\text{mm}^2/\text{m}$$

6. Compute the magnified moment:

$\beta_d = 0.5$, $k = 1.0$, $C_m = 1.0$

$$P_{cr} = \frac{\pi^2\phi_e(EI)_{eff}}{(1+0.5\beta_d)(kh)^2} = \frac{\pi^2\times0.65\times5.2\times10^{12}}{(1+0.25)\times4800^2} = 1158 \text{ kN/m} \qquad \text{Eq.(6.44)}$$

$$\delta = \frac{C_m}{1-\frac{P}{P_{cr}}} = \frac{1.0}{1-\frac{200}{1158}} = 1.21 \qquad \text{Eq.(6.42)}$$

$$\therefore \quad M_{tot} = Pe\delta = 200\times60\times1.21\times10^{-3} = 14.5 \text{ kN}\cdot\text{m/m} \qquad \text{Eq.(6.41)}$$

7. Design the wall: (CAN3-S304.1-94)

(a) Compute the factored vertical load resistance:

$$P_{r(max)} = 0.8\,(0.85\,\phi_m f'_m A_e)$$
$$= 0.8\,(0.85 \times 0.55 \times 15 \times 132.7 \times 10^3)$$
$$= 744 \text{ kN/m}$$

(b) Compute the factored moment resistance under pure bending:

Check if $f_s = f_y$?

$$C = 0.85\,ab\phi_m\chi f'_m = 0.85 \times 0.8 \times c \times 1000 \times 0.55 \times 1 \times 15$$

Where, $$c = \frac{600}{600 + f_y} \times 95$$

$$T = \phi_s f_s A_s = 0.85 \times f_s \times 500 = 425\, f_s$$

$$C = T$$

$\therefore$ $$f_s = 617 > f_y$$

Hence, $f_s = f_y$

$$0.85\,ab\phi_m\chi f'_m = \phi_s f_s A_s$$
$$0.85 \times a \times 1000 \times 0.55 \times 15 = 0.85 \times 300 \times 500$$
$$a = 18.18$$

$\therefore$ $M = \phi_s f_s A_s\,(95 - a/2) = 0.85 \times 300 \times 500 \times (95 - 18.18/2)$
$= 10.95$ kN· m /m

(c) Construct a simplified interaction diagram:

$$e_k = \frac{S}{A_e} = \frac{5.34 \times 10^6}{132.7 \times 10^3} = 40.2 \text{ mm}$$

Construct a simplified interaction diagram with three points: (P_{rmax}, 0), ($P_{rmax}/2$, $P_{rmax}e_k/2$), (0, M_r)

The point representing the factored load P_f and magnified moment M_{tot} (200kN/m, 14.5kN·m/m) falls outside the interaction diagram as shown below:

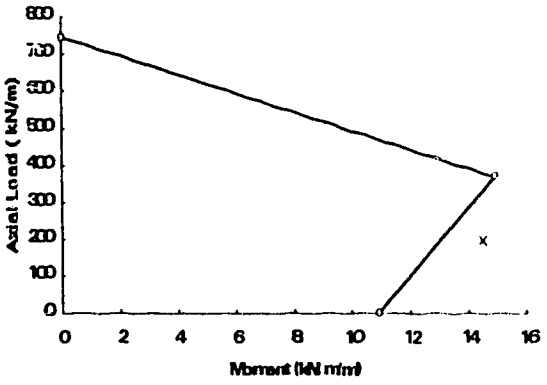

The design is not adequate.

Solution Trial 2

Try 250 mm block wythe partially grouted at 400 mm and reinforced with 15M bars @ 400 mm o.c. Repeat the above design procedures:

$$\frac{kh}{L} = \frac{4800}{240} = 20 > 10 - 3.5\left(\frac{\varepsilon_1}{e_2}\right) = 6.5$$

$e_{min} = 0.1t = 0.1 \times 240 = 24 \text{ mm} < 60 \text{ mm}$

The moment of inertia of the block wythe: $I_{block} = I_o = 984 \times 10^6 \text{ mm}^4 / \text{m}$

$$\frac{(EI)_{brick}}{(EI)_{block}} = \frac{60.75\times10^6\times8500}{984\times10^6\times12750} = 0.0412$$

L/t = 4800/240 = 20, e/t = 60/240 = 0.25

$$\therefore \quad (EI)_{eff} = \left(0.6 - 0.7\left(\frac{e}{t}\right) + 0.015\left(\frac{L}{t}\right) + 0.82\left(\frac{(EI)_{brick}}{(EI)_{block}}\right)\right)E_m I_o$$

$$= (0.6 - 0.7\times0.25 + 0.015\times20 + 0.82\times0.0412)\times12.55\times10^{12}$$

$$= 0.758\times12.55\times10^{12} = 9.52\times10^{12}\ \text{N}\cdot\text{mm}^2/\text{m}$$

Compute the magnified moment:

$\beta_d = 0.5$, $k = 1.0$, $C_m = 1.0$

$$P_{cr} = \frac{\pi^2\phi_e(EI)_{eff}}{(1+0.5\beta_d)(kh)^2} = \frac{\pi^2\times0.65\times9.52\times10^{12}}{(1+0.25)\times4800^2} = 2120\ \text{kN/m}$$

$$\delta = \frac{C_m}{1-\frac{P}{P_{cr}}} = \frac{1.0}{1-\frac{200}{2120}} = 1.10$$

$\therefore \quad M_{tot} = Pe\delta = 200\times60\times1.10\times10^{-3} = 13.2\ \text{kN}\cdot\text{m}$

Design the wall:

Compute the factored vertical load resistance:

$$P_{r(max)} = 0.8\,(0.85\,\phi_m f'_m A_e)$$

$$= 0.8\,(0.85\times0.55\times15\times160.85\times10^3)$$

$$= 902\ \text{kN/m}$$

Compute the factored moment resistance under pure bending:

$0.85\, ab\phi_m \chi f'_m = \phi_s f_s A_s$

$0.85 \times a \times 1000 \times 0.55 \times 15 = 0.85 \times 300 \times 500$

$a = 18.18$

$\therefore M = \phi_s f_s A_s (95 - a/2) = 0.85 \times 300 \times 500 \times (120 - 18.18/2)$

$= 14.14$ kN· m /m

Construct a simplified interaction diagram with three points: (P_{rmax}, 0), ($P_{rmax}/2$, $P_{rmax}e_k/2$), (0, M_r).

$$e_k = \frac{S}{A_e} = \frac{8.2 \times 10^6}{160.85 \times 10^3} = 50.98 \text{ mm}$$

The point representing the factored load P_f and magnified moment M_{tot} (200kN/m, 14.5kN·m/m) falls inside the interaction diagram as shown below:

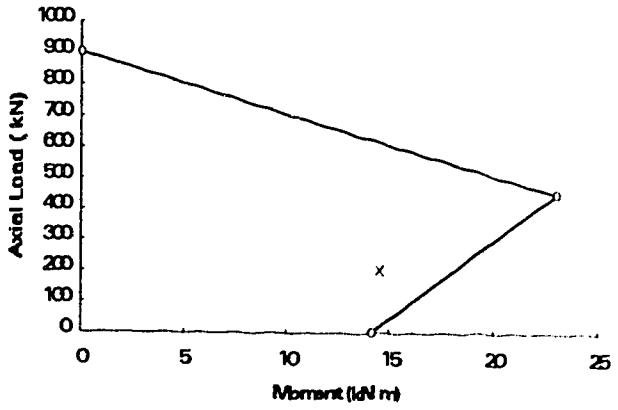

The design is adequate.